

Computational studies of silica

Kathryn Glaser

Department of Chemistry, University College London

May 2011

Supervisors: Dr. R. G. Bell, Prof. C. R. A. Catlow and

Prof. A. Takada

A thesis submitted for the degree of Doctor of Engineering

Declaration

I, Kathryn Joan Glaser confirm that the work presented in this thesis is my own. Where information has been derived from other sources, I confirm that this has been indicated in the thesis.

Abstract

There are three areas of research in this thesis. The first is concerned with the silica polymorph, tridymite, with simulations carried out using three computational methods: free energy minimisation, molecular dynamics and Density Functional Theory. A number of tridymite structures with different atomic configurations have been found in nature. The simulations explore various properties of these different forms of tridymite and investigate whether it is possible to distinguish between them using the three computational techniques. It was found that the interatomic potential and simulation technique used, rather than the simulation temperature, were the main factors affecting the resulting structure. There are a number of possible explanations for this result: The techniques may not be sensitive enough to deal with an energy landscape as flat as in the case of tridymite. Another reason is that the potentials have been parameterised to distinguish between structures which have reconstructive transitions (where bonds are broken and formed) and may not be able to deal with displacive transitions (where only angles between atoms change) as with tridymite. The final possible explanation is that a number of the known structures may be meta-stable and/or poorly characterised.

For the second research area molecular dynamics simulations using a rigid ion two body potential were carried out in order to investigate the properties of silica melts and glasses. A number of different silica crystals were melted to see whether the melts are all similar or whether their properties can be differentiated according to the original crystal structure. At sufficiently high temperatures the starting

structure did not affect the properties of the melt. Several properties of silica melts and glasses were investigated: mean square displacement, autocorrelation functions, pair distribution functions, the extent to which silicon and oxygen atoms move together, Arrhenius plots, coordination number, bond lengths and angles. Investigations were also carried out as to whether it is possible to use a shell model to simulate a silica melt. Various properties were calculated and it was found that agreement with experiment was not as accurate as when using the rigid ion model.

The third research area is an exploration of the properties of amorphous silica at elevated pressures and a range of temperatures, using molecular dynamics with a rigid ion two body potential. Calculations show that, at low temperatures, the distortion of the tetrahedra is not recovered upon decompression whereas experimental results find complete recovery of the tetrahedra. There is little available experimental data on the behaviour of silica at both high pressures and temperatures. Calculations show that at high temperatures all properties of the initial structure before compression are recovered.

Contents

Declaration	1
Abstract	2
Acknowledgements	12
1 Introduction	13
1.1 Introduction to silica	15
1.2 Introduction to tridymite	16
1.3 Other silica polymorphs	26
1.3.1 Cristobalite	28

CONTENTS

1.3.2	Quartz	29
1.3.3	Coesite	30
1.3.4	Stishovite and other six coordinated polymorphs	33
1.3.5	Higher pressure phases	34
1.4	Introduction to amorphous silica	36
2	Methodology	41
2.1	Free energy minimisation	41
2.2	Molecular dynamics	46
2.2.1	Finite difference methods	47
2.2.2	Time step	49
2.2.3	Initial velocities	51
2.2.4	Equillibration and simulation time	52
2.2.5	Periodic boundary conditions	52
2.2.6	Ensembles	55

CONTENTS

2.2.6.1	Constant temperature simulations	55
2.2.6.2	Constant pressure simulations	56
2.2.6.3	Choice of ensemble	57
2.2.7	Ewald summation	57
2.3	Potentials	59
2.3.1	Forces	61
2.3.1.1	Electrostatics	61
2.3.1.2	Repulsion	61
2.3.1.3	Dispersion	62
2.3.1.4	Spring or bond stretch	62
2.3.1.5	Angle bending	63
2.3.1.6	Shell model	65
2.3.2	The BKS potential	66
2.3.3	The Sanders potential	68

CONTENTS

2.4	Electronic structure calculations	70
2.5	Properties	71
2.5.1	Pair Distribution Function	71
2.5.2	Mean Square Displacement	74
2.5.3	Diffusion coefficient	74
2.5.4	Velocity Autocorrelation Function and Vibra- tional Density of States	75
2.5.5	Arrhenius plots	76
2.6	Programs	77
3	An exploration of the silica polymorph tridymite	78
3.1	Free energy minimisation	79
3.1.1	Methodology	79
3.1.2	Results	80
3.1.2.1	Final atomic configuration	80

CONTENTS

3.1.2.2	Energy and volume	83
3.2	Molecular Dynamics	86
3.2.1	Methodology	86
3.2.2	Results	88
3.2.2.1	Energy and volume	88
3.2.2.2	Final atomic configurations	91
3.2.2.2.1	Pair Distribution Functions	96
3.2.2.2.2	Bond lengths	100
3.2.2.2.3	O-Si-O angles	101
3.2.2.2.4	Si-O-Si angles	102
3.2.2.3	Alternative simulations	104
3.3	Simulations involving two potentials	106
3.4	Simulations involving two methods	108
3.5	Density Functional Theory	114

CONTENTS

3.6	Discussion and conclusions	116
3.6.1	Energy and volume	116
3.6.2	Final atomic configuration	117
3.6.3	Conclusions	118
4	The static and dynamic properties of silica melts and glasses	121
4.1	Modification of the BKS potential	122
4.2	Production of quenched structure	127
4.3	Diffusion	128
4.4	Arrhenius plots and activation energies	133
4.5	Energy and volume	140
4.6	Bond lengths, angles and Pair Distribution Functions	143
4.7	Coordination of silica melts and glasses	157
4.8	The effect of defects in a crystal on its melting behaviour	162

CONTENTS

4.9	The nature of the Si-O bond in a melt	165
4.10	Melting a structure using the Sanders potential	171
4.11	Conclusions	175
5	The behaviour of amorphous silica under pressure	178
5.1	Introduction	178
5.2	Literature review	180
5.2.1	Compression at ambient temperatures	180
5.2.1.1	Experimental studies	180
5.2.1.2	Computational studies	182
5.2.2	Compression at high temperatures	184
5.2.2.1	Experimental studies	184
5.2.2.2	Computational studies	185
5.3	Results	186
5.3.1	Volume	187

CONTENTS

5.3.2	Coordination, bond lengths and angles	191
5.3.3	Gradual application and release of pressure . .	195
5.3.4	The release of both high pressures and tem- peratures	201
5.4	Summary and conclusions	203
5.4.1	Summary	203
5.4.2	Conclusions	205
6	Summary and future work	207
6.1	Summary	207
6.2	Future work	211
	Bibliography	213

Acknowledgements

I would like to thank my supervisors, Dr. Robert G. Bell, Prof. C. Richard A. Catlow and Prof. Akira Takada, for their advice, encouragement, friendliness and patience. I would also like to thank past supervisors, Dr. Mark Wilson and Prof. G. David Price, for giving me the opportunity to come to UCL.

I would also like to thank the following people: Clyde Fare, Dr. Alexei Sokol and Dr. Scott Woodley for useful discussions on energy minimisation, Dr. Simon Clifford for help with I.T., Dr. Dominic Daisenberger for encouragement, advice and help with molecular dynamics, Dr. Jamieson Christie for general advice and Hugh Glaser for proofreading.

I am most grateful to the Engineering and Physical Sciences Research Council, the UCL Graduate School and the Asahi Glass Company Ltd. for funding my research. I am also grateful to W. Smith, T. R. Forester and I. T. Todorov for permission to use the DL_POLY code and to J. D. Gale for permission to use the Gulp code.

Finally, I would like to thank my friends and family for all their support and encouragement.

Chapter 1

Introduction

Silica (SiO_2) is the most abundant oxide in the earth's crust [1], with over 90% of its volume being composed of silicate minerals [2] (minerals which contain silica amongst other molecules). The crusts of the moon, Mercury, Venus and Mars are also mostly composed of silica [3]. It is the main constituent of soil [3] and has a wide range of applications: It is the archetypal glass former and is the principal constituent of most glasses. It provides the raw material for the production of silicon for use in computer chips. Fibre optic cables for use in the telecommunications industry are produced from silica. It is a good insulator and is used extensively in the production of ceramics. It is therefore studied extensively.

There are three areas of research in this thesis: One of the least well understood polymorphs of silica is the tridymite polymorph. A number of tridymite structures with different atomic configurations have been found in nature. Chapter 3 discusses research into tridymite and describes the exploration of various properties of the different forms of tridymite and an investigation into whether it is possible to distinguish between them using a number of computational techniques. Section 1.2 of this chapter introduces tridymite and its various configurations. Section 1.3 of this chapter briefly describes other silica polymorphs.

Chapter 4 describes computational research into the static and dynamic properties of liquid and glassy silica at ambient pressure. Computational techniques are especially useful for investigating the properties of amorphous structures such as liquids and glasses because there are certain properties that, in contrast to crystalline materials, experimental techniques are not able to precisely determine. Section 1.4 of this chapter is an introduction to amorphous silica.

The final research area, described in chapter 5, extends the scope of chapter 4 to explore the properties of amorphous silica at non-ambient pressures. The majority of experimental and computational

studies in the literature relating to the application and release of pressure have been carried out at ambient temperature. Simulations where the application and release of pressure is carried out at elevated temperatures are described. Amorphous silica has a wide variety of applications and is used under a range of conditions. It is therefore important to understand how its properties are affected by variations in both pressure and temperature.

1.1 Introduction to silica

The basic building block of crystalline silica is a silicon atom surrounded by four, six or eight oxygen atoms forming a tetrahedron, octahedron or cube respectively. There are a large number of silica polymorphs. The most common are quartz, cristobalite, tridymite, coesite and stishovite. Transitions between these structures require the breaking of bonds and the forming of new ones (reconstructive transitions). Within a number of these polymorphs transitions can take place where no breaking of bonds occurs but where the angle between three atoms changes, called displacive transitions. The best known displacive transition is probably between α -quartz and β -quartz. The most significant changes that occur in displacive transitions in silica are changes in the Si-O-Si angles, i.e. changes in the

angles between the basic building blocks of tetrahedra, octahedra or cubes. The atomic arrangement within the basic building block is not significantly altered in this type of transition.

1.2 Introduction to tridymite

The first research theme of this thesis concerns the silica structure of tridymite. There are a large number of tridymite polymorphs, perhaps because the tridymite structure is composed of large tunnels and so is easily deformable. Figures 1.1 - 1.6 show some polymorphs of tridymite that have been discovered in nature. Silicon atoms are green and oxygen atoms are blue. All figures were obtained from [4] and are shown as four primitive unit cells together (two in each unit cell dimension).

Tridymite occurs at ambient pressure and is formed of silica (SiO_4) tetrahedra. These are joined together in six-membered rings, with tetrahedra alternately pointing up and down. The rings are joined together to make a sheet, with each tetrahedron being a member of 3 rings in each sheet. The sheets are placed on top of each other, but with tetrahedra that point down above tetrahedra that point up, in an ABAB stacking. The bottom oxygen atom of a tetrahedron

pointing down and the top oxygen atom of a tetrahedron pointing up on a sheet below it are the common linking atom. A large number of tridymite polymorphs have been found in nature or synthesised, more than for any other silica structure. A detailed description of their ideal structure now follows.

HP (hexagonal packed) or high tridymite [5] [6] [7] (Figure 1.1) has space group $P6_3/mmc$ and is the highest temperature form of tridymite. It is stable at temperatures above 750 K [8]. In the HP structure as first determined by R. E. Gibbs in 1927 [7], all Si-O-Si angles were determined to be 180° , creating a structure with hexagonal shaped tunnels. However, structural refinements by K. Kihara in 1978 [5] revealed that 180° is only an average and that the true value is approximately 149.2° . It is not clear whether the value of 180° is an average over time (i.e. all atoms are vibrating about an average of 180°) or whether it is an average over all space (i.e. the individual Si-O-Si angles are different, but their average over the entire structure is 180°). Similar behaviour applies to β -quartz and β -cristobalite [7], which is discussed later in Section 1.3.

LHP (lower hexagonal packed) tridymite [5] [9] (Figure 1.2) has space group $P6_322$ and is stable in the temperature range 680 K - 750 K [8]. It was first discovered by D. Cellai in 1994 [5]. It is

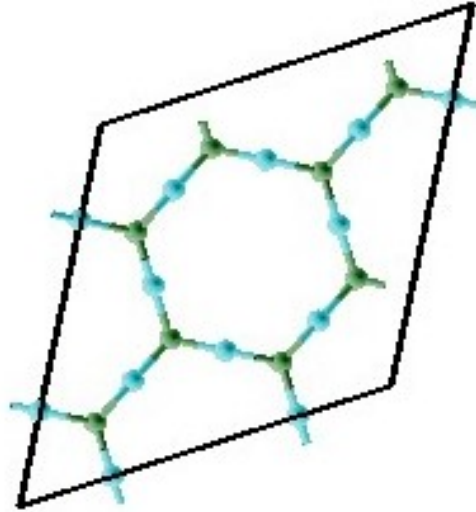


Figure 1.1: HP (Hexagonal Packed) or high tridymite (size $2 \times 2 \times 2$ primitive unit cells)

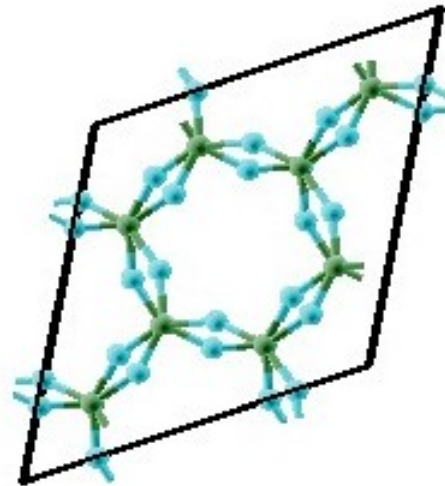


Figure 1.2: LHP (Lower Hexagonal Packed) tridymite (size $2 \times 2 \times 2$ primitive unit cells)

essentially the same as the HP form except that the Si-O-Si angles in the planes of the rings are 151.56° . The direction of the bend in the Si-O-Si angle alternates between the layers, i.e. if an Si-O-Si angle in one sheet is 151.56° , the corresponding Si-O-Si angle in the sheet below it will be $360^\circ - 151.56^\circ = 208.44^\circ$. The Si-O-Si angles between sheets remain at 180° .

OC (third orthorhombic) tridymite [10] [11] [12] (Figure 1.3) has space group $C222_1$ and is stable in the temperature range 520 K - 620 K [8]. It was first determined by W. A. Dollase in 1967 [12]. The structure differs from the HP form in that the sheets are not aligned. The displacement alternates between the sheets in an ABAB form. Also, the Si-O-Si angles are slightly less than 180° . The Si-O-Si angles between the sheets are 177.25° . In the planes of the rings there are four Si-O-Si angles of 160.60° and two angles of 170.38° .

OP (orthorhombic) tridymite [13] [14] [10] (Figure 1.4) has space group $P2_12_12_1$ and is stable in the temperature range 380 K - 420 K [8]. Its structure was first determined by A. Nukui, A. Yamamoto and H. Nakazawa in 1979 [10]. As with OC tridymite the sheets are displaced from one another in an ABAB form. In the structures described so far the rings have all been the same shape. In the OP tridymite structure there are two types of ring with differing Si-O-

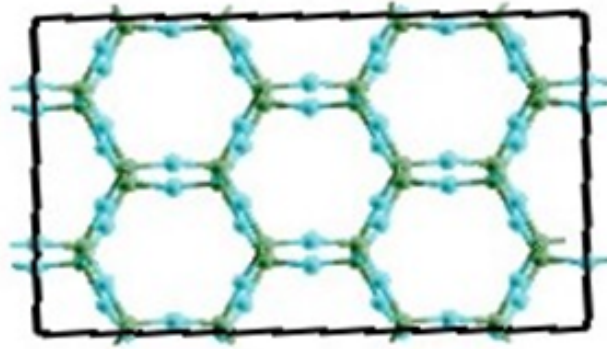


Figure 1.3: OC (third orthorhombic) tridymite (size $2 \times 2 \times 2$ primitive unit cells)

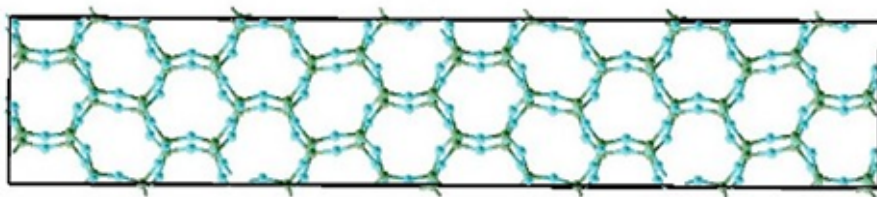


Figure 1.4: OP (orthorhombic) tridymite (size $2 \times 2 \times 2$ primitive unit cells)

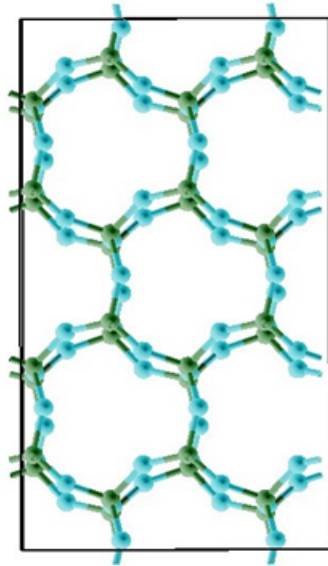


Figure 1.5: MC (monoclinic) tridymite (size 2x2x2 primitive unit cells)

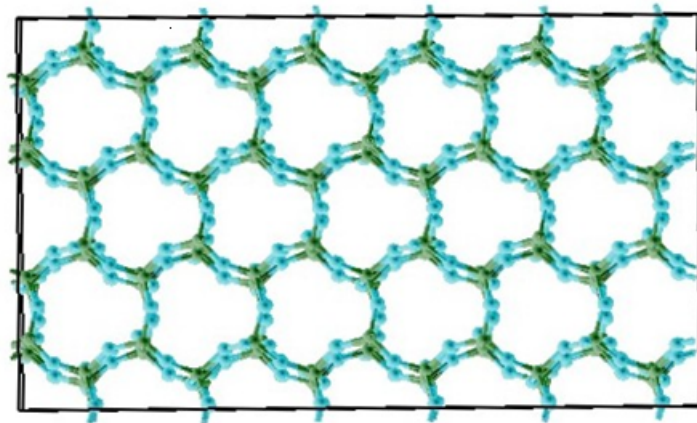


Figure 1.6: MX1 (low) tridymite (size 2x2x2 primitive unit cells)

Si angles. One type has 2-fold rotational symmetry, the other has 3-fold rotational symmetry.

MC (monoclinic) tridymite [15] [16] [17] (Figure 1.5) has space group Cc and is stable in the temperature range 340 K-370 K or 340 K - 380 K [8]. Its structure was first determined in 1976 by K. Kato and A. Nukui [17] and W. A. Dollase and W. H. Baur [16]. The sheets are displaced from one another in an ABAB form, with the Si-O-Si angles between the sheets being 175.43° . In the planes of the rings there are three Si-O-Si angles each of 147.06° , 149.80° and 155.39° . Most naturally occurring MC tridymite has been found in meteorites. The remaining MC tridymite structures are of synthetic origin [18].

MX1 (low) tridymite [19] [20] [21] (Figure 1.6) has space group $P1$ and is stable at temperatures below 380 K [8]. It was first discovered by S. P. Gardner and D. E. Appleman in 1974 [22]. It has a large unit cell with many different Si-O-Si angles. For more details on the structure see [23].

Figures 1.7 - 1.9 show Pair Distribution Functions (PDFs) for the above crystal structures. PDFs are explained in section 2.5.1. Figures 1.10 - 1.12 show Si-O bond lengths, O-Si-O angles and Si-O-Si

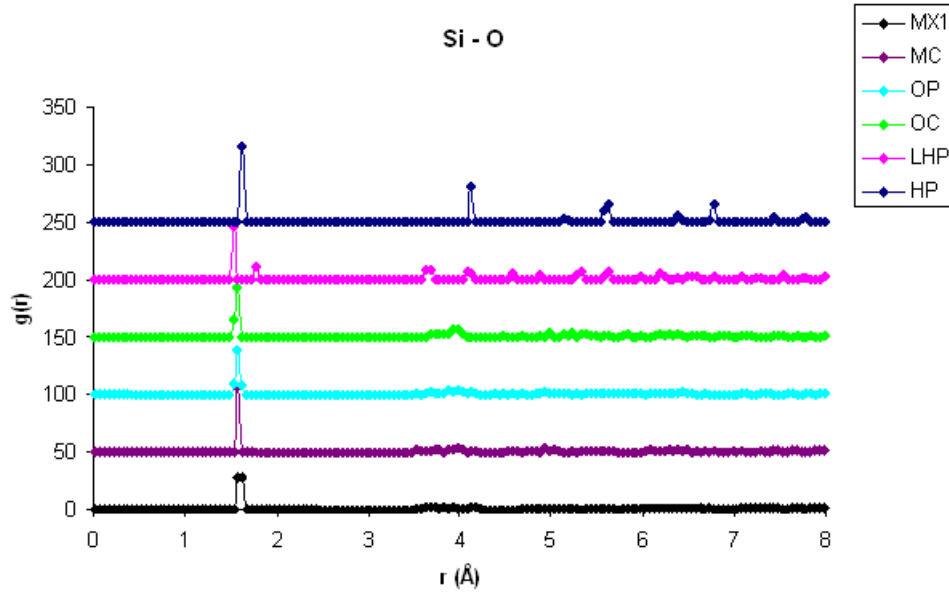


Figure 1.7: Si-O PDF

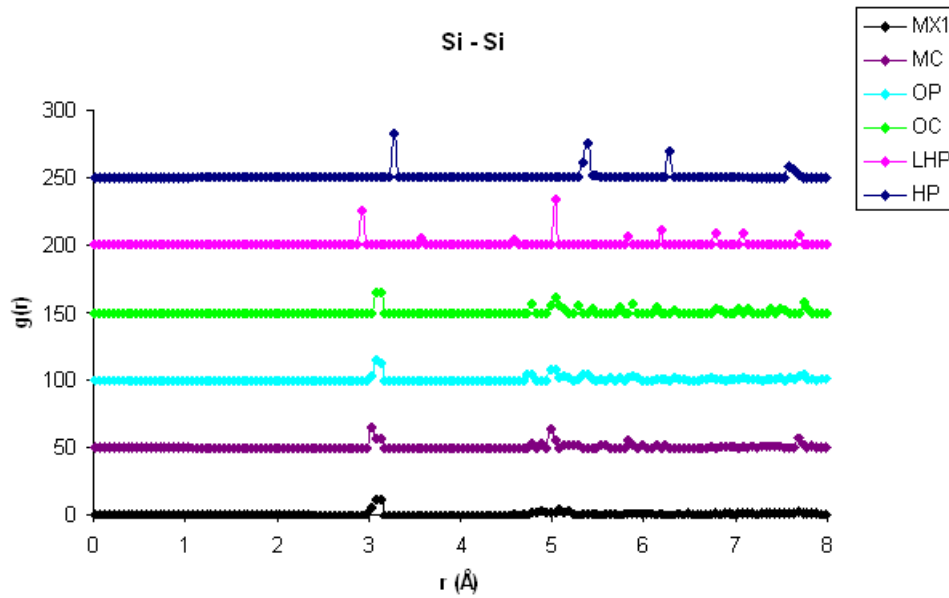


Figure 1.8: Si-Si PDF

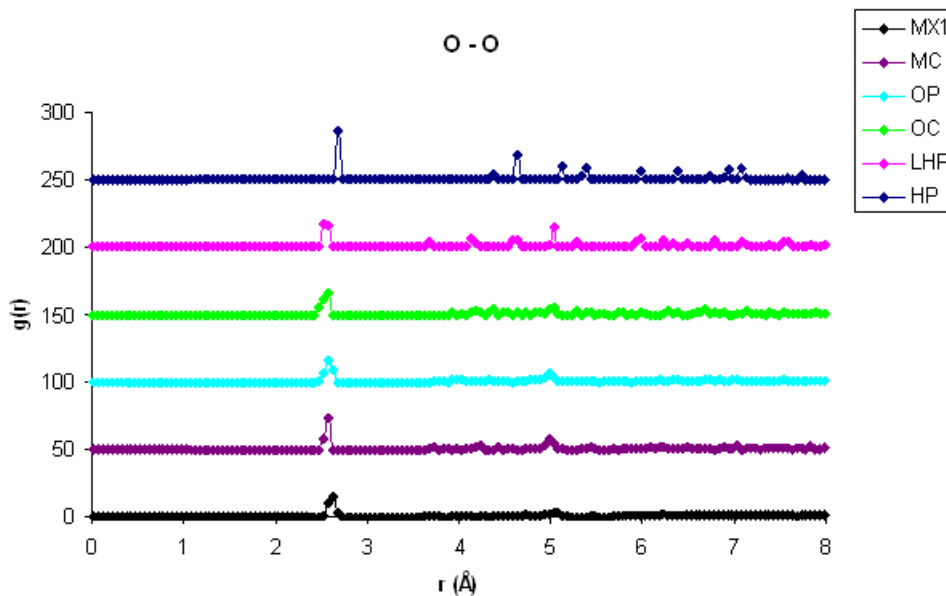


Figure 1.9: O-O PDF

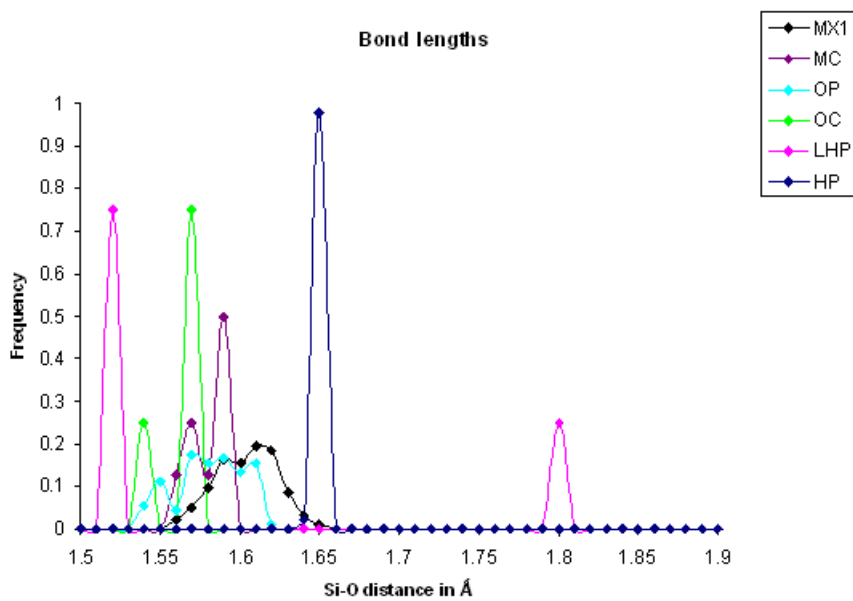


Figure 1.10: Si-O bond lengths

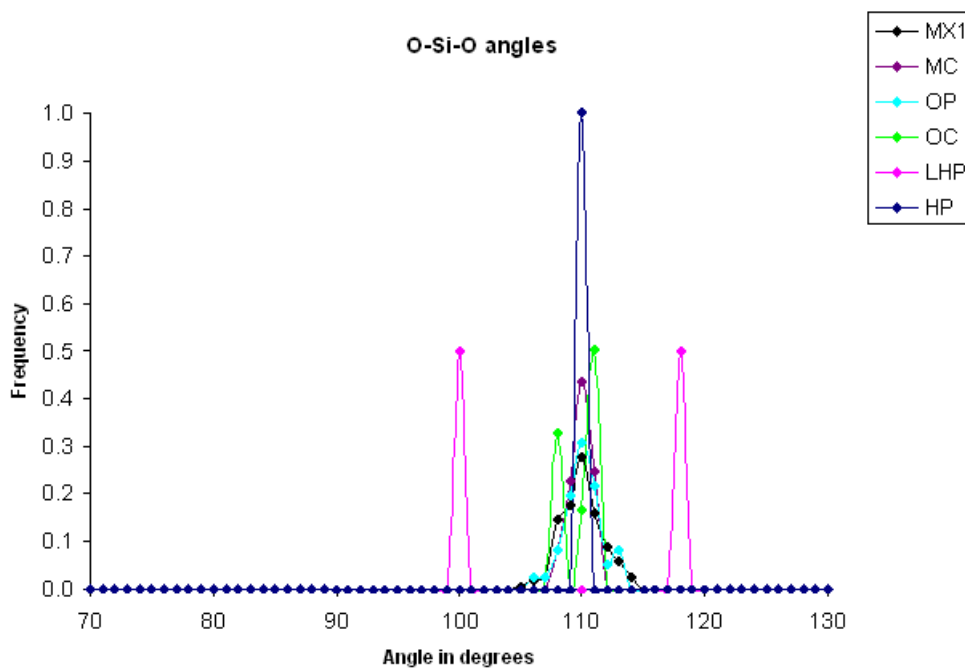


Figure 1.11: O-Si-O angles

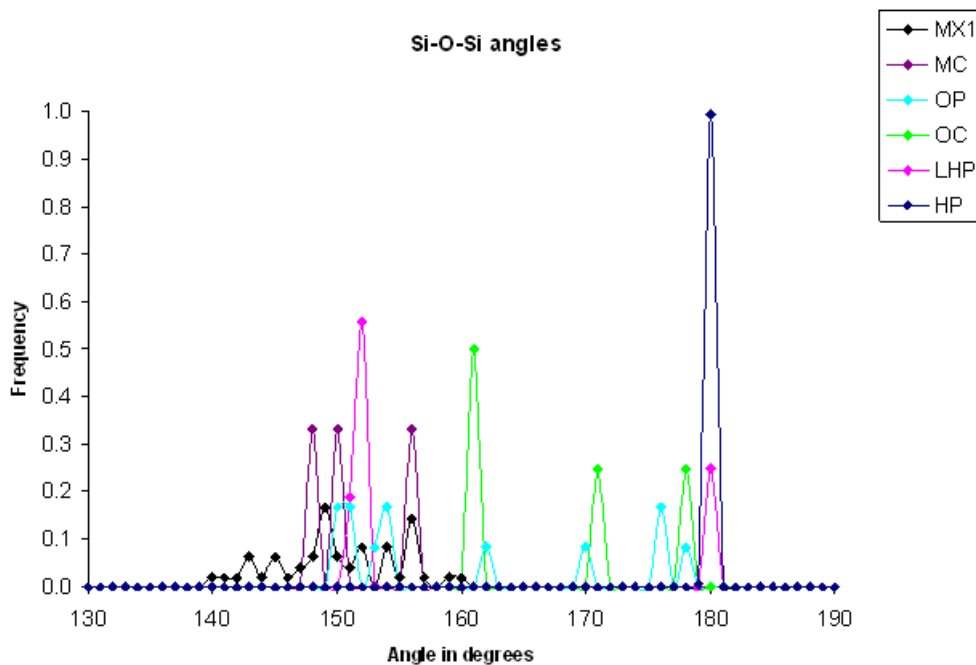


Figure 1.12: Si-O-Si angles

angles for the above crystal structures.

The different polymorphs of tridymite are some of the least understood and investigated polymorphs of silica. The first research theme in this thesis focuses on gaining a better understanding of this polymorph. This work is described in chapter 3. There were a number of aims:

- 1) The first was to investigate whether it is possible to distinguish between the different phases of tridymite described above using a number of computational techniques.
- 2) The second was to explore various properties of the polymorphs of tridymite (e.g. Pair Distribution Function, bond angles and bond lengths) using computer simulations.
- 3) Finally the performance of two different widely used potentials was compared: the BKS potential [24] and the Sanders potential [25] (which are described in sections 2.3.2 and 2.3.3).

1.3 Other silica polymorphs

Figure 1.13 shows a simplified phase diagram of silica. It can be seen that α -quartz is the most stable structure at ambient temperature

and pressure. It is therefore the most abundant structure of the silica polymorphs in the earth's crust [7].

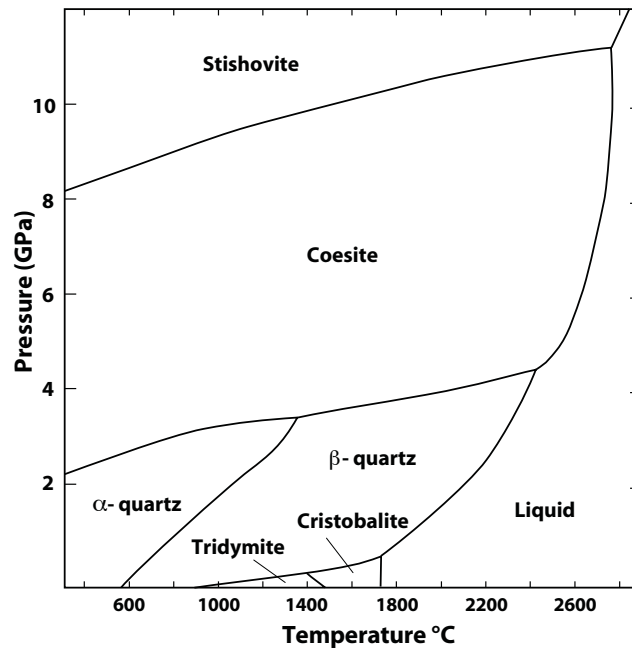


Figure 1.13: Silica phase diagram taken from [26]

This section describes the other polymorphs of silica. It only includes those structures which have a field of thermodynamic stability (structures which have a point on the temperature/pressure phase diagram where they are the most energetically favourable).

1.3.1 Cristobalite

Cristobalite, shown in Figure 1.14, is four coordinated and stable at ambient pressure. It has space group $Fd-3m$ and is stable in the temperature range 1743 K to 2000 K [7]. Its average structure is similar to HP-tridymite (section 1.2) in that it is constructed from six membered rings of tetrahedra. However, in cristobalite the sheets are not stacked directly above one another but are stacked with a tetrahedron of one layer above the hexagonal void of the layer below, so that the hexagons overlap. As can be seen in the figure, in contrast to tridymite where the tetrahedra have the same orientation in all layers, in cristobalite the tetrahedra of one layer are rotated by 60° relative to the tetrahedra in layers above and below. As with HP-tridymite the structure shown does not represent the true instantaneous structure and is either a spatial or temporal average structure [7]. (The structure shown in Figure 1.14 is in fact β -cristobalite, which can undergo a displacive transition to a metastable state, α -cristobalite, where the hexagonal rings become oval shaped.)

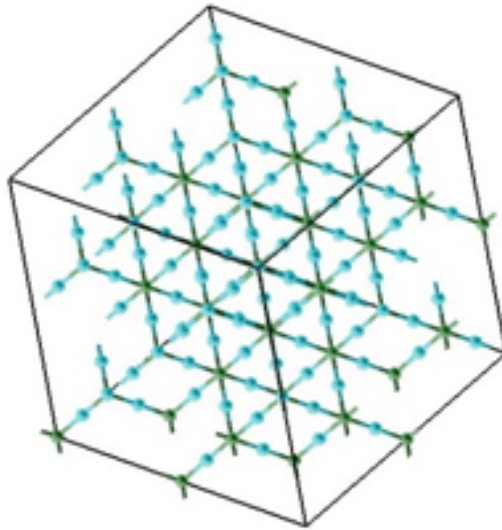


Figure 1.14: Cristobalite

1.3.2 Quartz

Like tridymite and cristobalite, quartz is a low pressure polymorph and is four coordinated. β -quartz has space group $P6_422$ and is stable in the temperature range 846 K to 1140 K at atmospheric pressure [7]. Its average structure is shown in Figure 1.15b. Its tetrahedra are connected in a spiral shape with the sixth tetrahedron being directly above the first one. As with HP-tridymite and β -cristobalite, the structure shown in Figure 1.15 does not represent the true instantaneous structure and is either a spatial or temporal average structure.

β -quartz can undergo a displacive transition to α -quartz. When

viewed along the spirals (in the 001 direction) as in Figure 1.15b, β -quartz spirals appear hexagonal (having six-fold rotational symmetry), with all O-O distances being equal. When viewed from the same direction (as in Figure 1.15a) α -quartz spirals only have three-fold rotational symmetry, with the O-O distances appearing alternately longer and shorter. α -quartz has space group $P3_12_1$ and is stable in the temperature range 0 K to 846 K at atmospheric pressure [7].

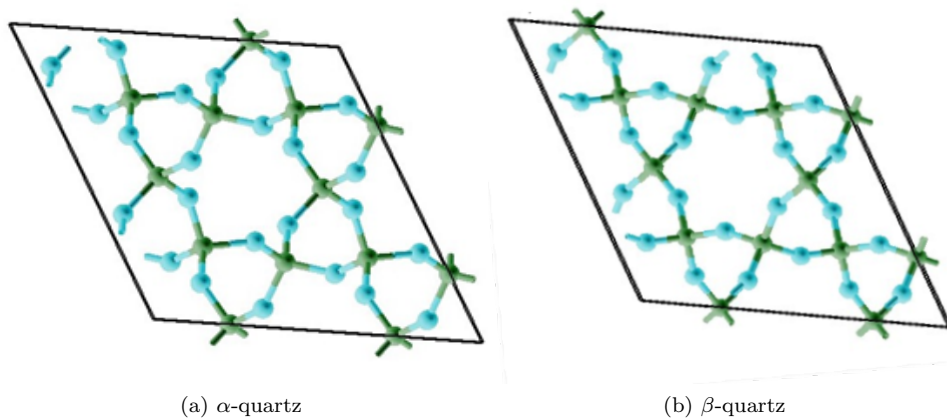


Figure 1.15: Quartz

1.3.3 Coesite

The polymorphs discussed so far are all stable at ambient pressure. Coesite (shown in Figure 1.16) is a high pressure polymorph, although it is still four coordinated. Unlike quartz, tridymite and

crystalite, which are made up of six membered rings of tetrahedra, coesite is constructed of four membered rings, allowing denser packing. Unlike the lower pressure polymorphs, there is only one coesite structure, e.g. no α or β phases, probably due to the denser packing which prevents the structure from being distorted as much as the lower pressure polymorphs. It has space group $C2/c$. At ambient temperature quartz converts to coesite at pressures of 2 - 3 GPa which is stable up to approximately 8 GPa [27].

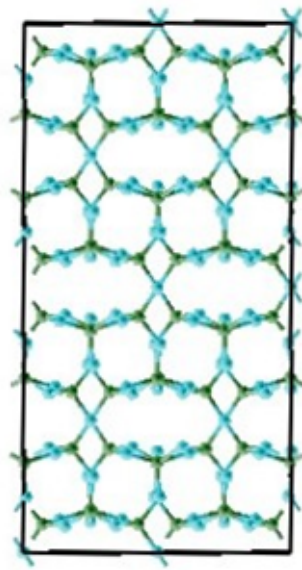
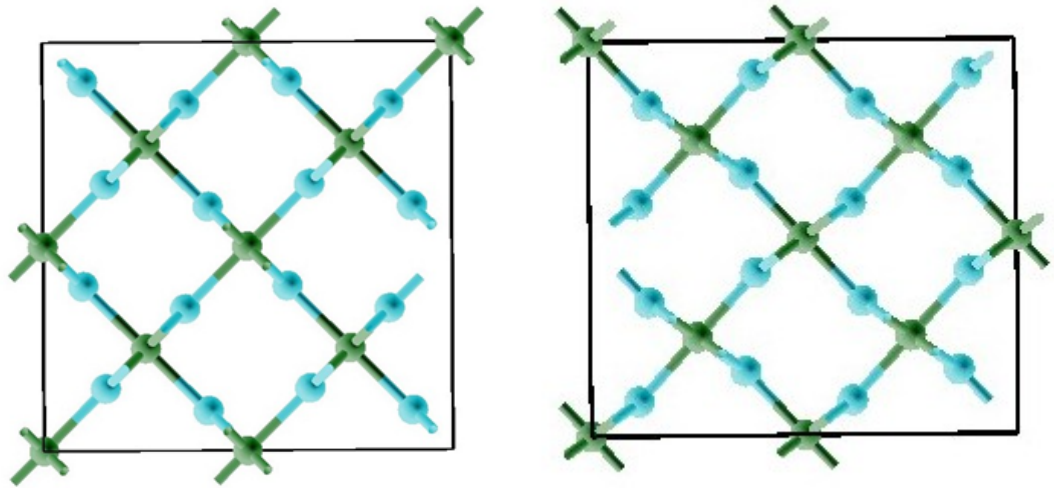
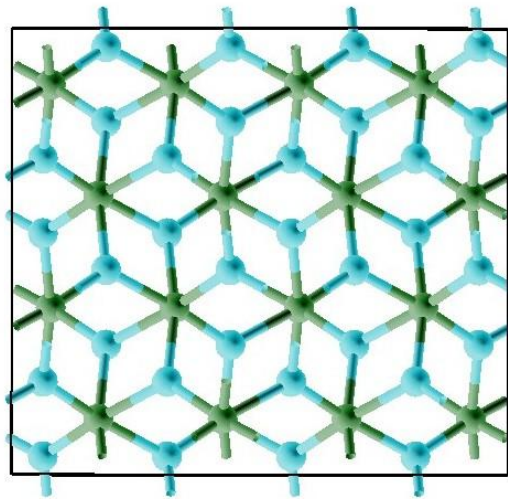


Figure 1.16: Coesite



(a) Stishovite structure

(b) CaCl₂ structure(c) PbO₂ structureFigure 1.17: Stishovite, PbO₂ and CaCl₂

1.3.4 Stishovite and other six coordinated polymorphs

Coesite transforms to stishovite (Figure 1.17a) at approximately 8 GPa [27] at ambient temperature. Stishovite has the structure of rutile, with space group $P4_2/mnm$. It is six coordinated (its basic building block is an octahedron) allowing close packing of the atoms. Unlike the lower pressure polymorphs where all bond lengths in a structure are approximately the same, two of the Si-O bonds in stishovite octahedra are significantly longer than the other four. The length of the two longer bonds is approximately 1.81 Å compared to 1.75 Å for the four shorter bonds. Both these values are larger than the bond lengths of the lower pressure polymorphs (approximately 1.6 Å) in order to accommodate the higher coordination. The two longer bonds are in line with each other and therefore the octahedra have the appearance of being stretched along one axis (i.e. one axis has four-fold rotational symmetry and two have two-fold rotational symmetry). The octahedra are connected such that the oxygen at a corner of an octahedron with a longer bond length and an oxygen at a corner of a neighbouring octahedron with a shorter bond length are the common linking atom.

There is some debate over the stability of and location of the phase boundaries of post-stishovite phases. The PbO_2 structure (not on

the phase diagram) shown in Figure 1.17c has space group $Pbcn$ and is stable at pressures from 35 GPa to 61 GPa according to [28]. The octahedra are more asymmetric than in stishovite with two of the Si-O bonds being approximately 1.98 Å and the other four being approximately 1.72 Å. Unlike stishovite, where the octahedra are connected via corner sharing, in the PbO_2 structure there is edge sharing, giving a denser packing. The octahedra are connected such that two opposing edges of each octahedron are connected to edges of other octahedra (accounting for four of the six oxygen atoms). The two remaining oxygen atoms are connected via corner sharing to the corners of two other octahedra.

The $CaCl_2$ structure (not on the phase diagram) shown in 1.17b has space group $Pnmm$ and is stable at pressures from 50 GPa [29] to at least 120 GPa [30]. In stishovite the Si-O-Si angles are all 90°. The $CaCl_2$ structure differs from stishovite in that these angles are alternately smaller and larger allowing for a denser structure.

1.3.5 Higher pressure phases

The phases described so far have all been established experimentally as the most stable structure at a particular temperature and

pressure. A number of ultra-high pressure eight fold coordinated phases have been synthesised in the laboratory, although none have been found in nature. It has not been established experimentally whether there is a point on the phase diagram where they are the most stable phase, although calculations suggest that this is a possibility. The fluorite structure (Figure 1.18) is an example of one of these phases [6]. Its structure can be thought of as a stacking of cubes with an oxygen atom at each of the eight corners and a silicon atom at the centre of each alternate cube. It has space group $Fm-3m$.

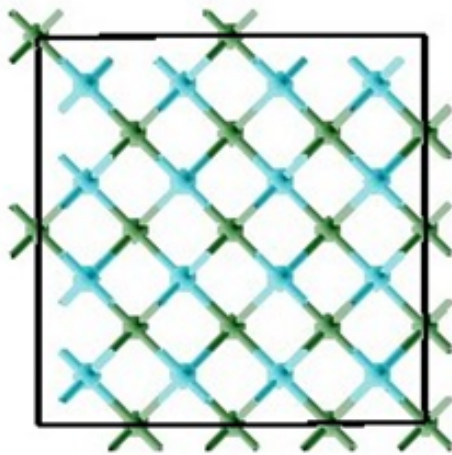


Figure 1.18: Fluorite

1.4 Introduction to amorphous silica

According to J. E. Shelby [31, p. 3] the definition of a glass is: “An amorphous solid completely lacking in long-range, periodic atomic structure, and exhibiting a region of glass transformation behaviour.” A region of glass transformation behaviour is a temperature range at which the amorphous structure of a melt becomes frozen in. A lack of long-range order means that, unlike crystalline structures, there is no precise repetition of structural units. Therefore, similarly to liquids and gases, the structure of amorphous silica must be defined statistically [32]. Although there is no long range order, a glass does exhibit some short range order. Experimental data for amorphous silica are discussed in chapter 4.

Silica is a good glass former because, in comparison to other materials, the energy of the vitreous structure is only a little higher than that of silica crystal structures [33]. This makes it easier for the atomic configuration to fall into that of the vitreous structure as the material is being quenched. Additionally, silica is a network structure where all bonds are the same (unlike molecular structures where there can be different types of bonds) making it less likely to fall into an ordered structure.

Glasses are most often produced by melting a silica crystal structure (the most widely used structure is α -quartz) and cooling at a fast rate so that it does not have time to form crystals and to a temperature at which the atoms do not have sufficient energy to rearrange themselves into a crystal structure, reaching a meta-stable state. They can also be produced through pressurisation, grinding, irradiation or chemical reaction [34, p. 120]. A glassy structure is approximately 5% less dense than an equivalent crystal [35].

Pure silica glass is very durable: The Si-O bond is very strong (over 335 kJ/mol [36]). The melting point of silica is high, at 1986 K [37, p. 9], and its linear coefficient of thermal expansion is low at $0.25 * 10^{-6}/^{\circ}\text{C}$ [38, p. 345]. If an exceptionally durable glass is required pure silica can be used, otherwise other materials are usually added to lower the melting point, making production easier and less expensive. The melting point of a typical soda-lime glass is approximately 1770 K [31, p. 264] (soda-lime glass is the most commonly used glass and is comprised of 70-75% SiO_2 , 13-17% Na_2O , 5-10% CaO and 1-5% other oxides such as B_2O_3 , Al_2O_3 and MgO [36]). Its linear coefficient of expansion coefficient, however, is much larger at $100 * 10^{-6}/^{\circ}\text{C}$ [38, p. 345]. Different materials and different proportions of those materials are added to silica to achieve

different properties for the glass. For example, a larger proportion of B_2O_3 is present in a boro-silicate (81% SiO_2 , 13% B_2O_3 , 4% Na_2O and 2% Al_2O_3 [36]) glass than in a soda-lime glass which lowers the linear coefficient of thermal expansion to $3 * 10^{-6}/^{\circ}C$ [38, p. 345].

The second and third themes of this thesis are to investigate the behaviour of amorphous silica under different conditions. Computational techniques can be used to investigate properties which are difficult or impossible to obtain from experiment. They are especially useful for the study of amorphous materials: Experimental diffraction techniques can only give average values [39] and although powerful local techniques are available, including NMR [40] and EXAFS [41], developing a detailed structural model is still difficult. Computational techniques enable structural models to be fitted to experimental data which can then be interrogated to provide data on a wide range of properties. The data can be more detailed, in the form of distributions rather than simple average values.

The work is described in two chapters: chapter 4 presents research on the structure and dynamics of a silica melt and vitreous structure at ambient pressure. Chapter 5 discusses the effect of pressure on glassy silica.

Several questions regarding amorphous silica were investigated:

- 1) The role of defects in a silica crystal on its melting behaviour.
- 2) The strength of the Si-O bond in a silica melt and the extent to which silicon and oxygen atoms move together.
- 3) The performance of the BKS potential [24] (introduced in section 2.3.2) in comparison to available experimental data.
- 4) The structural and dynamic properties of both a silica melt and vitreous structure for which no experimental data is available.
- 5) A number of different silica crystals were melted. Research was carried out to investigate whether the melts are all similar or whether their properties can be differentiated according to the original crystal structure.
- 6) A survey of the literature showed that no simulations for a silica melt using a shell model have been published (see section 2.3.1.6 for an explanation of a shell model). Research was carried out to investigate whether a shell model could be used to simulate a melt, with the potential being modified if necessary. If this was possible, the properties of this melt would be calculated.

7) The effect of the application and release of pressure on amorphous silica at high temperatures.

Chapter 2

Methodology

2.1 Free energy minimisation

Free energy minimisation (or lattice dynamics) is a technique for searching for a particular configuration of atomic coordinates which yields a stable structure. The multidimensional graph plotting free energy against atomic coordinates, temperature and pressure is denoted the free energy landscape or surface. The minima correspond to stable structures. The point with the lowest free energy is the global minimum and the other minima are local minima. Free energy minimisation calculations were carried out using the GULP code which was developed by J. D. Gale [42].

There are two measures of free energy: The Helmholtz free energy is used for constant volume experiments. The Gibbs free energy is used for constant pressure experiments. Most experiments in chemistry are at constant pressure, therefore the Gibbs free energy will be the measure used in this thesis.

The formula for Gibbs free energy is:

$$G = U + pV - TS \quad (2.1)$$

U is the internal energy.

p is the pressure.

V is the volume.

T is the temperature.

S is the entropy.

The internal energy (U) is the sum of the potential energy and the kinetic energy of the atoms in the structure.

The potential energy of a structure is defined as the energy released when atoms or ions are brought together from an infinite separation to their position in the structure. It is a function of the distances between atoms and the attractive and repulsive forces between them.

The multidimensional plot of atomic coordinates against potential

energy is denoted the potential energy landscape or surface. The potential energy landscape is described by a formula called an interatomic potential. Interatomic potentials are described in section 2.3. For a discussion of kinetic energy see section 2.2.6.1.

Although internal energy takes account of temperature, minimisation of the internal energy does not necessarily yield the most stable structure at a given temperature and pressure, as it does not take account of entropy.

In crystalline solids the major contribution to the entropy term is from vibrations. In free energy minimisation atoms are modelled as if they are vibrating harmonically around an equilibrium position. This method is called the “harmonic” approximation [43, p. 257]. A consequence of this is that free energy minimisation is only appropriate for simulating structures well below their melting point, where no diffusion can occur. This approximation can be extended to the “quasi-harmonic” approximation which allows the unit cell parameters of the structure to change [44, p. 76].

The three-dimensional matrix of second derivatives of the potential energy as a function of location for each atom in the structure is

called the Hessian matrix, which gives the force constant for harmonic vibration for each atom.

The formula for a simple harmonic oscillator is used to calculate the vibrational frequency of each atom:

$$v_i = \frac{1}{2\pi} \sqrt{\frac{k}{m}} \quad (2.2)$$

v_i is the vibrational frequency of atom i

k is the force constant.

m is the mass of the atom.

These frequencies can then be used to calculate the free energy using:

$$G = U + pV + \frac{1}{2} \sum_i hv_i + kT \sum_i \ln(1 - e^{hv_i/kT}) \quad (2.3)$$

U is the internal energy.

p is the pressure.

V is the volume.

h is Planck's constant ($6.626068 * 10^{-34} m^2 kg/s$).

v_i is the vibrational frequency of atom i .

T is the temperature.

k is the force constant.

The derivation of this formula is shown in [45, p. 38].

The atomic vibrations of a structure are more conveniently calculated in reciprocal space than real space [46, chapter 2]. The unit cell dimensions in reciprocal space are related to the reciprocal of the unit cell dimensions in real space. The coordinates in reciprocal space are called k-points. The more k-points sampled during a free energy minimisation calculation, the larger the number of possible vibrational modes that can be sampled, but the more computationally intensive the calculation.

Minima on the free energy landscape can be searched for using a number of possible algorithms. The method used in GULP is either the steepest descent method or the Newton-Raphson method, whichever is the most appropriate. The steepest descent method is based on calculating first derivatives and moving along the energy landscape in a direction in which the gradient is negative. The Newton-Raphson method is based on calculating second derivatives and is therefore more computationally intensive than steepest descent. However, since it calculates the rate of change of the gradient, it can choose a path where the gradient becomes more negative more quickly and therefore is more likely to find a configuration with a lower minimum. As the steepest descent algorithm approaches a minimum, a very small step is required in order to find the mini-

mum. With the Newton-Raphson technique, however, a larger step can be used because the rate of change of the gradient indicates the proximity to the minimum. Therefore, the steepest descent method is used at locations far from a minimum and the Newton-Raphson technique is used at locations close to a minimum. For more details of these algorithms see [42] or [47].

At low temperatures free energy minimisation is often the method of choice over molecular dynamics (MD), which is described in the next section, as it takes account of zero point energy [48].

2.2 Molecular dynamics

At high temperatures dynamic effects, including diffusion, become increasingly important. MD simulations include these effects explicitly by simulating the evolution of a system with time.

MD is based on calculating the acceleration of each atom by solving Newton's classical equation of motion:

$$\textit{Acceleration} = \textit{Force}/\textit{Mass} \quad (2.4)$$

The force is calculated by taking the derivative of the energy. As with free energy minimisation described above, the energy is calculated using an interatomic potential (described in section 2.3).

An MD simulation comprises a number of time steps. At each step the acceleration of each atom is calculated using the above formula and the atoms are moved accordingly.

The software used to perform MD simulations was DL_POLY, developed by W. Smith, T. R. Forester and I. T. Todorov [49].

2.2.1 Finite difference methods

The ideal MD simulation would be continuous, where the forces between all atoms are recalculated after an infinitesimally small movement of each atom. As this is not possible, finite difference methods with a sufficiently small time step are used. There are several finite difference methods. For MD simulations in this thesis the Velocity Verlet [50] method was used. It was chosen because it is one of the most accurate. Although it is not the fastest method, sufficient computer resources were available to allow its use.

In the Velocity Verlet method, the new positions of the atoms at each step are calculated using the velocity at time $t + \frac{1}{2}\delta t$ rather

than at time $t + \delta t$ (where δt is the size of the time step), as is the case with simpler algorithms. This is in order to make the new positions of the atoms closer to a function of the average velocity over the time step. This procedure has the disadvantage that the velocity has to be calculated at both $t + \delta t$ and $t + \frac{1}{2}\delta t$, making the calculations slower than a simpler algorithm.

There are two stages to the calculations:

In the first stage the velocities at time $t + \frac{1}{2}\delta t$ are calculated:

$$\underline{v}(t + \frac{1}{2}\delta t) = \underline{v}(t) + \frac{1}{2}\delta t \underline{a}(t) \quad (2.5)$$

$\underline{v}(t)$ is the velocity at time t .

$\underline{a}(t)$ is the acceleration at time t and is calculated using the formula:

$$\underline{a}(t) = \underline{f}(t)/m \quad (2.6)$$

$\underline{f}(t)$ is the force at time t .

m is the mass of the atom.

The new positions of the atoms at time $t + \delta t$ are then calculated:

$$\underline{r}(t + \delta t) = \underline{r}(t) + \delta t \underline{v}(t + \frac{1}{2}\delta t) \quad (2.7)$$

$\underline{r}(t)$ is the position at time t .

The new forces at time $t + \delta t$ are calculated using $\underline{r}(t + \delta t)$ and the atomic potentials described in section 2.3.

In stage 2 the velocities at time $t + \delta t$ are calculated:

$$\underline{v}(t + \delta t) = \underline{v}(t + \frac{1}{2}\delta t) + \frac{1}{2}\delta t \underline{a}(t + \delta t) \quad (2.8)$$

$\underline{a}(t + \delta t)$ is calculated using the formula:

$$\underline{a}(t + \delta t) = \underline{f}(t + \delta t)/m \quad (2.9)$$

2.2.2 Time step

When choosing the size of time step, a balance must be struck between it being large enough to enable a significant amount of phase space to be explored but not too large that the system becomes unstable due to excessive atomic displacements between time steps.

For simulations at low temperatures using the BKS potential (see section 2.3.2 for details of this potential) a search of time steps used in the literature indicated time steps between 1 femtosecond (fs) and 1.6 fs. Examples include: [51](1 fs), [52](1.6 fs) and [53](1.2 fs). A

time step of 1 fs was chosen for this work as this was at the bottom of the range of time steps.

For simulations at low temperatures using the Sanders potential (see section 2.3.3 for details of this potential) a time step of 0.2 fs was chosen as per [54]. The Sanders potential is a shell model and therefore a smaller time step is required, because the shell has a very small mass and can accelerate very quickly.

At higher temperatures, a shorter time step is advisable, since the particles are moving at a higher velocity with consequent larger atomic displacements.

For simulations of a melt using the BKS potential a search of time steps used in the literature resulted in time steps between 0.5 fs and 2 fs. Examples include [55](1 fs), [56](1.6 fs), [51](0.5 fs), [52](1.6 fs), [57](1 fs), [58](0.7 fs) and [59](2 fs). A time step of 0.5 fs was chosen in this work as this was at the bottom of the range of time steps.

For simulations of a melt using the Sanders potential a time step of 0.02 fs was chosen, for reasons discussed in section 4.10.

2.2.3 Initial velocities

As discussed in section 2.2.1, the velocities of the atoms at each step are calculated using a formula which is a function of the velocities at the previous step. This means that initial velocities must be assigned to the atoms. In DL_POLY the initial velocities are assigned at random according to a Maxwell-Boltzmann distribution. However, the sum of momenta of all the atoms must be equal to 0, to ensure that the entire simulation cell does not move. Additionally the sum of the kinetic energy of all the atoms must correspond to the temperature of the simulation, which is achieved by ensuring that the following formula holds:

$$\frac{1}{2} \sum_{i=1}^N m_i v_i^2(0) = \frac{3}{2} N k_B T \quad (2.10)$$

i is the index for an atom.

v is the velocity.

m is the mass.

N is the number of atoms.

k_B is the Boltzmann constant ($1.381 * 10^{-23} J/K$).

T is the simulation temperature.

2.2.4 Equilibration and simulation time

An MD simulation usually has an initial period of equilibration to allow the system to reach thermal equilibrium. In simulations in this work an equilibration period of 100,000 time steps was used. This value was chosen because test runs were carried out for all values of time step used in calculations in this thesis, which showed that this was a sufficient amount of time for initial fluctuations in values such as energy and volume to settle.

The period following equilibration is referred to as the production phase. Measurements are only taken during this phase. The length of production phase used in simulations in this work was 100,000 time steps unless otherwise stated. This value was chosen because test runs were carried out with different lengths of production phase which showed that this was a sufficient amount of time for statistically significant data to be collected.

2.2.5 Periodic boundary conditions

The systems being modelled in this work are bulk structures. The greater the number of atoms in a simulation, the more accurate

the results: for example, a larger number of possible vibrational modes can be captured. In practice, due to limited computer power, simulations are limited to hundreds or thousands of atoms, where surface effects might still be significant. In order to model structures where the forces exerted on atoms are as similar as possible to those in bulk systems, the method of periodic boundary conditions is used, as illustrated in Figure 2.1.

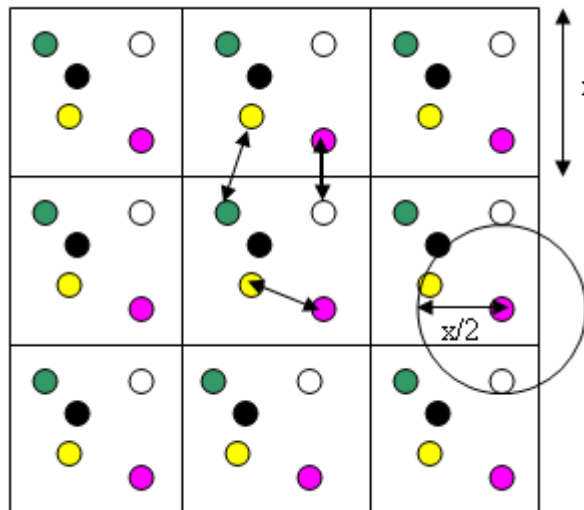


Figure 2.1: Periodic boundary conditions

The system is represented as an infinite three-dimensional series of copies of the structure (or simulation cell) being modelled, which eliminates surfaces. As shown in Figure 2.1, an atom can interact with another atom across the boundary of the simulation cell. Atoms can also move across the boundary.

The calculations would obviously be intractable if the structure was infinite. Therefore, the concept of a cut-off is introduced. An example of a cut-off is shown by the circle in figure 2.1 and is a distance from an atom beyond which short-range atom-atom interactions are not calculated (long-range electrostatic interactions are calculated beyond the cut-off and the method for dealing with this is discussed in section 2.2.7). The cut-off also serves another purpose in that it ensures that atoms cannot interact with their own image in an adjacent simulation cell. If the value of the cut-off is chosen such that it is half of the size of the shortest side of the simulation cell, each atom will interact with the maximum possible number of other atoms but without interacting with its own image. This rule is known as the Minimum Image Convention. In simulations in this thesis a cut-off of 8 Å was used unless a different value is specified. This value was chosen because it is less than half the length of the smallest side of the smallest unit cell of any of the structures simulated in this thesis. This choice ensures that all structures obey the Minimum Image Convention and that the final structures are easily comparable as all simulations have the same cut-off.

2.2.6 Ensembles

The type of ensemble specifies the properties of the system which are kept constant throughout a simulation. The simplest method, using the methods described so far, is in the NVE (microcanonical) ensemble: The number of atoms (N), the energy (E) and the volume (V) are kept constant. The volume is constant because when atoms move during a simulation they can move across the periodic boundary instead of the simulation cell expanding or contracting. This ensemble is not representative of typical experimental conditions and an ensemble where the pressure and/or temperature are constant but the volume and/or energy are allowed to fluctuate is often required.

2.2.6.1 Constant temperature simulations

The kinetic energy (KE) of a system is related to its temperature by:

$$\text{Kinetic energy} = \frac{3}{2}Nk_bT \quad (2.11)$$

N is the number of atoms.

k_b is the Boltzmann constant.

T is the temperature.

The kinetic energy of an atom is related to its velocity by the formula:

$$\textit{Kinetic energy} = \frac{1}{2} \textit{mass} * \textit{velocity}^2 \quad (2.12)$$

The temperature of a system can therefore be kept constant by keeping the sum of the squares of the velocities of all the atoms constant. This is achieved by rescaling the velocities at certain intervals. For MD calculations in this thesis the velocity rescaling was carried out at every time step.

2.2.6.2 Constant pressure simulations

In constant pressure simulations the volume of the simulation cell can change. There are two types of constant pressure ensembles. In an NPT ensemble the volume changes isotropically (by the same amount in all directions). In an $N\sigma T$ ensemble the volume can change anisotropically. As with constant temperature simulations, in constant pressure simulations the size and/or shape of the simulation cell is rescaled at certain intervals (every step in this thesis) in order to keep the pressure of the simulation constant.

2.2.6.3 Choice of ensemble

The ensemble used for the simulations described in this thesis, unless otherwise stated, is $N\sigma T$ (isothermal-isobaric). A constant temperature ensemble was chosen because various properties of silica as a function of temperature were studied. Additionally, glasses of silica were being simulated and such structures are produced by cooling a melt at a particular rate. The capacity to set the temperature at a particular value is therefore required. The constant pressure ensemble was similarly chosen because various properties as a function of pressure were studied. The crystal structures being simulated in this thesis are anisotropic and therefore volume change due to varying temperatures or pressures might occur by different amounts in different directions. The $N\sigma T$ ensemble was used therefore in preference to the NPT ensemble.

2.2.7 Ewald summation

The long-range electrostatic or charge-charge interactions (explained in section 2.3.1.1) converge very slowly in real space. It is therefore more efficient to calculate these types of interactions in reciprocal space.

Figure 2.2 shows a one-dimensional representation of the location of atoms in a structure and their charges. The value on the x-axis is the x-coordinate of an atom and the value on the y-axis is its charge.

In the method of Ewald summation a Gaussian function is added to each point charge. The mean value of this function is the value of the original point charge but with the opposite sign, as is shown in Figure 2.3.

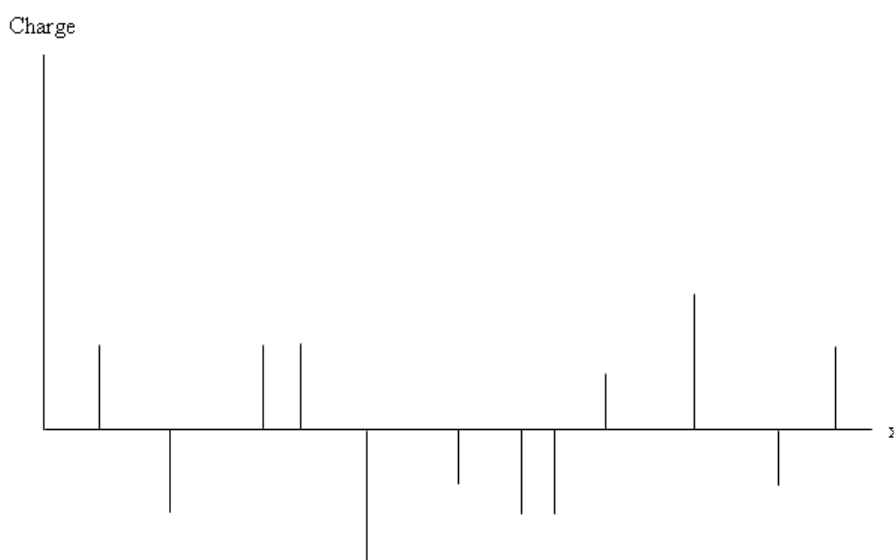


Figure 2.2: A 1 dimensional representation of the location of atoms and their charges

This new system must be evaluated in real space. However, it converges very quickly, since the overall amount of charge in the system has been reduced by the addition of the Gaussian functions with opposite signs to the original point charges. In order to calculate the

true energy of the system, Gaussian functions of the opposite sign of the first Gaussian functions must be added i.e. functions whose mean values are equal to the point charges. This is to cancel out the first set of functions which were added. These Gaussians are shown in Figure 2.4.

These functions converge slowly in real space. However, because they are Gaussian functions they can be evaluated in reciprocal space, in which they converge quickly.

The Ewald method enables the entire system to be represented by rapidly converging functions.

2.3 Potentials

An interatomic potential is a formula for calculating the potential energy of a system as a function of its atomic coordinates. The derivative of the energy is taken to calculate the force between atoms. There are a wide range of possible potentials and the choice of which interactions to include in the potential will depend on a number of factors, including the atomic species in the system, the computational capacity available and the nature of the energy landscape.

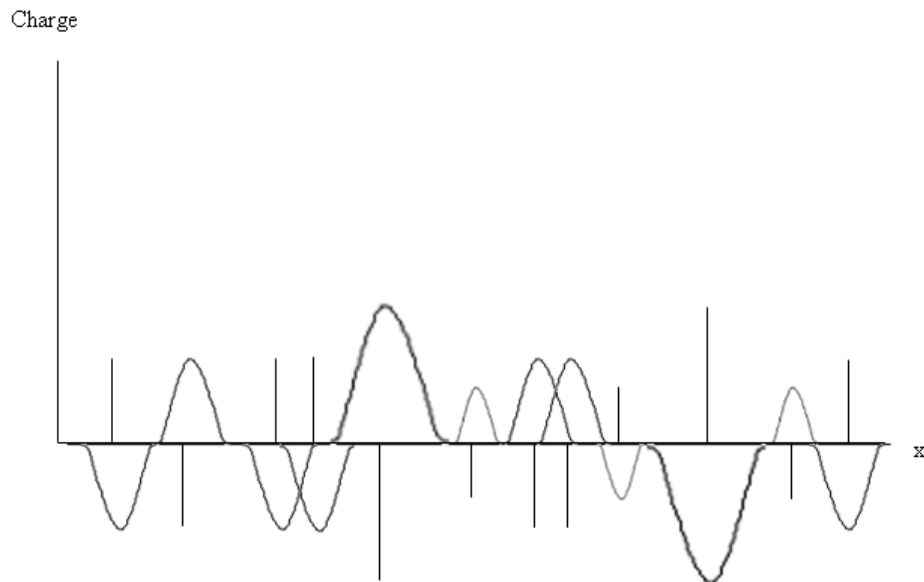


Figure 2.3: The point charges with Gaussians of opposite signs added

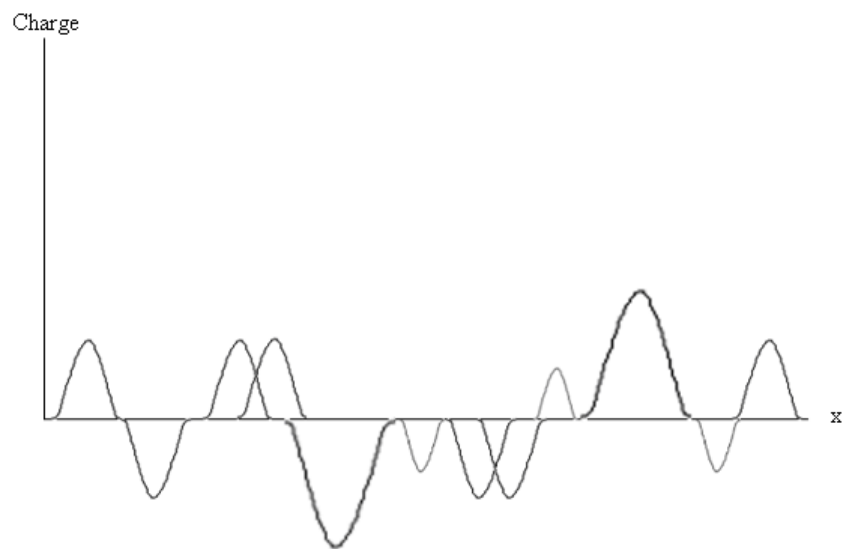


Figure 2.4: The Gaussians added to cancel out the first set of Gaussians

2.3.1 Forces

A potential is a sum of the different types of interactions between particles. The types of interactions used in this thesis are described below.

2.3.1.1 Electrostatics

Electrostatic forces are long range classical coulomb-coulomb interactions between charged particles:

$$E_{ij}(r_{ij}) = \frac{Q_i Q_j}{r_{ij}} \quad (2.13)$$

E_{ij} is the energy of the electrostatic interaction between two atoms.

i and j are species of atoms, e.g. Si or O.

r_{ij} is the distance between atoms i and j .

Q_i is the point charge of atom i .

2.3.1.2 Repulsion

There are a number of short range forces. The one which dominates is electron-electron repulsion. This force occurs when atoms come close enough for their electron clouds to overlap.

An example formula for repulsive interactions:

$$E_{ij}(r_{ij}) = A_{ij}e^{-B_{ij}r_{ij}} \quad (2.14)$$

A_{ij} and B_{ij} are parameterised constants.

2.3.1.3 Dispersion

Dispersion is an attractive force and arises from correlation effects of electrons resulting in induced-dipole induced-dipole interactions.

The formula (which is exact, as it is derived from second-order perturbation theory) for dispersive interactions is as follows:

$$E_{ij}(r_{ij}) = -\frac{C_{ij}}{r_{ij}^6} \quad (2.15)$$

C_{ij} is a constant.

2.3.1.4 Spring or bond stretch

In a spring or bond stretching term there is a preset equilibrium bond length that has the lowest energy. Deviations from this bond length have a higher energy and so this type of interaction is represented by a harmonic function.

An example formula for a bond stretch:

$$E_{ij}(r_{ij}) = k(r_{ij} - r_0)^2 \quad (2.16)$$

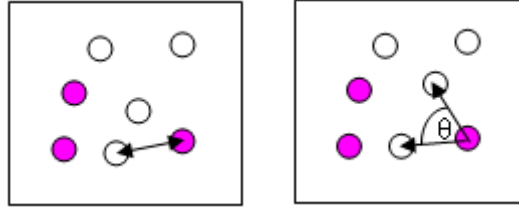
r_0 is the equilibrium bond length.

k is the strength of the spring (i.e. the amount of energy needed to make the bond length deviate from its equilibrium value).

2.3.1.5 Angle bending

The interactions described so far have been two body interactions, i.e. the total energy of the system is given by the sum of each atom interacting with every other atom, two atoms at a time. It can often be useful to introduce terms which depend on the coordinates of more than two atoms (called many body terms). In this thesis the largest number of atoms in a many body term is three. A term is added to the potential which is a function of the angle between three atoms, as illustrated in Figure 2.5.

The angle bending terms used in this thesis are similar to bond stretching terms in that an angle that is equal to a preset equilibrium value will have the lowest energy and if the angle deviates from this equilibrium value the energy becomes higher.



(a) Two body interactions (b) Three body interactions

Figure 2.5: Two and three body interactions

An example formula for an angle bending term:

$$E_{ijk}(r_{ijk}) = l(\Theta_{ijk} - \Theta_0)^2 \quad (2.17)$$

Θ_0 is the equilibrium angle.

Θ_{ijk} is the angle between atoms i , j and k .

l plays a similar role to the strength of the spring in bond stretching (i.e. the amount of energy needed to make the angle deviate from its equilibrium value).

Three body potentials are often used in simulations of silica because the basic building blocks (e.g. tetrahedra for low pressure polymorphs) are not easily deformed, i.e. the O-Si-O angles are quite rigid. The three body term ensures that these angles do not deviate greatly from an equilibrium value.

2.3.1.6 Shell model

A shell model is widely used to model polarisation. The atom is represented by two separate entities: the core (representing the nucleus and core electrons) and the shell (representing the valence electrons). The core and the shell separately interact with other atoms and also with each other. They also each have their own charge.

The core and shell interact with each other by a harmonic spring, as described in section 2.3.1.4, but where the equilibrium distance between them is set to 0. They interact with other atoms using a formula containing terms described in the previous sections.

The shell can be assigned a mass or it can be massless. In the case of a shell with a mass it is assigned a small fraction of the total mass of the atom (typically ≈ 0.05 a.m.u.). It has a small mass so that it can react quickly to changes in the location of its associated core. Since the shell has a mass, Newton's equation of motion can be used to calculate its acceleration. It is therefore treated in the same way as the core in its interactions with other atoms. Newton's equation of motion cannot be used in simulations with a massless shell because it would give an infinite force. The location of the shell is therefore calculated by statically minimising the force acting

on it. Although the massless shell model is the more realistic, it is more computationally intensive than the model with masses on the shells. The reason for this is that the massless shell model requires a number of iterations in order to obtain self consistent locations for all the shells.

2.3.2 The BKS potential

The BKS potential was developed by B. W. H. van Beest, G. J. Kramer and R. A. van Santen [24] for modelling low pressure silica crystal structures.

The parameters of the model (i.e. the values of the constants in the formula) were derived by iterating between the optimisation of bulk experimental properties (unit cell dimensions and elastic constants) and performing electronic structure calculations on a small silica cluster. Electronic structure calculations are computationally intensive and so can only be used for a relatively small number of atoms, which might give less accurate results for certain properties such as vibrational modes and bulk properties. The use of experimental data means that longer range interactions can be included in the fitting of the model parameters, therefore improving the accuracy of the prediction of certain properties.

Three of the interactions described in section 2.3.1 are included in this potential: electrostatics, repulsion and dispersion. It is of the form:

$$\Theta_{ij}(r_{ij}) = \frac{Q_i Q_j}{r_{ij}} + A_{ij} e^{-B_{ij} r_{ij}} - \frac{C_{ij}}{r_{ij}^6} \quad (2.18)$$

Θ_{ij} is the energy.

i and j are species of atoms, e.g. Si or O.

r_{ij} is the distance between atoms i and j .

A_{ij} , B_{ij} and C_{ij} are constants. $A_{Si-O} = 18003.7572$ eV, $A_{O-O} = 1388.7730$ eV, $B_{Si-O} = 4.87318$ Å⁻¹, $B_{O-O} = 2.76000$ Å⁻¹, $C_{Si-O} = 1133.5381$ eVÅ⁶ and $C_{O-O} = 175.0000$ eVÅ⁶.

The formula contains no Si-Si short range terms as these forces are negligible.

The Si-O bond is considered to be partially covalent and partially ionic [60]. In the BKS potential partial charges are assigned to the atoms in order to reflect this. Q_i is the point charge of atom i and $Q_{Si} = +2.4$ and $Q_O = -1.2$.

The BKS potential qualitatively reproduces the experimental silica phase diagram of quartz, coesite, stishovite and the liquid phase quite accurately, i.e. the shapes of the areas delimited by the lines separating the different structures and their proportions are compa-

rable. However, it is inaccurate quantitatively in that the location of the different phase boundaries differs significantly from experiment [61]. The potential also accurately reproduces the experimental elastic constants of α and β quartz [53] and [62].

2.3.3 The Sanders potential

This model was developed by M. J. Sanders, M. Leslie and C. R. A. Catlow [25]. The parameters of this model were calculated by fitting to experimental bulk properties (elastic constants and dielectric properties) of quartz. The model includes five of the interactions described in section 2.3: electrostatics, repulsion, dispersion, angle bending and a shell component.

The two body effects are of the form:

$$\Theta_{ij}(r_{ij}) = \frac{Q_i Q_j}{r_{ij}} + A_{ij} e^{r_{ij}/-B_{ij}} - \frac{C_{ij}}{r_{ij}^6} \quad (2.19)$$

$A_{Si-O} = 1283.9073$ eV, $A_{O-O} = 22764.0000$ eV, $B_{Si-O} = 0.3205$ Å, $B_{O-O} = 0.149$ Å, $C_{Si-O} = 10.6616$ eVÅ⁶ and $C_{O-O} = 27.88$ eVÅ⁶.

The potential is a full charge model: $Q_{Si} = 4$, $Q_{O_{core}} = +0.8482$ and $Q_{O_{shell}} = -2.8482$.

i and j can be a silicon atom, an oxygen core or an oxygen shell.

The repulsion and dispersion terms usually exclude oxygen core and silicon core interactions as they are negligible. The shell is given a mass of 0.05 a.m.u.

The three body term is given by:

$$\Theta_{ijk}(r_{ijk}) = k_{3b}(\Theta_{ijk} - \Theta_0)^2 \quad (2.20)$$

i , j and k are always oxygen, silicon and oxygen, respectively.

Θ_{ijk} is the actual angle between three atoms.

Θ_0 is the ideal O-Si-O angle (109.47°).

k_{3b} is a constant and takes the value 2.097.

The core-shell interaction is given by the formula:

$$\Theta_{core-shell} = \frac{1}{2}k_{core-shell} r_{core-shell}^2 \quad (2.21)$$

$r_{core-shell}$ is the distance between the core and the shell.

$k_{core-shell}$ is the strength of the harmonic spring and has the value 74.9204.

Only oxygen atoms are modelled as a separate core and shell, as silicon atoms are positively charged and are therefore not significantly polarisable.

Although this potential was parameterised using the properties of

α -quartz it accurately reproduces the unit cell parameters of α -cristobalite, β -cristobalite and MX1 tridymite [63].

2.4 Electronic structure calculations

Electronic structure calculations form only a small part of the work in this thesis. They will therefore be described only briefly.

The methods discussed thus far model each atom (or core and shell) as a single entity. Electronic structure calculations model the electrons and nucleus separately. They are based on solving the Schrödinger equation:

$$\mathbf{H}\Psi = E\Psi \quad (2.22)$$

\mathbf{H} is the Hamiltonian operator

E is the total energy of a particle

Ψ is the wave function of the particle

An exact solution for this equation can only be obtained for one electron systems. Therefore, although electronic structure calculations require no input parameters (such as the repulsive and dispersion terms in the pair potentials described previously), several approximations must be made when solving the Schrödinger equation for

all other systems. Prior to the development of Density Functional Theory (DFT), electronic structure methods, notably Hartree-Fock methods, calculated the wave function using the variational principle. DFT is based on the concept of charge density, from which energy and other properties are calculated. For a more detailed explanation see [64].

The basis set used in calculations in this thesis was DND (Double Numerical plus d-functions). For this basis set calculations are made using two possible atomic orbitals (a ground state and an excited state) for each electron. In addition there is a polarisation d-function on all non-hydrogen atoms. For calculations in this thesis the Local Density Approximation (LDA) was used with PWC (Perdew-Wang) exchange-correlation functionals [65]. The maximum number of possible iterations was set to 200. The real space cut-off was set to 3.5 Å. The calculations were performed using the DMol3 code [66].

2.5 Properties

2.5.1 Pair Distribution Function

The Pair Distribution Function (PDF) provides information on the distance between atoms. The number of other atoms at distance r

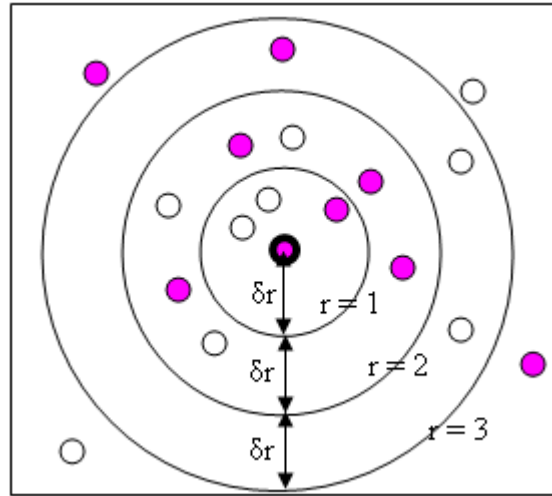


Figure 2.6: Calculation of a Pair Distribution Function (PDF)

from each atom, averaged over all atoms is calculated. In this thesis partial PDFs are calculated, where Si-O, Si-Si and O-O PDFs are calculated separately. The PDF, represented by $g(r)$, is calculated by taking each atom in the structure individually as a central atom and dividing the area round the atom into shells of thickness δr . The number of atoms in each shell is counted. Figure 2.6 shows an example of this. The silicon atoms are coloured pink and the oxygen atoms are coloured white. If the Si-O PDF was being calculated the number of oxygen atoms in the first shell surrounding the central atom (shown in bold) would be 2 and the numbers in the second and third shells would be 3 and 2 respectively. If the Si-Si PDF was being calculated the number of silicon atoms in the first shell surrounding the central atom would be 1 and the numbers in the

second and third shells would be 4 and 1 respectively.

This procedure is repeated for all atoms and then averaged over all atoms giving $\langle n(r) \rangle$.

The volume of each shell increases with increasing r . $\langle n(r) \rangle$ is therefore normalised by dividing by an approximation to the volume of the shell. The volume of the shell is:

$$Volume = \frac{4}{3}\pi(r + \delta r)^3 - \frac{4}{3}\pi r^3 \quad (2.23)$$

which is equal to:

$$Volume = 4\pi r^2(\delta r) + 4\pi(\delta r)^2 + \frac{4}{3}\pi(\delta r)^3 \quad (2.24)$$

This is approximated to:

$$Volume \approx 4\pi r^2(\delta r) \quad (2.25)$$

This calculated value is then normalised so that it can be compared with other structures by dividing by the density of the entire structure (ρ).

The formula for $g(r)$ is therefore:

$$g(r) = \frac{\langle n(r) \rangle}{\rho 4\pi r^2 (\delta r)} \quad (2.26)$$

2.5.2 Mean Square Displacement

The Mean Square Displacement (MSD) provides information on the distance atoms move from their original starting site during a simulation. It is the square of the difference between the initial coordinates of an atom and its final coordinates, averaged over all atoms.

It is given by the formula:

$$\langle r_i^2(t) \rangle = \frac{1}{N} \sum_{i=1}^N (\underline{r}_i(t) - \underline{r}_i(0))^2 \quad (2.27)$$

i is an index for an atom.

N is the total number of atoms.

$\underline{r}(t)$ represents the coordinates of an atom at time t .

2.5.3 Diffusion coefficient

The MSD is a function of the difference between the initial coordinates of an atom and its final coordinates. Because atoms are

vibrating, it will always be non-zero, even in a solid. This may make it difficult to ascertain whether a structure has melted and diffusion is occurring. The diffusion coefficient [67] takes account of vibrations and will take the value zero in a solid. It is given by the relationship:

$$D = \frac{1}{6} \lim_{t \rightarrow \infty} \frac{d}{dt} \langle (\underline{r}_i(t) - \underline{r}_i(0))^2 \rangle \quad (2.28)$$

2.5.4 Velocity Autocorrelation Function and Vibrational Density of States

An autocorrelation function shows the correlation between different points in time of a particular property of a particle. Figure 2.7 has an example of a velocity autocorrelation function.

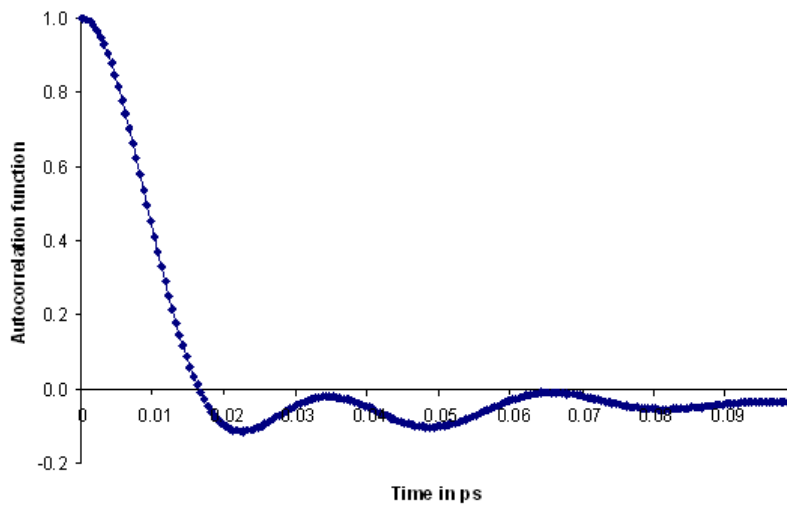


Figure 2.7: An example of a velocity autocorrelation function (for liquid silica)

A Fourier transform of the velocity autocorrelation function produces the vibrational density of states or vibrational spectrum. It is a plot with frequency of vibration on the x-axis and the number of atoms vibrating at this frequency on the y-axis. It does not, however, give any information about the character of the vibrations, e.g. whether they are bond stretching, angle bending, etc.

2.5.5 Arrhenius plots

It is useful to represent the temperature dependence of the diffusion coefficients as an Arrhenius plot of $\ln D$ (diffusion) against $1/T$ (temperature). It gives an indication of the ability of the atoms in a structure to rearrange themselves at different temperatures as a material is being heated or quenched. A material is a strong glass former if the Arrhenius plot results in a near straight line [68]. The Arrhenius plot of a fragile glass is curved. A strong glass has a significant amount of short range order [31, p. 121], whereas a fragile glass does not. This is because as a fragile glass is cooled, there will come a point where the diffusion coefficient decreases quite suddenly (due to the Arrhenius plot being curved) and the configuration of the melt is frozen in more quickly than it would be for a strong glass former.

The equation:

$$\ln D = \ln A - \frac{E_a}{RT} \quad (2.29)$$

is called the Arrhenius equation [69, p. 792]. A linear Arrhenius plot allows the activation energy to be calculated.

R is the gas constant (8.31447 J/K Mol).

A is called the pre-exponential factor.

E_a is the activation energy. This is the height of the energy barrier which needs to be overcome in order for the system to take on a different configuration.

2.6 Programs

All programs for analysing the properties of the structures were written by the author, with the exception of programs to analyse:

- 1) The density of states: The code used was developed by W. Smith as a utility for the DL_POLY code [49].
- 2) Torsion angles: The GULP code was used, which was developed by J. D. Gale [42].

The programs are available from the author, as are output files containing structures and their properties from simulations.

Chapter 3

An exploration of the silica polymorph tridymite

The work discussed in this chapter uses three computational techniques, free energy minimisation, molecular dynamics (MD) and Density Functional Theory, to investigate the silica polymorph tridymite. As discussed in section 1.2, tridymite is a particularly interesting polymorph, having been found to exist in a large number of different atomic configurations. The aims of this chapter are described in section 1.2 on page 26.

3.1 Free energy minimisation

3.1.1 Methodology

Free energy minimisation calculations (methodology described in section 2.1) were carried out for a range of temperatures at ambient pressure for six tridymite structures. Free energy includes the vibrational entropy term and was used in preference to static lattice energy minimisation because simulations at high temperatures were being carried out. The simulations were at constant pressure and using the Zero Static Internal Stress Approximation (ZSISA) [42]. Simulations were run for a range of supercell sizes and shapes and for several different numbers of k-points, ranging from 1 to 15.

Calculations were carried out using two different potentials:

The BKS potential (see section 2.3.2 and [24] for details) is a rigid ion model and was chosen because it is one of the most successful and widely used potentials for modelling silica structures at low pressures.

The Sanders potential (see section 2.3.3 and [25] for details) was chosen because it differs from the BKS potential: it is a shell model

and so includes polarisation. It also includes 3 body terms. As with the BKS potential it has also been used successfully for modelling low pressure polymorphs of silica.

3.1.2 Results

Section 3.1.2.1 discusses results for final atomic configurations and section 3.1.2.2 discusses results for final energies and volumes.

3.1.2.1 Final atomic configuration

Table 3.1 contains data on final structures obtained using free energy minimisation for the BKS potential with 3 k-points and at ambient pressure. The first column contains the starting structure of the calculation. The numbers in the second column refer to the size and shape of the supercell, e.g. 212 means that the length of the primitive unit cell is doubled in the a and c directions. The fourth column contains information on the appearance of the final structure and is for simulations at 273 K. The fifth column has the same information for simulations at 700 K. The final structures were categorised by visual inspection and also analysis of Si-O-Si angles. N/A means that the calculation did not achieve a minimised structure. Where

two structures are given, the final structure was part way between the two crystal structures.

A number of different final structures were obtained from the simulations. The final structure and starting structure appear to be weakly correlated. However, the results are not consistent with the tridymite phase diagram that has been obtained from experimental studies [8] (the temperature ranges for these are given in section 1.2), where the final structure would be determined by the temperature of the simulation. For example, some simulations with LHP tridymite as the starting structure (the highest temperature form) minimised to HP tridymite at a temperature (273 K) where MX1 tridymite (the lowest temperature form) would be expected to be the most stable structure.

Moreover, two simulations with the same starting polymorph but different supercell sizes and shapes often minimised to different final structures. For example, at 273 K, simulations with MX1 as the starting structure resulted in OC tridymite as the final structure with a super cell size of 122, but resulted in OP tridymite as the final structure with a super cell size of 221.

Starting structure	Supercell shape	Appearance of final structure most similar to crystal structure (0 K)	Appearance of final structure most similar to crystal structure (273 K)	Appearance of final structure most similar to crystal structure (700 K)
HP	111	HP	HP	HP
	112	HP	HP	HP
	121	HP	HP	HP
	211	HP	HP	HP
	122	HP	HP	HP
	212	HP	HP	HP
	221	HP	HP	HP
	222	HP	HP	HP
	223	HP	HP	HP
	232	HP	HP	HP
	322	HP	HP	HP
	233	HP	HP	HP
	323	HP	HP	HP
	332	HP	HP	HP
	333	HP	HP	HP
LHP	111	Approximately HP	HP	N/A
	112	Approximately HP	No known structure	HP
	121	No known structure	HP/LHP	No known structure
	211	Approximately HP	No known structure	No known structure
	122	Approximately HP	No known structure	HP/LHP
	212	Approximately LHP	No known structure	Approximately HP
	221	Approximately OC	No known structure	Approximately LHP
	222	Approximately OC	HP	Approximately LHP
	223	Approximately OC	HP	Approximately LHP
	232	Approximately MX1	HP	Approximately HP
	322	HP	Approximately HP	OC
	233	N/A	HP	Approximately HP
	323	Approximately HP	Approximately LHP	Approximately HP
	332	Approximately OC	Approximately LHP	Approximately HP
	333	Approximately HP	OC/LHP	HP
OC	111	No known structure	No known structure	No known structure
	112	No known structure	No known structure	OC
	121	Approximately OC	No known structure	No known structure
	211	No known structure	Approximately OC	Approximately OC
	122	Approximately OC	Approximately OC	Approximately OC
	212	Approximately OC	OC	No known structure
	221	Approximately OC	Approximately OC	OC
	222	N/A	Approximately OC	N/A
	223	Approximately OC	N/A	Approximately OC
	232	Approximately OC	Approximately OC	OC
	322	No known structure	Approximately OC	Approximately OC
	233	Approximately OC	Approximately OC	OC
	323	Approximately OC	OC	OC
	332	Approximately OC	OC	OC
	OP	111	Approximately OC	Approximately OC
112		Approximately OC	OP	Approximately OP
121		No known structure	OP	OP
211		N/A	OP	OP
122		No known structure	OP	OP
212		No known structure	OP	OP
221		OP	OP	OP
MC	111	Approximately OC	OP	N/A
	112	No known structure	No known structure	No known structure
	121	No known structure	No known structure	OC
	211	Approximately OC	MC	MC
	122	No known structure	No known structure	OC
	212	Approximately OC	MC	OC
	221	No known structure	MC	OC
	222	Approximately OC	No known structure	MC/OC
	223	Approximately OC	Approximately MC	MC/OC
	232	No known structure	Approximately MC	MC/OC
	322	Approximately OC	Approximately MC	MC/OC
	233	Approximately OC	Approximately MC	MC/OC
	323	Approximately OC	Approximately MC	MC/OC
	332	Approximately OC	Approximately MC	MC/OC
	MX1	111	N/A	MC
112		No known structure	Approximately MC	No known structure
121		N/A	No known structure	OP
211		N/A	No known structure	OC/OP
122		No known structure	OC	OC/OP
212		Approximately OC	N/A	N/A
221		Approximately OC	OC	Approximately OP
222		No known structure	N/A	Approximately OP

Table 3.1: Final structures for free energy minimisation for the BKS potential with 3 k-points, at ambient pressure for two different temperatures

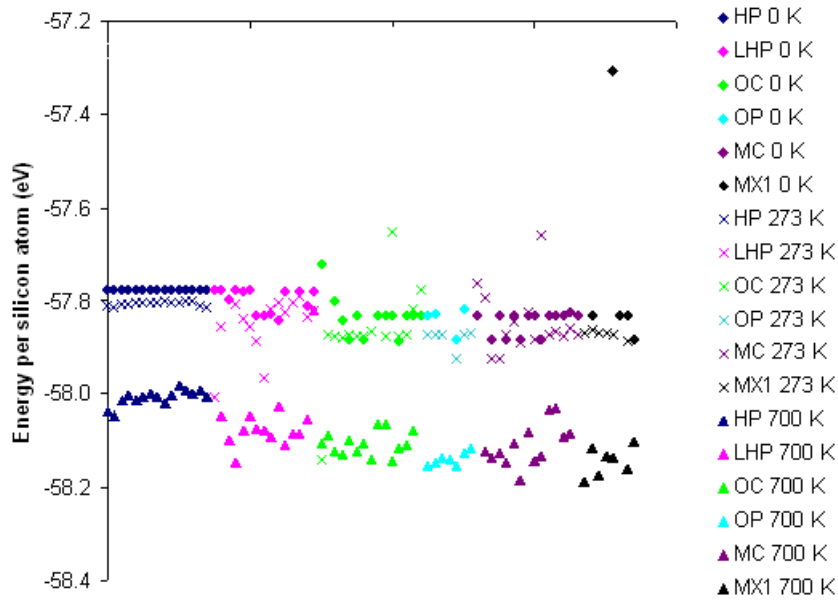


Figure 3.1: Energies in eV for free energy minimisation using the BKS potential with 3 k-points, at ambient pressure for two different temperatures. Each point on the x-axis refers to a row in table 3.1, from HP tridymite with a supercell size of 111 to MX1 tridymite with a supercell size of 222

3.1.2.2 Energy and volume

Figures 3.1 and 3.2 show resulting energies and volumes respectively for the simulations in table 3.1. Each point along the x-axis refers to a row in the table above, i.e. the first point is for simulations for HP tridymite with a supercell size of 111 and the last point is for simulations for MX1 tridymite with a supercell size of 222. The experimental values for volume were taken from [7] and [8]. 21 out of 222 simulations did not achieve a minimised structure and are not shown in the figures.

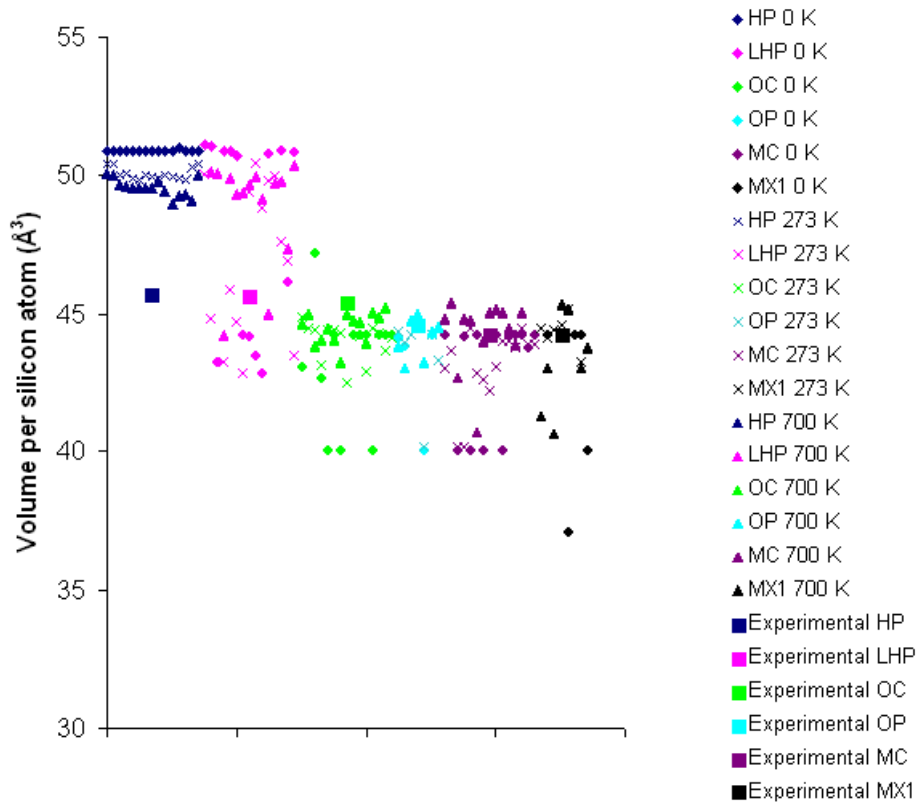


Figure 3.2: Volumes in \AA^3 for free energy minimisation using the BKS potential with 3 k-points, at ambient pressure for two different temperatures. Each point on the x-axis refers to a row in table 3.1, from HP tridymite with a supercell size of 111 to MX1 tridymite with a supercell size of 222

The structures appear to fall into two groups. The first group contains HP tridymite and LHP tridymite as starting structures. This group has similar volumes of approximately 50\AA^3 (per silicon atom), with energies of approximately -57.78 eV (per silicon atom) for simulations at 0 K, -57.80 eV for simulations at 273 K and -58.00 eV for simulations at 700 K. The second group contains the remaining starting structures with similar volumes of approximately 45\AA^3 and energies of approximately -57.83 eV for simulations at 0 K, -57.87 eV

for simulations at 273 K and -58.12 eV for simulations at 700 K.

We note from the graphs that there is a correlation between the temperature of the simulation and the final free energy. There does not, however, appear to be a strong correlation between the temperature of the simulation and the resulting volume.

There is greater variation in the volumes than would be expected from experimental data. The experimental value for the volumes of HP, LHP, OC, OP, MC and MX1 tridymite are 45.70 \AA^3 , 45.62 \AA^3 , 45.38 \AA^3 , 44.57 \AA^3 , 44.24 \AA^3 and 44.22 \AA^3 respectively [8]. Resulting volumes from simulations are spread over the range 40.0482 \AA^3 and 50.4432 \AA^3 .

Within each of the two groups (the first group containing the HP and LHP structures and the second group containing the remaining structures as described above) there is as much variation between different sized and shaped supercells within one polymorph as between different polymorphs. For example, for simulations at 273K, volumes for OC tridymite range from 40.05 \AA^3 and 47.19 \AA^3 for the different supercell sizes and shapes, and those for MC tridymite range from 40.05 \AA^3 and 44.25 \AA^3 .

The simulations were run using a number of different k-points, ranging from 1 to 15 and also using the Sanders potential. These simulations yielded similar results to those described above.

3.2 Molecular Dynamics

3.2.1 Methodology

Molecular dynamics (MD) was used next (methodology described in section 2.2) to model the structural properties of tridymite. As discussed in section 2.1, energy minimisation is a suitable technique for simulations at low temperatures but is less appropriate at high temperatures because it uses the harmonic approximation and anharmonic effects are not taken into account. MD can simulate anharmonic effects and is therefore often more accurate at higher temperatures. Additionally, free energy minimisation is most suitable for exploring energy landscapes with a small number of deep minima, because it explores less phase space, whereas MD is more appropriate for exploring an extensive and flat energy landscape (where the energy barriers to move from one atomic configuration to another are low). It is likely that the energy landscape of tridymite is quite

flat, as transitions between the different structures require no breaking of bonds. DL_POLY [49] was therefore used for MD simulations using the same six structures and same two potentials as for free energy minimisation.

The calculations were performed using the $N\sigma T$ ensemble and periodic boundary conditions with Ewald summation with a cut-off of 8 Å. As discussed in section 2.2.5, this value was chosen because it is less than half the length of the smallest side of the smallest unit cell of any of the tridymite structures, which ensures that all structures obey the Minimum Image Convention. Also, the final structures are more easily comparable if all simulations have the same cut-off. The Hoover thermostat (see [49] for details) was initially chosen as the mechanism for keeping the temperature constant because it is the most commonly used thermostat in simulations of silica. However, this resulted in the volume for all structures fluctuating throughout the simulations by as much as 10%, even at very low temperatures. Simulations with different relaxation times altered the amount of fluctuation but did not eliminate it entirely. The Berendsen thermostat (see [49] for details) eliminated the fluctuation and was therefore chosen instead of the Hoover thermostat. The thermostat relaxation time used was 1 ps and the barostat re-

laxation time was 5 ps. As discussed in section 2.2.2 a time step of 1 fs was employed for the BKS potential and a time step of 0.2 fs for the Sanders potential. All calculations were at ambient pressure. A shell with a mass of 0.05 a.m.u. was used for the Sanders potential. The range of temperatures used was between 1 K and 1600 K.

3.2.2 Results

Section 3.2.2.1 discusses results for final energies and volumes and section 3.2.2.2 discusses results for final atomic configurations.

3.2.2.1 Energy and volume

In contrast to the free energy minimisation calculations, where the final energy and volume could be approximately predicted depending on whether the starting structure was in the HP and LHP group or in the other group, for MD calculations no relationship could be found between the starting structure and the energies and volumes of the final structures. For some of the structures, calculations were carried out for several sizes of supercell. Tables 3.2 and 3.3 compare the resulting energies and volumes for calculations at 273 K using the BKS and Sanders potentials respectively.

Starting structure	Number of Si atoms	Energy per Si atom (eV)	Volume per Si atom (\AA^3)	Experimental volume (\AA^3)
HP	500	-58.0180	41.3660	45.70
	1372	-58.0182	40.9825	
	2048	-58.0371	40.0122	
LHP	500	-58.0180	41.3660	45.62
	1372	-58.0219	40.9796	
	2048	-58.0371	40.2886	
OC	512	-58.0332	40.4570	45.38
	1000	-58.0480	39.616	
OP	1536	-58.0547	39.5944	44.57
MC	512	-58.0566	39.6035	44.24
	1000	-58.0360	40.2690	
MX1	384	-58.0573	39.5990	44.22

Table 3.2: Energies and volumes of final structures using MD with the BKS potential at 273 K

Starting structure	Number of Si atoms	Energy per Si atom (eV)	Volume per Si atom (\AA^3)	Experimental volume (\AA^3)
HP	500	-128.4340	45.8980	45.70
	864	-128.4375	45.9109	
	1372	-128.4329	45.9300	
LHP	500	-128.4360	45.9660	45.62
	864	-128.4375	46.0058	
	1372	-128.4329	46.0058	
OC	512	-128.4336	45.9395	45.38
OP	1536	-128.4375	45.6797	44.57
MC	1000	-128.4300	45.9270	44.24
MX1	384	-128.4349	45.8802	44.22
	1296	-128.4336	45.9298	

Table 3.3: Energies and volumes of final structures using MD with the Sanders potential at 273 K.

It can be seen that there is at least as much variation within different supercell sizes and shapes of a particular structure as between different structures.

The calculated volumes for simulations using the Sanders potential are closer to experimental data than for those using the BKS potential.

In contrast to the free energy minimisation calculations, the variation in volume between the different starting structures is more comparable with experimental data. The experimental volumes for structures range from 44.22 \AA^3 to 45.70 \AA^3 . The volumes for MD simulations for the BKS potential are in the range 39.5990 \AA^3 to 41.3660 \AA^3 and those for the Sanders potential are in the range 45.6797 \AA^3 to 46.0058 \AA^3 . Resulting volumes for free energy minimisation were in the range 40.1982 \AA^3 and 50.4432 \AA^3 , although a larger number of simulations were carried out using that method so greater variation would be expected.

At the temperatures at which simulations reported here are being carried out it would be expected that simulations at higher temperatures would have both a higher energy and volume than simulations at low temperatures. For energy, this was observed for the majority of simulations. For volume, however, this was often not the case. Tables 3.4 and 3.5 illustrate this for HP tridymite with 500 silicon atoms as the starting structure for simulations using the BKS and Sanders potentials respectively. The simulation using the BKS po-

tential at 1100 K is inconsistent with the trend of the remaining simulations which is a rise in volume with increasing temperature. Table 3.5 shows that simulations using the Sanders potential display a trend of decreasing volume with increasing temperature.

Temperature (K)	Energy per Si atom (eV)	Volume per Si atom (\AA^3)
300	-58.0180	40.3020
700	-57.6900	42.1220
900	-57.5360	42.5060
1100	-57.4000	41.7100
1600	-57.0000	43.1080

Table 3.4: Energies and volumes using MD with the BKS potential for HP tridymite as the starting structure with 500 silicon atoms

Temperature (K)	Energy per Si atom (eV)	Volume per Si atom (\AA^3)
300	-128.4100	45.9300
700	-128.1160	45.7200
900	-127.9660	45.8260
1100	-127.8300	45.3360
1600	-127.4460	45.2600

Table 3.5: Energies and volumes using MD with the Sanders potential for HP tridymite as the starting structure with 500 silicon atoms

3.2.2.2 Final atomic configurations

As with free energy minimisation, the final structures were not consistent with the phase diagram that has been obtained from experiments. For the BKS potential each simulation could be allocated to one of four groups according to their final structure. The allocation appears to be independent of temperature. In each simulation

the atoms reverted to their final structure within a small number of time steps. None of the four final structures are similar to any of the six tridymite crystal starting structures. Group 1 contains LHP tridymite with 500 silicon atoms, LHP tridymite with 1372 silicon atoms and HP tridymite with 1372 silicon atoms as starting structures. The final structure for this group is shown in Figure 3.3. Silicon atoms are green and oxygen atoms are blue. Group 2 contains OC tridymite with 1000 silicon atoms as starting structure. The final structure for this group is shown in Figure 3.4. Group 3 contains MX1 tridymite with 384 silicon atoms, OP tridymite with 1536 silicon atoms and MC tridymite with 512 silicon atoms as starting structures. The final structure for this group is shown in Figure 3.5. Group 4 contains HP tridymite with 500 silicon atoms, MC tridymite with 1000 silicon atoms and OC tridymite with 512 silicon atoms as starting structures. The final structure for this group is shown in Figure 3.6. Its appearance is similar to the final structure of group 3 except that it has two different types of ring: one has 2 fold symmetry and another has 3 fold symmetry.

There does not appear to be a pattern which determines to which final structure group a particular starting structure will belong. In addition, a polymorph of a particular supercell size may belong to

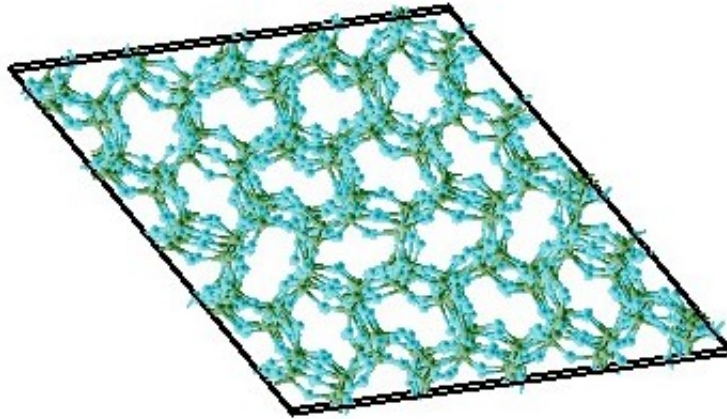


Figure 3.3: Final structure for group 1 using the BKS potential

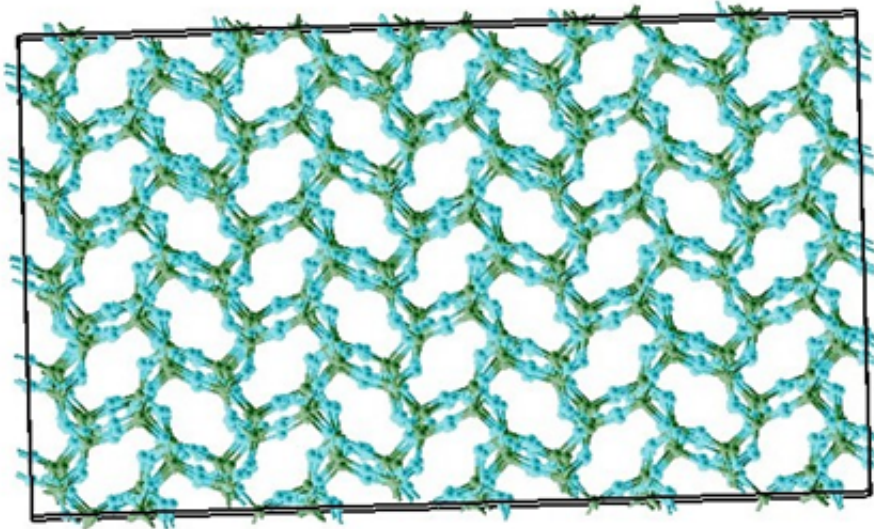


Figure 3.4: Final structure for group 2 using the BKS potential

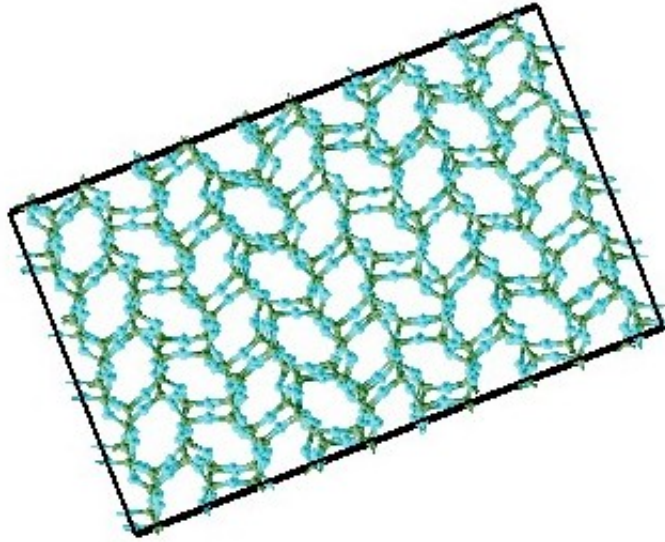


Figure 3.5: Final structure for group 3 using the BKS potential

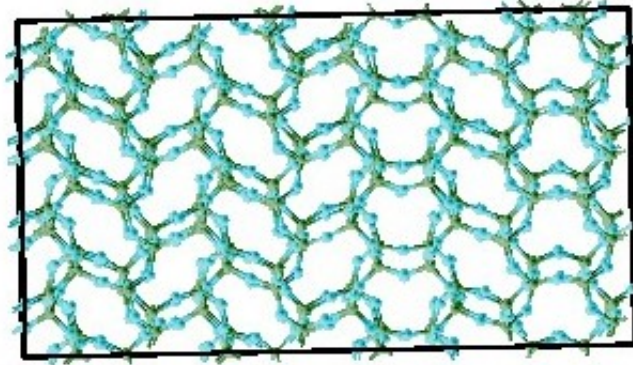


Figure 3.6: Final structure for group 4 using the BKS potential

one group, while the same polymorph but with a different supercell size may belong to another. For example, the HP polymorph with 500 silicon atoms at 273 K belongs to group 4 while the HP polymorph with 1372 silicon atoms at 273 K belongs to group 1. (It is interesting to note that although more ordered than the structure obtained from compression of the zeolite silicalite-1-F by J. Haines et al. [70], the four structures bear some resemblance to it in the rings being a full shaped and in the large variation in Si-O-Si angles).

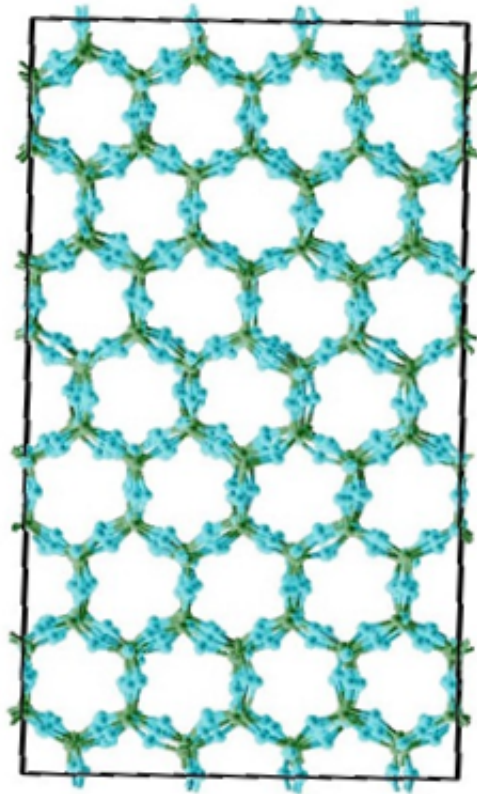


Figure 3.7: Final structure for all starting structures using Sanders

All simulations using the Sanders potential resulted in the structure

in Figure 3.7.

3.2.2.2.1 Pair Distribution Functions

Figures 3.8 - 3.10 show PDFs for the four final structures using the BKS potential.

In comparison to the PDFs of the tridymite crystal structures in Figures 1.7 - 1.9 (on pages 23 - 24), all of the PDFs above have wider and shorter peaks, indicating a lower level of symmetry.

Of the tridymite structures found in nature, the final structure obtained from all Sanders simulations appears to be most similar to the LHP polymorph. Figures 3.11 - 3.13 compare the PDFs of the final structure using the Sanders potential and those of LHP tridymite. Although the width and height of the peaks are very different, their locations generally coincide. It is therefore possible that the Sanders potential simulations are fluctuating about an average structure of the LHP polymorph. This topic is discussed further in section 3.2.2.2.4 which analyses the Si-O-Si angles.

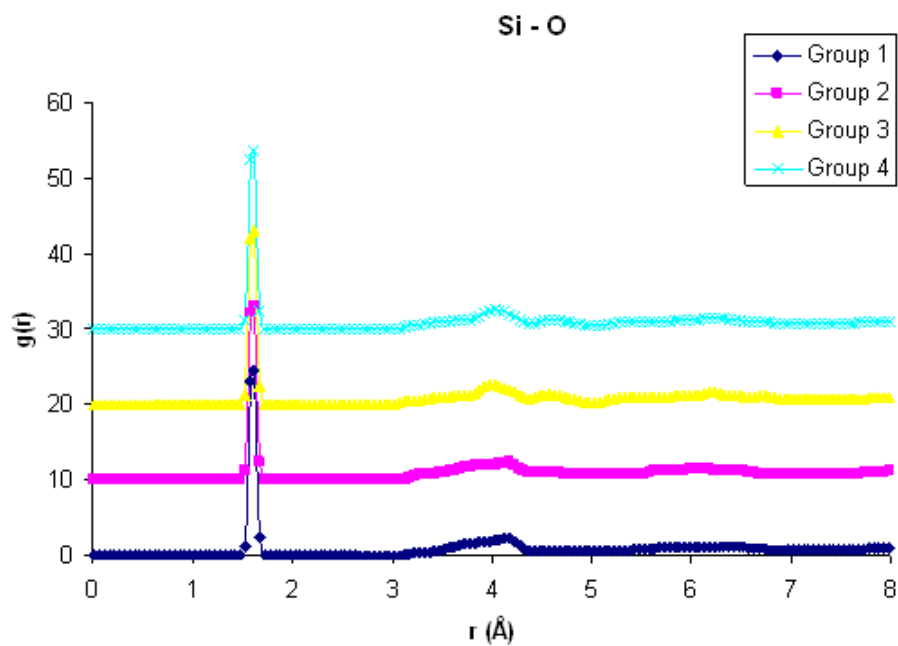


Figure 3.8: Si-O PDF for the four final structures using BKS

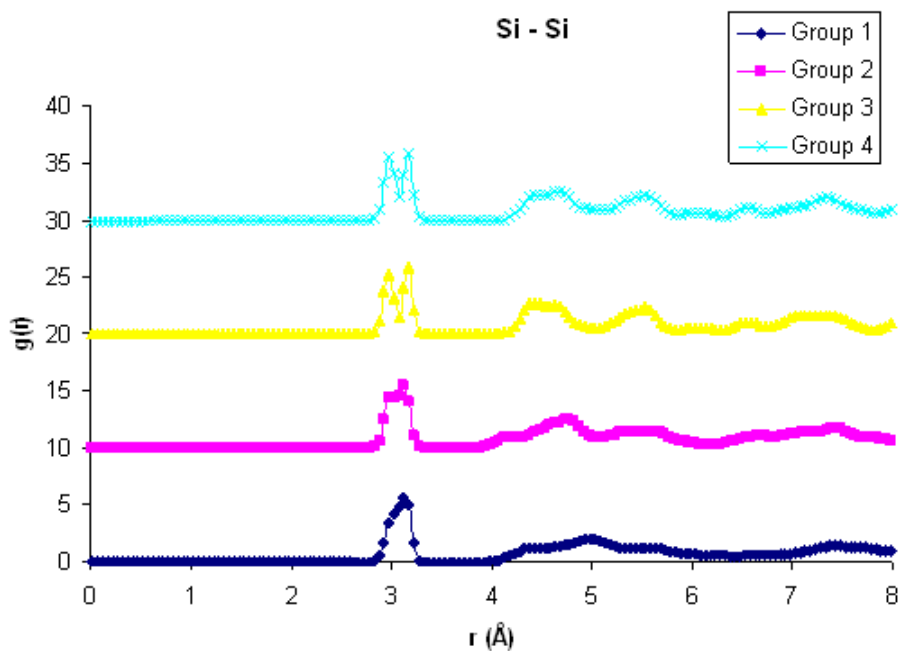


Figure 3.9: Si-Si PDF for the four final structures using BKS

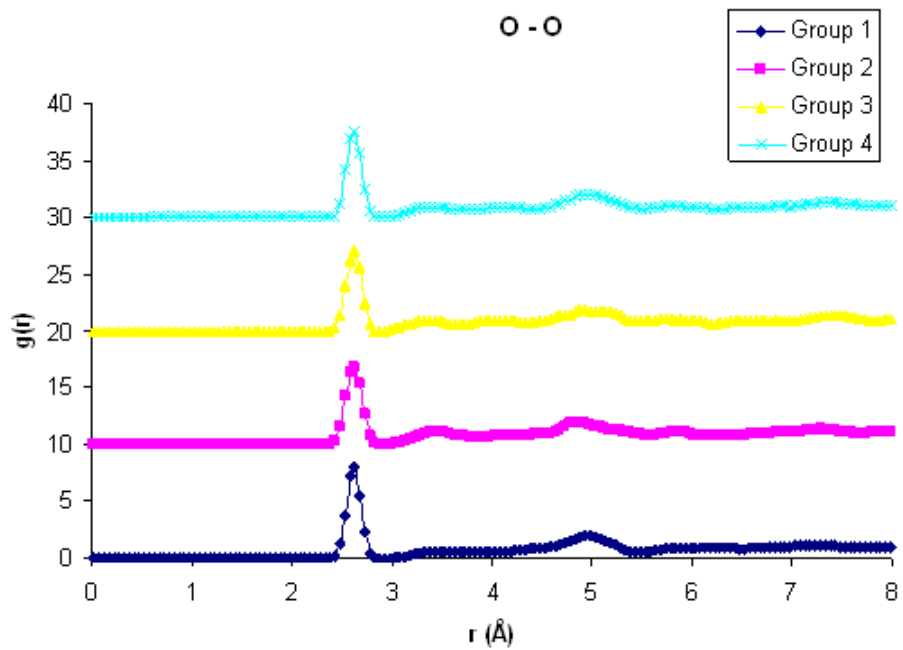


Figure 3.10: O-O PDF for the four final structures using BKS

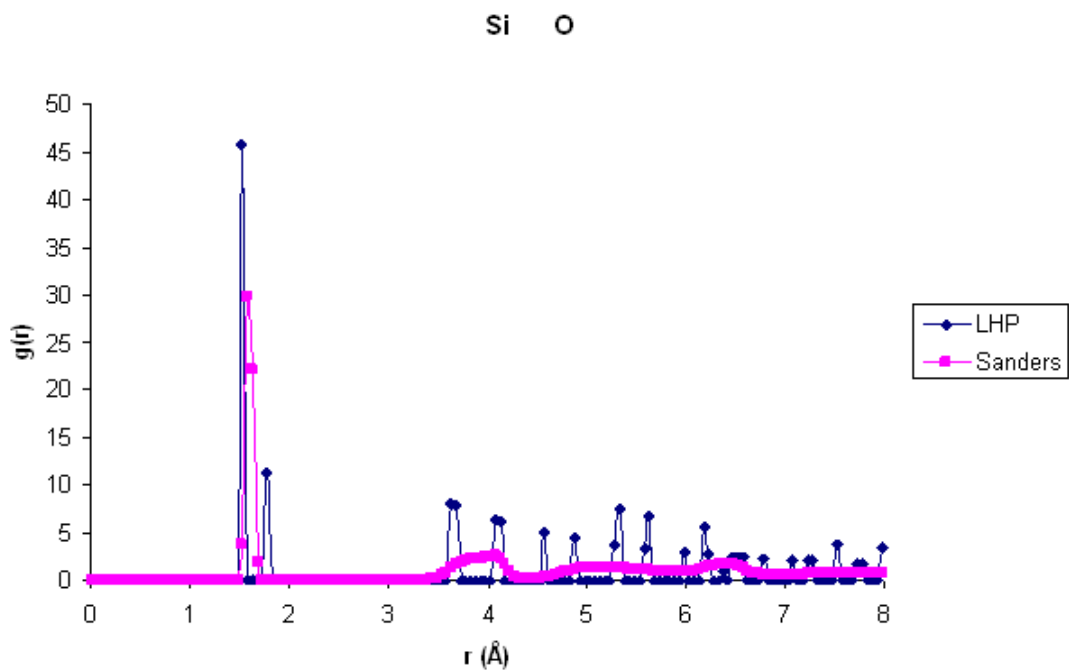


Figure 3.11: Comparison of the Si-O PDFs of the final structure using the Sanders potential and LHP Tridymite

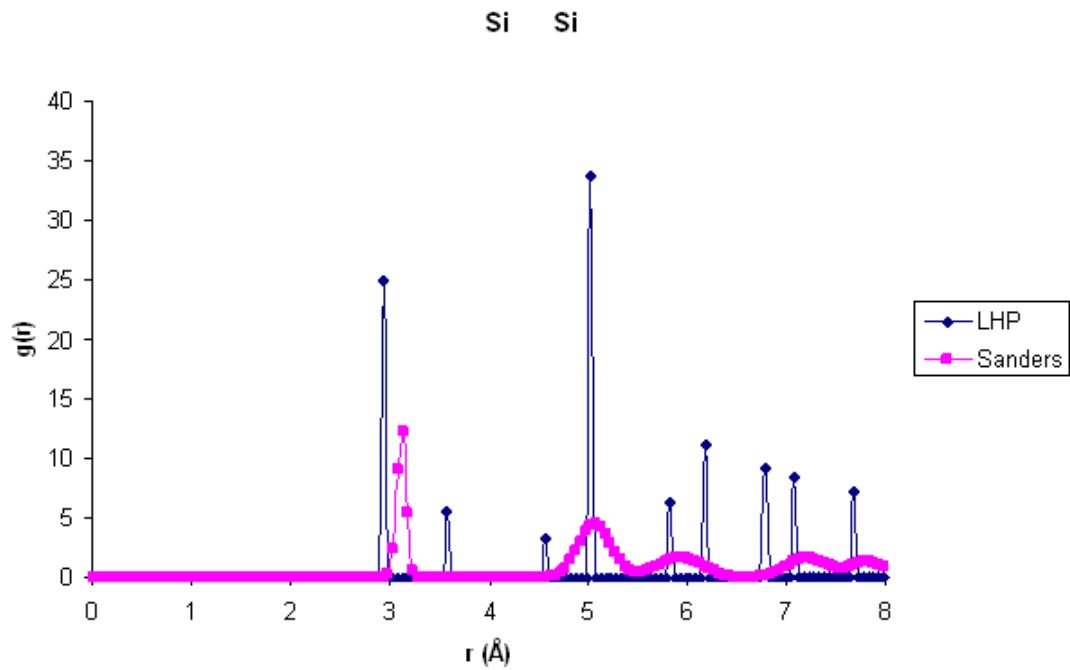


Figure 3.12: Comparison of the Si-Si PDFs of the final structure using the Sanders potential and LHP Tridymite

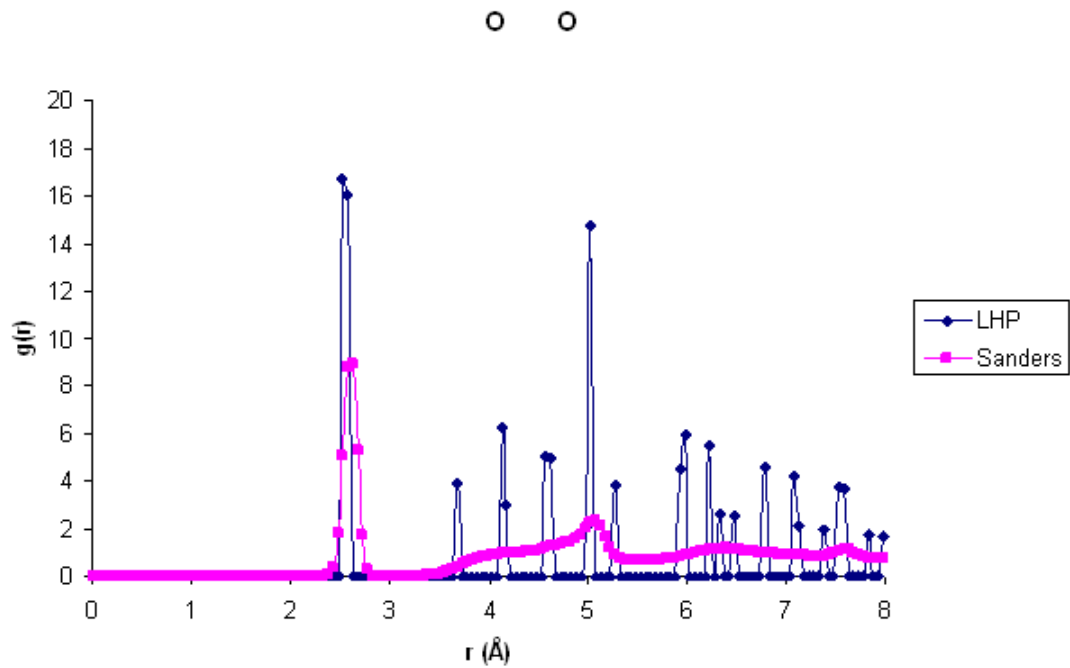


Figure 3.13: Comparison of the O-O PDFs of the final structure using the Sanders potential and LHP Tridymite

3.2.2.2.2 Bond lengths

Figure 3.14 shows Si-O bond length distributions for the four final BKS structures and the final Sanders structure. The frequency has been normalised because the structures have different numbers of atoms. Each point represents the frequency with which that bond length occurs divided by the total number of atoms in the structure.

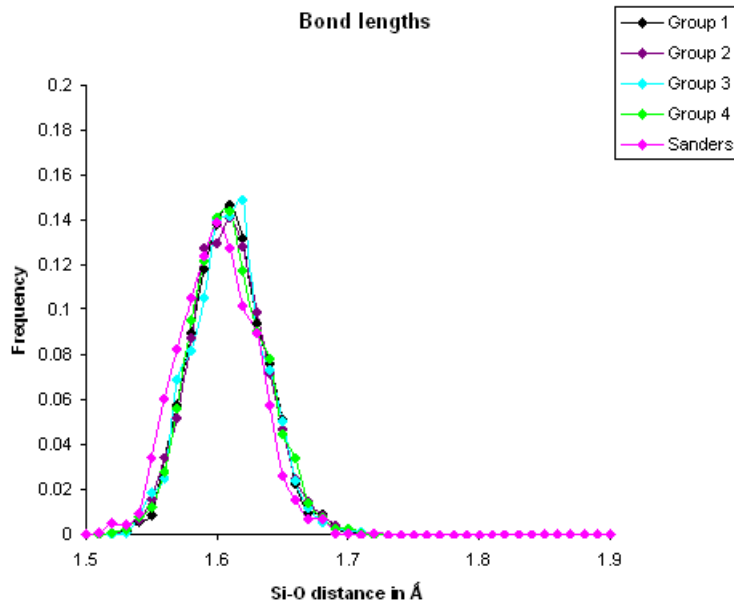


Figure 3.14: Si-O bond length distributions for the four final BKS structures and the final Sanders structure

There appears to be little difference between the different final structures. However, the plots differ greatly from all the crystal structures shown in Figure 1.10 (on page 24), with the exception of MX1 tridymite. All simulated structures and MX1 tridymite only have one peak, whereas all the remaining crystal structures have more

than one. The peaks for the simulated structures and MX1 tridymite are much wider and shorter than those for the crystal structures, indicating a higher level of disorder. The mean bond length for all simulated structures is 1.60 Å. This value is the same as for MX1 tridymite but is different from those for the other crystal structures.

3.2.2.2.3 O-Si-O angles

Figure 3.15 shows O-Si-O angle distributions for the four final BKS structures and the final Sanders structure.

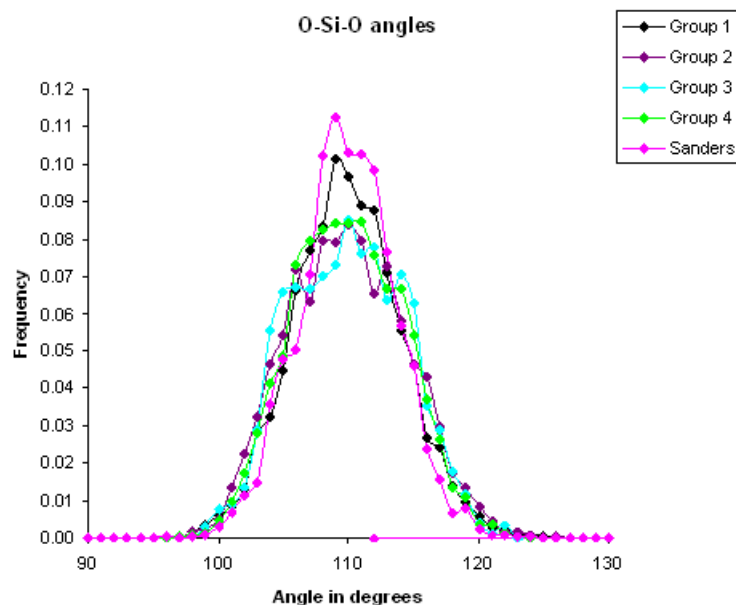


Figure 3.15: O-Si-O angles for the four final BKS structures and the final Sanders structure

As with bond lengths there does not appear to be a significant difference in O-Si-O angles between the final structures. The peaks are

much lower and broader than those for all the crystal structures (including MX1 tridymite) shown in Figure 1.11 on page 25. There is only one peak for each of the simulated structures. This is the case for four of the crystal structures. The remaining two (LHP and OC tridymite) have 2 peaks. In contrast to the calculated bond lengths, the mean of the O-Si-O angles for all simulated structures is similar to those for the crystal structures: between 109.42° and 109.43° for all simulated structures compared with 109.47° for all experimental crystal structures except for the LHP polymorph which is 108.37° .

3.2.2.2.4 Si-O-Si angles

Figure 3.16 shows Si-O-Si angle distributions for the four final BKS structures and the final Sanders structure.

In contrast to both bond lengths and O-Si-O angles, the Si-O-Si angles of the final simulated structures differ from one another, as might be expected.

Groups 1 and 2 for simulations using the BKS potential are similar to each other and display a very wide curve, much wider than for any of the experimental crystal structures, as shown in Figure 1.12 (on page 25). The mean angles are 150.7° and 148.8° for groups 1

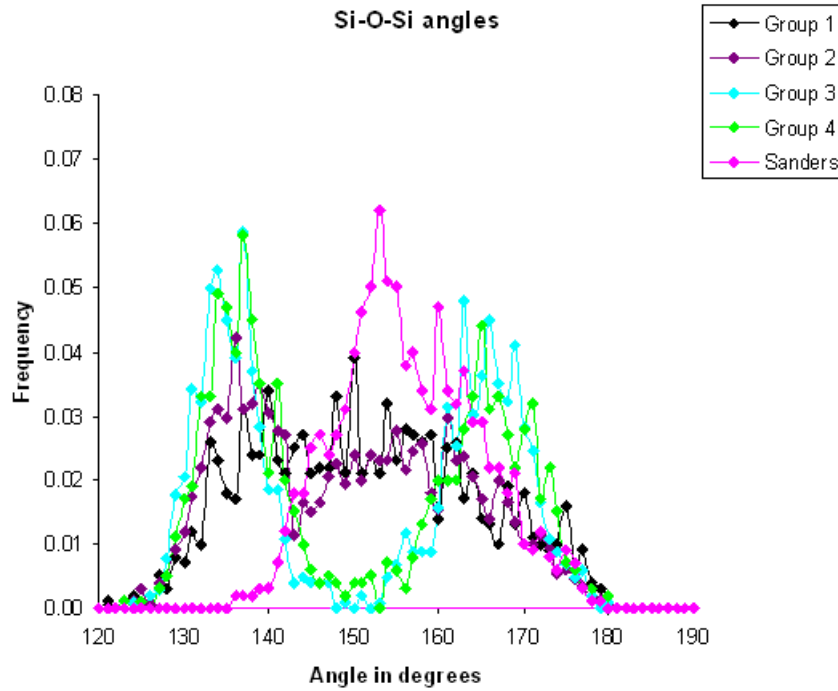


Figure 3.16: Si-O-Si angle distributions for the four final BKS structures and the final Sanders structure

and 2 respectively, which are similar to the mean of 149.7° for the crystal structure of the MX1 polymorph.

Plots for groups 3 and 4 are similar to each other and display 2 peaks. The locations of the peaks (at approximately 137° and 165°) are very different from those observed in any of the crystal structures.

The plots for the Sanders potential simulations have one peak with the highest point at 153° . The first of the 2 peaks in the equivalent graph for the LHP crystal structure (Figure 1.12, page 25) is quite close to this value at 152° . Although the Sanders potential

simulations do not have a second peak at 180° , the main peak is asymmetrical with a higher frequency of points to the right of the peak than to the left and the means of the Si-O-Si angles for Sanders simulations and LHP crystal structure are not too dissimilar at 156° and 158° respectively. It is therefore possible that the Sanders potential simulations are fluctuating about an average structure of the LHP polymorph.

When the atomic configurations are observed throughout a simulation using the BKS potential, the atoms vibrate around Si-O-Si angles which are significantly less than 180° . This observation does not confirm the postulation that the angles of the ideal structures described in section 1.12 are instantaneous values and that the atoms are actually vibrating around a mean value of 180° .

3.2.2.3 Alternative simulations

Several changes were made to the inputs to the simulations to test if there would be any affect on the resulting structures and their properties:

- 1) Simulations were run with the original cut-off of 8 \AA changed to 9 \AA , 10 \AA and 12 \AA .

- 2) The simulation time was doubled.
- 3) Simulations were run for non-ambient pressures.
- 4) The $N\sigma T$ ensemble was replaced with the NPT ensemble (described in section 2.2.6).
- 5) The time step for the BKS potential was changed from 1 fs to 0.2 fs and the time step for the Sanders potential was changed from 0.2 fs to 0.1 fs.
- 6) In the Sanders potential the shell with a mass of 0.05 a.m.u. was replaced with a massless shell (described in section 2.3.1.6).
- 7) Aluminium impurities were introduced: A number of simulations were run where between 1 and 21 silicon atoms were replaced with aluminium atoms. A sodium ion was added for each aluminium atom to ensure charge neutrality.
- 8) Simulations were run using single clusters of various sizes rather than using periodic boundary conditions. Hydrogen atoms were added to the surface of the cluster for charge neutrality. Parameters for O-H interactions were obtained from [71].

These changes did not appear to make a discernible difference (as determined by bond lengths and angles) to the resulting structures.

3.3 Simulations involving two potentials

In order to examine the extent to which the choice of potential determines the properties of the final structure of a simulation, the final structures of a number of simulations using the BKS potential were used as starting structures for simulations using the Sanders potential, and vice versa. Table 3.6 shows a sample of typical results of these calculations. The first column refers to the first potential used in the simulation. The second column refers to the potential which took as input the output of the simulation using the first potential. The fourth column contains the space group of the original crystal starting structure which was used as input to the first potential. The fifth column contains the resulting energy from the second simulation. The sixth column contains the resulting volume from the second simulation. Column seven contains the resulting energy from a simulation using only one potential given in column two and the crystal structure in column four as input. Column eight contains the resulting volume for the simulations described for the previous column.

First potential	Second potential	Temperature (K)	Space group of starting structure	Energy per Si atom of final structure (eV)	Volume per Si atom of final structure (\AA^3)	Energy of a simulation of just the second potential	Volume of a simulation of just the second potential
BKS	Sanders	273.15	LHP	-128.43	45.98	-128.43	45.96
BKS	Sanders	1600	LHP	-127.43	44.17	-127.58	43.62
BKS	Sanders	273.15	OP	-58.02	40.49	-58.05	39.59
BKS	Sanders	273.15	MX1	-128.43	45.85	-128.43	45.88
Sanders	BKS	1100	HP	-57.40	41.76	-57.40	41.71
Sanders	BKS	1100	LHP	-57.40	41.72	-57.38	42.98
Sanders	BKS	900	OC	-57.57	40.46	-57.54	41.57
Sanders	BKS	273.15	OP	-128.43	45.62	-128.43	45.67
Sanders	BKS	273.15	MX1	-58.05	39.59	-58.05	39.59

Table 3.6: Energies and volumes using MD for simulations using the BKS potential followed by the Sanders potential and vice versa

It can be seen that the energies and volumes resulting from simulations using two potentials are comparable with simulations using the second potential alone.

Additionally, the atomic configurations and PDFs of simulations with the Sanders potential as the second potential are similar to those using the Sanders potential alone, while the atomic configurations and PDFs of simulations with the BKS potential as the second potential fall into one of the four groups described in section 3.2.2.2.

These results are a strong indication that the most influential factor on the final atomic configurations, energies and volumes of a simulation are the choice of potential.

3.4 Simulations involving two methods

Simulations were carried out where the output of a free energy calculation was used as the input to an MD simulation using the BKS potential, and vice versa.

Tables 3.7 and 3.8 contain results for MD simulations as the first method and free energy minimisation as the second method for energy and volume respectively. Tables 3.9 and 3.10 contain results

for free energy minimisation as the first method and MD as the second method for energy and volume respectively. The first column of each table contains the starting structure and the number of silicon atoms in the structure used as the input for the first method. The second column shows the temperature of the first simulation. The third column shows the temperature of the second simulation. Column 4 shows the resulting energy/volume from the second simulation. Column 5 shows the energy/volume of a single simulation using free energy minimisation at the temperature in column 3. Column 6 shows the energy/volume of a single simulation using MD at the temperature in column 3. A simulation showing N/A did not successfully complete. The final column shows the final atomic configuration resulting from the second simulation. Numbers in that column refer to one of the four groups described in section 3.2.2.2 which are the outcomes of MD simulations using the BKS potential. NKS stands for “no known structure”.

With regard to atomic configuration, all but 5 out of the 36 simulations resulted in a structure with a configuration belonging to one of the four groups described in section 3.2.2.2 which are the outcomes of MD simulations using the BKS potential alone. This was regardless of whether MD was the first or second method. An explanation

Starting Structure	Temperature (K)	Temperature (K)	Energy per Si atom (eV) after 2nd method	Energy of free energy alone	Energy of molecular dynamics alone	Appearance
HP 32	1	1	-57.88	-57.78	-58.22	2 or 3
HP 32	1	273.15	-57.92	-57.80	-57.94	2 or 3
HP 32	1	700	-58.14	-58.01	-57.89	1
LHP 32	273.15	1	-57.88	-57.83	N/A	2 or 3
LHP 32	273.15	273.15	-57.94	-57.96	N/A	2 or 3
LHP 32	273.15	700	-58.18	-58.08	-57.89	2 or 3
LHP 32	700	1	-57.88	-57.83	N/A	2 or 3
LHP 32	700	273.15	-57.92	-57.96	N/A	2 or 3
LHP 32	700	700	-58.18	-58.08	-57.89	2 or 3
MC 32	273.15	1	-57.88	-57.83	-58.23	2 or 3
MC 32	273.15	273.15	-57.92	-57.82	-58.13	2 or 3
MC 32	273.15	700	-58.18	-58.08	-57.89	2 or 3
MX1 64	1	1	-57.87	-57.88	-58.23	OC
MX1 64	1	273.15	-57.84	-57.87	-58.11	NKS
MX1 64	1	700	-58.14	-58.10	-57.82	Almost OC

Table 3.7: Energies and configurations using the output of an MD simulation as input to a free energy minimisation calculation using the BKS potential

for this might be that in MD simulations a larger proportion of the energy landscape can be explored than in free energy minimisation. Therefore, in MD there is a higher probability that an atomic configuration with a lower energy or corresponding to a section of the energy landscape surrounded by high energy barriers will be found. The method of free energy minimisation may not explore enough of the energy landscape to find an atomic configuration which has a significantly lower energy than for MD or (if it is the second method) may be unable to overcome the large energy barriers of the atomic configuration found by MD.

Starting Structure	Temperature (K)	Temperature (K)	Volume per Si atom (eV) after 2nd method	Volume of free energy alone	Volume of molecular dynamics alone	Appearance
HP 32	1	1	40.05	50.89	39.78	2 or 3
HP 32	1	273.15	40.20	49.95	40.34	2 or 3
HP 32	1	700	43.09	49.54	38.15	1
LHP 32	273.15	1	40.05	44.19	N/A	2 or 3
LHP 32	273.15	273.15	40.21	49.37	N/A	2 or 3
LHP 32	273.15	700	40.67	49.70	38.17	2 or 3
LHP 32	700	1	40.05	44.19	N/A	2 or 3
LHP 32	700	273.15	40.21	49.37	N/A	2 or 3
LHP 32	700	700	40.67	49.70	38.17	2 or 3
MC 32	273.15	1	40.05	44.25	42.24	2 or 3
MC 32	273.15	273.15	40.20	42.19	37.88	2 or 3
MC 32	273.15	700	40.70	44.02	38.33	2 or 3
MX1 64	1	1	44.47	40.05	41.32	OC
MX1 64	1	273.15	42.74	44.48	37.72	NKS
MX1 64	1	700	44.99	43.76	38.18	Almost OC

Table 3.8: Volumes and configurations using the output of an MD simulation as input to a free energy minimisation calculation using the BKS potential

All the energies of the MD followed by free energy minimisation calculations are similar to those of free energy minimisation alone. The majority of the energies of the free energy minimisation followed by MD calculations are similar to those of MD alone. This is not in accord with the discussion in the previous paragraph that MD is more likely to find a more stable structure. However, overall, the differences in energy between all structures and methods are very small.

The correlation described above for energies is not observed for vol-

Starting Structure	Temperature (K)	Temperature (K)	Energy per Si atom (eV) after 2nd method	Energy of free energy alone	Energy of molecular dynamics alone	Appearance
HP 108	1	1	-58.21	-57.78	-58.24	4
HP 108	1	273.15	-58.04	-57.82	-57.94	4
HP 108	1	700	-57.75	-58.01	-57.59	4
HP 108	273.15	1	-58.21	-57.78	-58.24	4
HP 108	273.15	273.15	-58.04	-57.82	-57.94	4
HP 108	273.15	700	-57.74	-58.01	-57.59	4
HP 108	700	1	-58.24	-57.78	-58.24	4
HP 108	700	273.15	-58.04	-57.82	-57.94	4
HP 108	700	700	-57.75	-58.01	-57.59	4
LHP 108	1	1	-58.21	-57.78	-58.22	OC
LHP 108	1	273.15	-58.04	-57.82	-58.04	4
LHP 108	1	700	-57.74	-57.82	-57.74	4
LHP 108	700	1	-58.23	-57.78	-58.22	4
LHP 108	700	273.15	-58.04	-57.82	-58.04	4
LHP 108	700	700	-57.75	-57.82	-57.75	4
MC 32	273.15	1	N/A	-57.83	-58.23	N/A
MC 32	273.15	273.15	-57.13	-57.82	-58.13	2 or 3
MC 32	273.15	700	-57.89	-58.08	-57.89	2 or 3
MX1 64	1	1	-58.31	-57.88	-58.23	2 or 3
MX1 64	1	273.15	-58.11	-57.87	-58.11	OC
MX1 64	1	700	-57.83	-58.10	-57.82	2 or 3

Table 3.9: Energies and configurations using the output of a free energy minimisation calculation as input to an MD simulation using the BKS potential

umes: For MD followed by free energy calculations, all the volumes differ significantly from free energy alone and all but one differ from MD alone. For free energy followed by MD all volumes differ significantly from free energy alone, however, 16 out of 20 simulations are similar to MD alone. This result accords with the postulation that MD explores a larger proportion of the energy landscape and finds a more stable structure.

Starting Structure	Temperature (K)	Temperature (K)	Volume per Si atom (eV) after 2nd method	Volume of free energy alone	Volume of molecular dynamics alone	Appearance
HP 108	1	1	42.06	50.88	40.09	4
HP 108	1	273.15	40.51	50.41	40.34	4
HP 108	1	700	41.27	50.03	41.67	4
HP 108	273.15	1	42.06	50.88	40.09	4
HP 108	273.15	273.15	40.51	50.41	40.34	4
HP 108	273.15	700	41.33	50.03	41.67	4
HP 108	700	1	40.08	50.88	40.09	4
HP 108	700	273.15	40.50	50.41	40.34	4
HP 108	700	700	41.30	50.03	41.67	4
LHP 108	1	1	43.20	50.84	40.76	OC
LHP 108	1	273.15	40.52	43.46	40.56	4
LHP 108	1	700	41.29	50.39	41.36	4
LHP 108	700	1	40.43	50.84	40.76	4
LHP 108	700	273.15	40.52	43.46	40.56	4
LHP 108	700	700	41.30	50.39	41.36	4
MC 32	273.15	1	N/A	44.25	42.24	N/A
MC 32	273.15	273.15	37.89	42.19	37.88	2 or 3
MC 32	273.15	700	38.36	44.02	38.33	2 or 3
MX1 64	1	1	37.34	40.05	41.32	2 or 3
MX1 64	1	273.15	37.72	44.48	37.72	OC
MX1 64	1	700	38.20	43.76	38.18	2 or 3

Table 3.10: Volumes and configurations using the output of a free energy minimisation calculation as input to an MD simulation using the BKS potential

With a few exceptions the temperature of the first simulation does not appear to greatly affect the outcome of the second simulation. Table 3.11 shows energies and volumes using HP tridymite as the starting structure for free energy minimisation, followed by the use of the output as input to MD simulations, sorted by the temperature of the second method. We note that the resulting energies and volumes where the temperature of the second simulation is the same,

are similar for all simulations, the exception being a simulation at 700 K followed by one at 1 K.

Temperature of first simulation	Temperature of second simulation	Energy per Si atom (eV)	Volume per Si atom (\AA^3)
1	1	-58.21	42.06
273.15	1	-58.21	42.06
700	1	-58.24	40.08
1	273.15	-58.04	40.51
273.15	273.15	-58.04	40.51
700	273.15	-58.04	40.50
1	700	-57.75	41.27
273.15	700	-57.74	41.33
700	700	-57.75	41.30

Table 3.11: Energies and volumes using the output of a free energy minimisation calculation as input to an MD for simulations using the BKS potential for HP tridymite

3.5 Density Functional Theory

Density Functional Theory (DFT) calculations (methodology described in section 2.4) were performed for the polymorphs described in the previous sections. This was to investigate whether any final structures different from those from free energy minimisation and MD could be reproduced.

Calculations using periodic boundary conditions did not converge. For simulations using finite clusters only three of the six starting structures converged.

All three calculations resulted in a similar looking structure, shown in Figure 3.17.

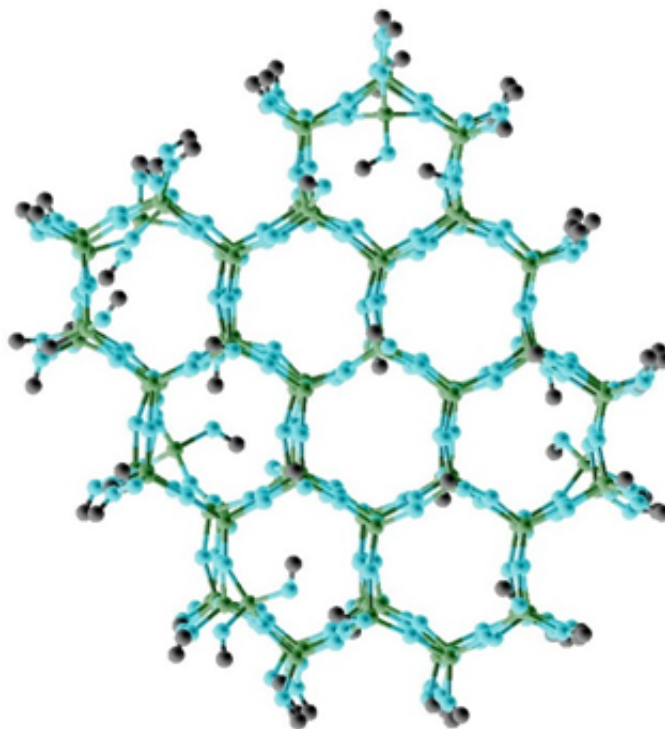


Figure 3.17: Final structure using Density Functional Theory

The structure appears to be part way between HP and LHP tridymite. The Si-O-Si angle varies but is mostly in the range 150° - 170° . For the ideal HP structure it is 180° and for the LHP structure it is 151.2° .

There was more variation in the resulting energies between structures than for the free energy minimisation and MD. This is, however, attributed to the fact that the values were less reliable for

the Density Functional Theory calculations than for the other two methods because clusters rather than periodic boundary conditions were used. The clusters were made by adding hydrogen atoms to the surface of the structures to ensure they were charge neutral. The original cells of the structures were different shapes and sizes and so it was difficult to construct clusters which were perfectly comparable.

3.6 Discussion and conclusions

3.6.1 Energy and volume

The main finding with respect to the resulting energies of final structures from the simulations is that they are not dependent on the starting structure, but that the atomic potential and simulation technique used were the main factors affecting the final energies. For most MD simulations for both the BKS and Sanders potentials the energy of a structure increased (became less negative) with increasing temperature, although there were several exceptions. This trend was not seen in free energy minimisation calculations. A possible reason for this result is that the ZSISA (Zero Static Internal

Stress Approximation) [42] which is generally used in free energy minimisation calculations for silicates, minimises unit cell shape and size with respect to free energy, but the atomic coordinates within the cell are only minimised with respect to internal energy. This approximation means that there is no temperature term in the minimisation of atomic coordinates.

The main finding with respect to the resulting volumes of final structures was that they are not dependent on the temperature of the simulation. They are very weakly dependent on the starting structure in free energy minimisation calculations. As with values for energy, the atomic potential and simulation technique used were the main factors affecting the final volumes. The Sanders potential reproduced experimental volumes more accurately than the BKS potential.

3.6.2 Final atomic configuration

In general, the atomic configuration of the final structure did not appear to be strongly determined by the temperature of the simulation. In free energy calculations the final structure was weakly correlated with the starting structure, but this was not the case

for MD simulations or electronic structure calculations. As with energy and volume, the atomic potential and simulation technique used were the main factors affecting the configuration of the final structure. The atomic configurations resulting from MD simulations using the BKS potential are unlike any structures documented in the literature. However, all MD simulations using the Sanders potential resulted in one structure, in which atoms are most probably vibrating around the ideal LHP structure.

These results differ from what might be expected experimentally. A number of experimental studies have been carried out which have concluded that different tridymite structures are the most stable at different temperature ranges (these temperature ranges are given in section 1.2), resulting in a phase diagram [8]. A range of temperatures was used in the simulations described in the present work. Therefore, according to the experimental phase diagram, a range of tridymite structures determined by simulation temperature would have been expected.

3.6.3 Conclusions

There are a number of possible explanations for the results described above:

1) The transitions between the various tridymite polymorphs require no bonds to be broken or formed. The most significant changes are in the Si-O-Si angles. The energy landscape is therefore quite flat, i.e. the energy barriers between polymorphs are quite low and can be easily overcome. The techniques used above may not be sensitive enough to deal with such low energy barriers. The fact that there is little variation in energies between the simulated structures supports this hypothesis.

2) The parameters for the two potentials used are derived from ab initio calculations and experimental data for quartz. The potentials are able to successfully reproduce the properties of a number of low pressure polymorphs. The transitions between these structures are reconstructive, where bonds are broken and formed, as opposed to displacive, where only angles between atoms change. It may not be possible to extrapolate these potentials to differentiate between structures which undergo displacive transitions, as is the case for the tridymite polymorphs.

3) Many of the starting structures used in this work have been obtained from samples which have been found in nature. It is possible that some of these structures are meta-stable and are at local minima in the energy landscape, i.e. there is no point on the silica phase

diagram where they are the most energetically favourable structure. The resulting structures from the computer simulations may be different from the crystal structures because they have found different local minima or have found the global minimum. It is unlikely, however, that the simulations have found the true global minimum, because all of the final structures from MD simulations and some of the final structures from free energy calculations do not resemble any of the tridymite crystal structures.

Chapter 4

The static and dynamic properties of silica melts and glasses

This chapter describes computational simulations using molecular dynamics (MD) to explore the structural and dynamic properties of amorphous silica, both of a melt and a glass, at a range of temperatures. As discussed in section 1.4, computational techniques are especially useful for exploring the properties of amorphous materials, as there are certain properties of these materials which it is not possible to precisely determine using experimental techniques.

The aims of this chapter are described in section 1.4 on page 39, numbered 1 to 6.

Section 4.1 of this chapter describes the modifications required to the BKS potential to enable it to simulate a melt. Section 4.2 discusses the simulations to produce a vitreous structure. Section 4.8 investigates aim 1. Section 4.9 describes research into aim 2. Sections 4.3 to 4.9 cover aims 3 to 5. Each section describes investigations into a certain property or group of properties. Section 4.10 covers aim 6 and discusses the attempts to simulate a melt using the Sanders potential (section 2.3.3) and the properties of the resulting structure.

All simulations discussed in this chapter were carried out at ambient pressure. Chapter 5 describes calculations at elevated pressures.

4.1 Modification of the BKS potential

At increasingly small interatomic distances the BKS potential diverges to infinitely low energies. This behaviour is shown in Figure 4.1, where interatomic distance is on the x-axis and energy is on the y-axis.

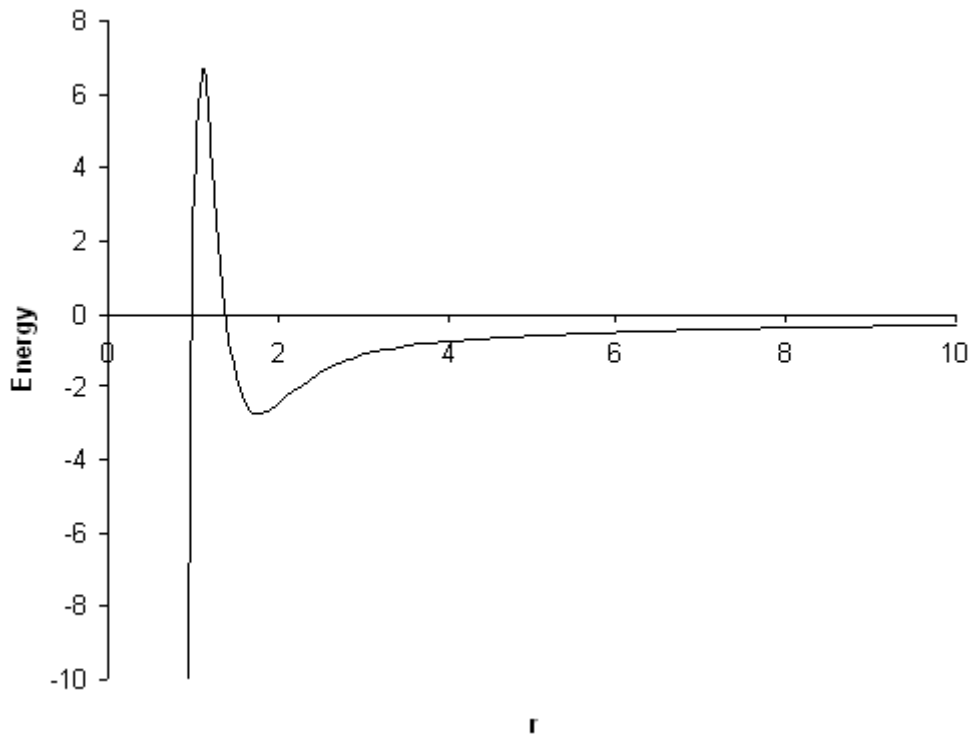


Figure 4.1: The divergence in energy of the BKS potential at small interatomic distances

This does not present a problem when modelling materials at low temperatures because the bonds between the atoms are strong and the atoms are subjected to small forces. They are therefore not able to access the small interatomic distances at which energy divergence becomes a problem. In a melt, however, atoms may move with a larger force and may therefore overcome the energy barrier at which the divergence to infinitely low energies occurs.

When simulating structures at high temperatures, a correction must be made to the formula for the potential so that it corresponds more

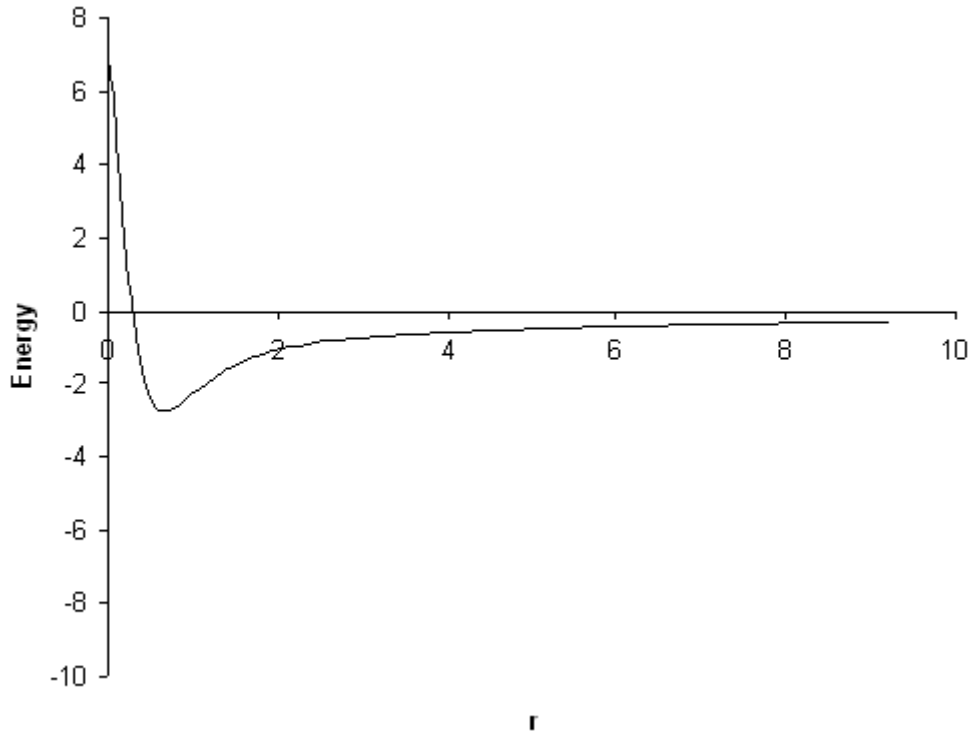


Figure 4.2: Schematic interatomic potential

closely to the behaviour shown in Figure 4.2, where the energy becomes infinitely positive at increasingly small interatomic distances. A number of possible methods for making this correction were tried in this thesis:

A squared or cubed term (or both) can be added in order to make the repulsive force stronger, as shown in Equation 4.1 (the original BKS formula and parameters are given in [24] and section 2.3.2 and include only the first three terms).

$$\Theta_{ij}(r_{ij}) = \frac{Q_i Q_j}{r_{ij}} - \frac{C_{ij}}{r_{ij}^6} + A_{ij} e^{-B_{ij} r_{ij}} + D_{ij} e^{-E_{ij} r_{ij}^2} + F_{ij} e^{-G_{ij} r_{ij}^3} \quad (4.1)$$

Several different values for the coefficients of the squared and cubed terms were tried. However, this did not make the potential sufficiently repulsive at small interatomic distances.

A second possible method is the addition of a harmonic term, as shown in Equation 4.2.

$$\Theta_{ij}(r_{ij}) = \frac{Q_i Q_j}{r_{ij}} - \frac{C_{ij}}{r_{ij}^6} + A_{ij} e^{-B_{ij} r_{ij}} + k_{ij} (r_{ij} - D_{ij})^2 + E_{ij} \quad (4.2)$$

Several different values for the constants were tried. However, values which were large enough to ensure that the potential was sufficiently repulsive at small interatomic distances significantly affected the behaviour of the potential at larger distances.

Another possible method is the addition of a Lennard-Jones term as is shown in Equation 4.3.

$$\Theta_{ij}(r_{ij}) = \frac{Q_i Q_j}{r_{ij}} - \frac{C_{ij}}{r_{ij}^6} + A_{ij} e^{-B_{ij} r_{ij}} + 4\epsilon_{\mu\nu} \left(\left(\frac{\sigma_{\mu\nu}}{r_{ij}} \right)^{30} - \left(\frac{\sigma_{\mu\nu}}{r_{ij}} \right)^6 \right) \quad (4.3)$$

The values for the additional parameters are taken from [72], where $\epsilon_{Si-O} = 4.963460$, $\epsilon_{O-O} = 1.6839685$, $\sigma_{Si-O} = 0.1313635$ and $\sigma_{Si-O} = 0.1779239$.

When this method was tested on a melt it succeeded in ensuring that interatomic distances did not become unfeasibly small. The amended potential was tested on crystal structures at temperatures below the melting point. The energy and volume of these structures were compared with those of the structures using the original potential and it was found that their values did not differ significantly.

This method has been used in a number of published papers describing simulations of a silica melt, including [73], [61], and [74], which explore diffusion coefficients and density anomalies in liquid silica. Since it has a published track record of successfully simulating a melt and the tests described above were successful, this method was chosen as the one to be used for simulations in this thesis.

In order to implement the addition of the Lennard-Jones term, the formula for the potential in the DL_POLY Fortran code was modified. The specific code is located in the “vdw_module.f” file at line 376. This file is located in the “srcmod” directory of the DL_POLY code.

4.2 Production of quenched structure

With current computational speeds it is unfeasible to quench a melt at the rate used in experiments and so in practice quench rates using computational techniques are several orders of magnitude faster than under experimental conditions. To produce vitreous structures for simulations using the BKS potential, a simulation was run for 100 ps, the temperature was reduced by 500 K and run for another 100 ps. This was repeated until a temperature of 500 K was reached. The final reduction in temperature was 499 K with the final temperature being 1 K. 100 ps was a sufficient amount of time to settle energy fluctuations, giving a quench rate of 5×10^{12} K/s. K. Vollmayr, W. Kob and K. Binder [75] describe investigations into different cooling rates of simulated silica and this rate is in the range of quench rates recommended in the paper.

Six of the melts from crystal structures were successfully quenched. Four of these were from a temperature of 6000 K. Two (cristobalite and fluorite) were from a temperature of 5000 K because simulations of melts for these crystal structures at 6000 K did not complete successfully.

4.3 Diffusion

There is only a small amount of experimental data available on diffusion coefficients of a silica melt (for an explanation of diffusion coefficients see section 2.5.3). All experiments have been carried out in the range 1000 K - 1500 K ([76], [77] and [78]) which is below the silica melting point of 1986 K [79]. The resulting diffusion coefficients are in the range 10^{-11} m²/s - 10^{-14} m²/s.

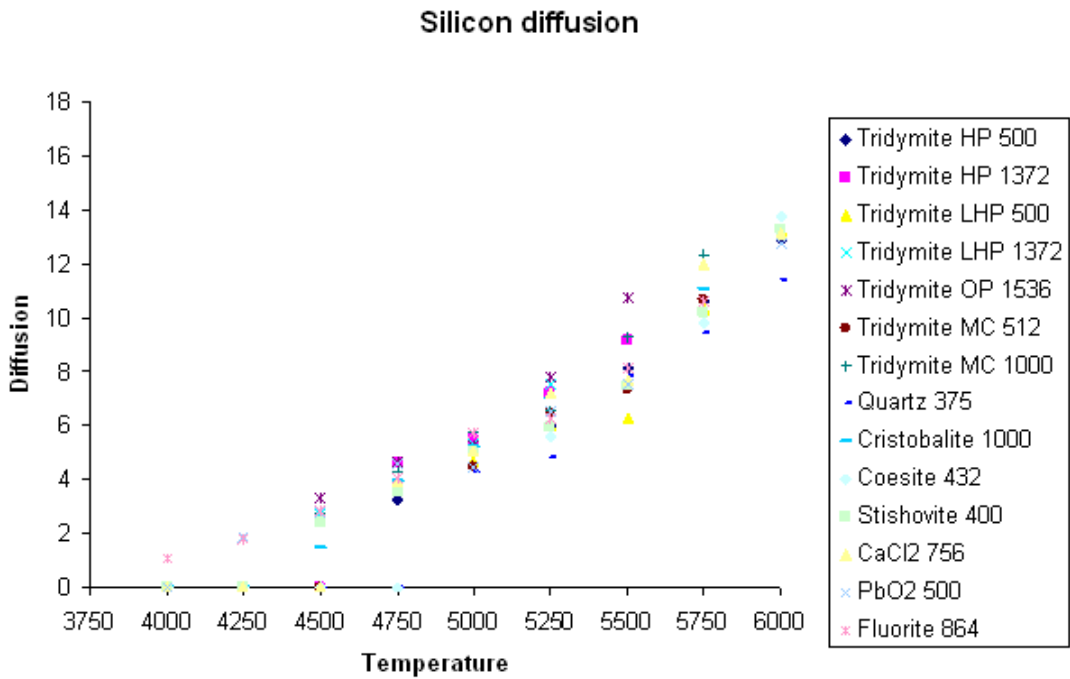


Figure 4.3: Diffusion coefficients (in units of 10^{-9} m²/s) for silicon for a number of silica crystal structures at a range of temperatures

Figures 4.3 and 4.4 show the diffusion coefficients (in units of 10^{-9} m²/s) of simulations starting with different crystal structures for silicon

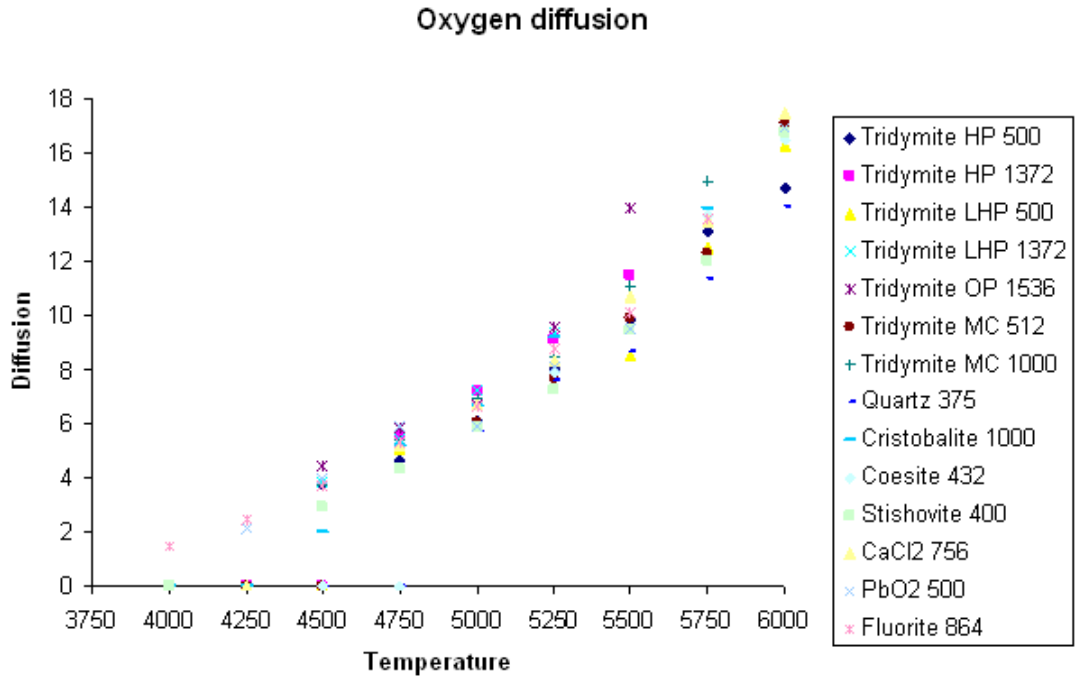


Figure 4.4: Diffusion coefficients (in units of 10^{-9} m²/s) for oxygen for a number of silica crystal structures at a range of temperatures

and oxygen respectively. The coefficients were calculated for the production period of 100,000 time steps, which is 50 ps. Simulations were carried out at a range of temperatures. The number after the name of the crystal structure refers to the number of silicon atoms in the structure. 17 out of a total of 63 simulations did not successfully complete and are not shown in the figures.

The values in the figures are comparable to the results of simulations using the BKS potential carried out by Y. Zhang, G. Guo, K. Refson and Y. Zhao [74] in which diffusion coefficients for simulations at 6543 K (in units of 10^{-9} m²) ranged from 11.0 to 16.8 for silicon and

15.2 to 21.0 for oxygen. Simulations at 3310 K resulted in diffusion coefficients in the range 0.027 to 0.044 for silicon and 0.048 to 0.74 for oxygen. The simulations described in the paper differ from those in this work in that they were performed in the less experimentally realistic NVE (constant volume and constant energy) ensemble, in contrast to the $N\sigma T$ ensemble used in this thesis.

For information Figure 4.5 shows a typical Mean Square Displacement of a melted structure from this thesis (for an explanation of Mean Square Displacement see section 2.5.2).

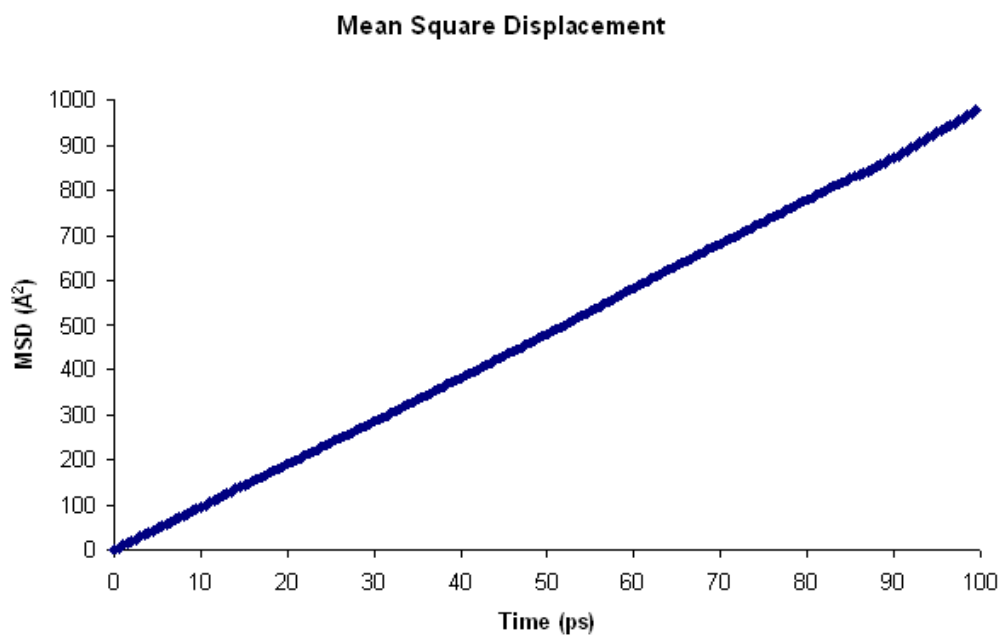


Figure 4.5: A typical Mean Square Displacement plot

There does not appear to be a large variation in diffusion coefficients between the different crystal starting structures at higher temper-

atures. At lower temperatures different structures appear to have slightly different melting points.

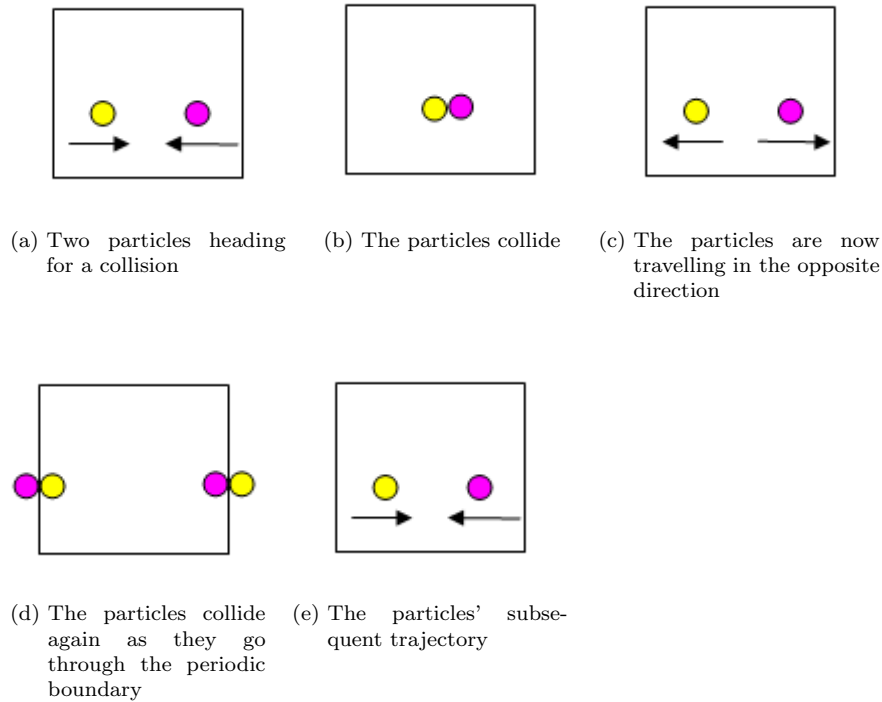


Figure 4.6: Example of how a system with a small number of atoms can have a lower diffusion coefficient than a larger system

As would be expected, the diffusion coefficients increase with increasing temperature. However, in simulations described in [74] at two different temperatures with four different system sizes it was found that diffusion coefficients increase with increasing system size. This is due to conservation of momentum and is illustrated in Figure 4.6. If two particles are travelling directly towards each other and collide, the direction of travel of each of them will be altered

so that they are travelling in opposite directions. In a system with a small number of atoms the particles are more likely to meet each other again when they leave the boundaries of the simulation box on one side and enter it on the other side. This causes them to change direction again. In a system with a larger number of atoms the two atoms are more likely to be shielded from each other and from this second collision by other atoms.

Starting structure	No. of Si atoms	Diffusion coefficient ($10^{-9}m^2$ per second) at temperature								
		4000	4250	4500	4750	5000	5250	5500	5750	6000
HP tridymite	500	0.000	0.015	2.755	3.269	5.618	6.025	8.146	10.611	12.881
HP tridymite	1372	0.000	0.002	0.000	4.628	5.477	7.177	9.507	N/A	N/A
LHP tridymite	500	0.000	0.001	0.005	3.787	4.691	6.009	6.291	10.36	13.248
LHP tridymite	1372	0.000	0.004	2.733	4.079	5.314	7.508	N/A	N/A	N/A
MC tridymite	512	0.000	0.000	0.005	N/A	4.442	6.483	7.301	10.634	13.122
MC tridymite	1000	0.000	0.004	2.736	4.289	5.764	6.508	9.282	12.320	N/A

Table 4.1: Diffusion coefficients of silicon for structures of different sizes

Starting structure	No. of Si atoms	Diffusion coefficient ($10^{-9}m^2$ per second) at temperature								
		4000	4250	4500	4750	5000	5250	5500	5750	6000
HP tridymite	500	0.000	0.022	3.814	4.656	6.126	8.060	9.846	13.104	14.666
HP tridymite	1372	0.003	0.008	0.0165	5.527	7.202	9.131	11.501	N/A	N/A
LHP tridymite	500	0.005	0.000	0.015	5.070	5.963	7.750	8.525	12.512	16.245
LHP tridymite	1372	0.002	0.010	3.868	5.474	7.269	9.3595	N/A	N/A	N/A
MC tridymite	512	0.000	0.000	0.012	N/A	6.062	7.630	9.871	12.302	17.089
MC tridymite	1000	0.000	0.011	3.738	5.405	6.936	8.418	11.103	14.949	N/A

Table 4.2: Diffusion coefficients of oxygen for structures of different sizes

Tables 4.1 and 4.2 show diffusion coefficients at a range of temperatures for silicon and oxygen respectively. Simulations given the value N/A did not successfully complete. The increase in diffusion coefficient with increasing system size is generally observed in sim-

ulations in this thesis at temperatures above 4500 K. Simulations in the temperature range 4000 K - 4500 K do not exhibit this behaviour, which is attributed to the particles having low diffusion coefficients and so rarely moving through the boundaries of the simulation cell, therefore behaviour shown in 4.6 does not occur.

In order to provide further evidence that the structures have melted a frequency table was constructed showing the displacement of every silicon atom individually, comparing its location at the beginning and end of the simulation. Table 4.3 shows this for all silicon atoms for a melt at 6000 K with LHP tridymite as the starting structure. It can be seen that no atom is displaced by less than 10 \AA^2 from its original site, indicating that a significant number of the original bonds in the crystal have been broken. Similar frequency tables were constructed for each crystal starting structure and similar results were obtained.

4.4 Arrhenius plots and activation energies

There have been a number of experimental studies to measure the activation energies of silicon and oxygen in silica (for an explanation of Arrhenius plots and activation energies see section 2.5.5). All

Distance in Å ²	Number of atoms at that distance
0-10	0
10-20	1
20-30	5
30-40	6
40-50	2
50-100	11
100-300	72
300-500	91
500-700	81
700-900	55
900-1100	36
1100-1300	41
1300-1500	24
1500-1700	22
1700-1900	11
>1900	42
Total	500

Table 4.3: Displacement of each silicon atom for a melt of LHP tridymite at 6000 K over 100 ps

the studies of which we are aware were carried out below the silica melting point of 1713°C [79]. Only one experiment investigating the activation energy of silicon could be found which was carried out by O. Jaoul, F. Bejina and F. Elie [77] and used Rutherford backscattering spectrometry resulting in an activation energy for silicon of 7.6 eV. Data obtained by J. C. Mikkelsen Jr. [80] using secondary ion mass spectrometry in the temperature range 1200°C-1400°C finds the activation energy of oxygen to be 4.7 eV. Experiments carried out by E. L. Williams [78] using heterogeneous isotope exchange in the temperature range 850°C-1250°C resulted in an activation energy for oxygen of 1.26 eV. E. W. Sucov [81] describes experi-

ments using the same method with an activation energy for oxygen of 1.3 eV. K. Muehlenbachs and H. A. Schaeffer [82] also used isotope exchange but in the temperature range 1150°C-1430°C and found an activation energy of 0.87 eV. All activation energies for oxygen except for one are much less than the strength of the Si-O bond (4.82 eV according to H. A. Schaeffer [83] and 3.8 eV according to J. C. Mikkelsen Jr. [80]), suggesting that the diffusion process consists of exchange of network oxygen [83].

Table 4.4 shows activation energies calculated from diffusion coefficients given in the previous section and R^2 values for the fit of the Arrhenius plots (the extent to which the activation energies lie on a straight line, with a value of 1 representing a perfect straight line and 0 representing a random distribution). This was only done for starting structures which yielded at least five successfully completed simulations with non-zero diffusion coefficients in the range 4000-6000 K. As can be seen in Figures 4.3 and 4.4 on pages 128 and 129, a couple of the starting structures have different melting points. The first point on the Arrhenius plots was therefore taken as the first non-zero diffusion coefficient. The temperature of this first point is given in column two of table 4.4. The temperature of the final point is given in column three. Simulations were carried

out at intervals of 250 K.

Starting structure and no. of Si atoms	First temp- -erature (K)	Second temp- -erature (K)	Silicon		Oxygen	
			R ²	Activation energy	R ²	Activation energy
Tridymite HP 500	4500	6000	0.99	2.494	0.99	2.191
Tridymite LHP 500	4750	6000	0.94	2.412	0.96	2.263
Tridymite MC 512	5000	6000	0.98	2.751	0.98	1.951
Tridymite MC 1000	4500	5750	0.98	2.732	0.99	2.365
Tridymite OP 1536	4500	5500	0.97	2.434	0.99	2.626
Quartz 375	5000	6000	0.96	2.732	0.99	2.270
Stishovite 400	4500	6000	0.99	2.566	0.99	2.349
PbO ₂ 500	4250	5500	0.96	2.448	0.94	2.249
CaCl ₂ 756	4750	6000	0.97	2.448	0.99	2.373
Fluorite 864	4000	5750	0.99	2.524	0.99	2.524

Table 4.4: Activation energies and R² values of fits of Arrhenius plots

Figures 4.7 to 4.10 contain examples of Arrhenius plots from calculations in the above table. Figures 4.7 and 4.9 show the best and worst fits respectively for silicon and Figures 4.8 and 4.10 show the best and worst fits respectively for oxygen.

The high R² values in table 4.4 for all starting structures confirm that silica is a strong glass former (see section 2.5.5 for an explanation of why this is so) and that this property is not affected by the starting structure. There is little variation in activation energy between the different starting structures, indicating that they exhibit similar melting behaviour at sufficiently high temperatures.

The calculated activation energies (which are above the melting point) for oxygen are approximately in the range of the values found

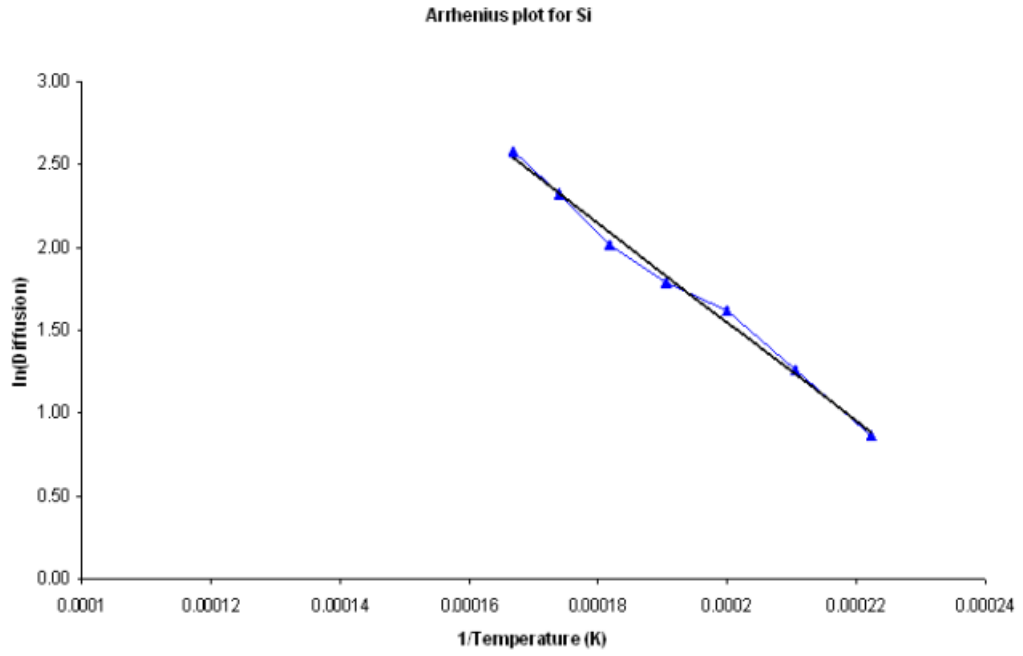


Figure 4.7: Arrhenius plot for silicon with stishovite as the starting structure (the highest R^2 of all the starting structures for silicon)

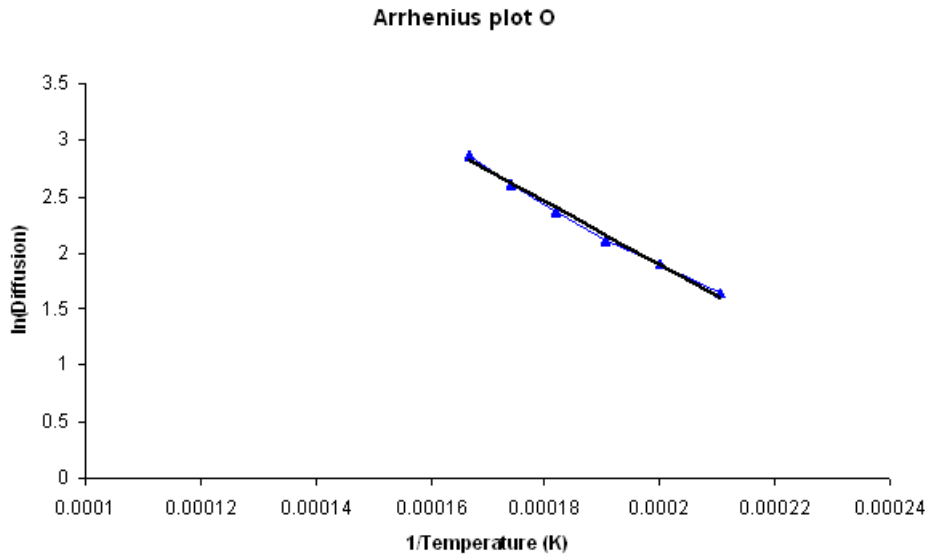


Figure 4.8: Arrhenius plot for oxygen with CaCl_2 as the starting structure (the highest R^2 of all the starting structures for oxygen)

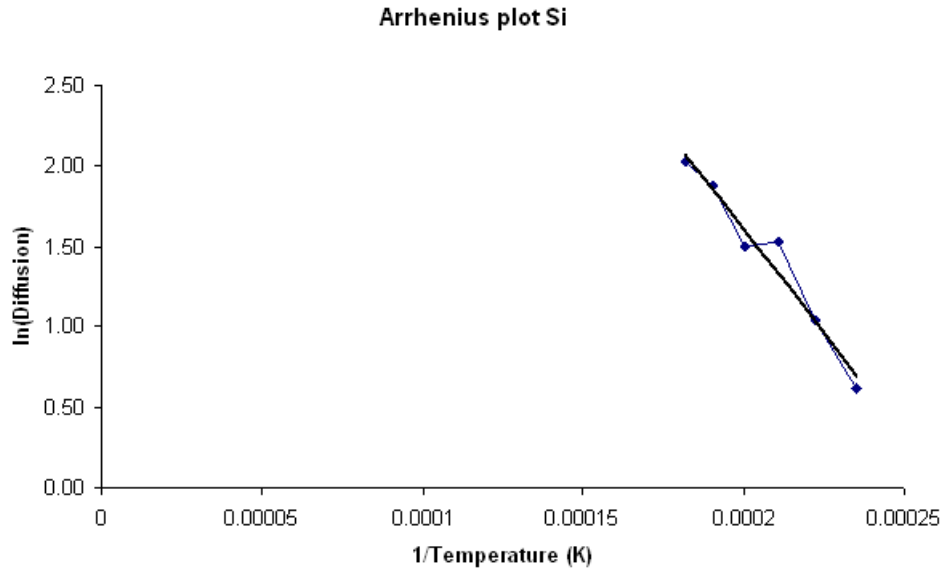


Figure 4.9: Arrhenius plot for silicon with PbO_2 as the starting structure (the lowest R^2 of all the starting structures for silicon)

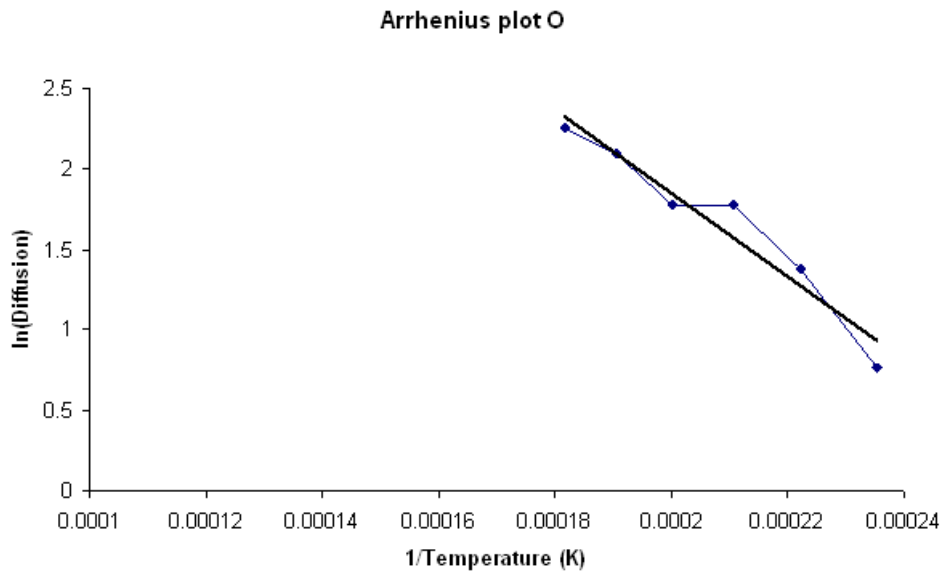


Figure 4.10: Arrhenius plot for oxygen with PbO_2 as the starting structure (the lowest R^2 of all the starting structures for oxygen)

in experiments below the melting point, described above (0.87, 1.26, 1.3 and 4.7 eV). The calculated activation energies for silicon are much lower than the experimental value (7.6 eV) for silicon below the melting point.

MD simulations using the BKS potential described by J. Horbach, W. Kob and K. Binder [52] result in activation energies significantly different from those in this study, at 4.9 eV for silicon and 4.45 eV for oxygen. This result might be explained by a number of differences: The paper uses a time step of 1.6 fs compared to one of 0.5 fs in the work described here. Simulations in the paper were carried out at constant volume, whereas in the present study the volume was allowed to fluctuate. Finally, the temperature range used for the calculations in the paper is 2900 K to 6100 K compared to 4000 K to 6000 K in the simulations discussed here.

It might be expected that the activation energy for silicon would be significantly higher than that for oxygen, since in order for silicon to diffuse four bonds must be broken, whereas for oxygen only two bonds need to be broken. This difference is observed in experimental data below the melting point, discussed earlier. However, in calculations shown in table 4.4, although the activation energy of silicon is generally slightly higher than that of oxygen, the difference is not as

great as between experimental values below the melting point. The calculated values shown in the table suggest that at temperatures above the melting point the diffusion mechanisms of both silicon and oxygen are similar.

4.5 Energy and volume

Figures 4.11 and 4.12 show the final energies and volumes of simulated melts starting with different crystal structures. Simulations were carried out at a range of temperatures. The number after the name of the crystal structure refers to the number of silicon atoms in the structure. 17 out of a total of 63 simulations did not successfully complete and are not shown in the figures.

The spread of final energies between different starting structures decreases with increasing temperature with a range of -55.45 eV to -54.66 eV at 4000 K and -52.40 eV to -52.08 eV at 6000 K. This is also the case for final volumes with a range of 25.09 Å³ to 44.93 Å³ at 4000 K and 38.22 Å³ to 38.54 Å³ at 6000 K. This provides some evidence that the starting structure does not affect the final structure of the melt, providing the temperature is sufficiently high.

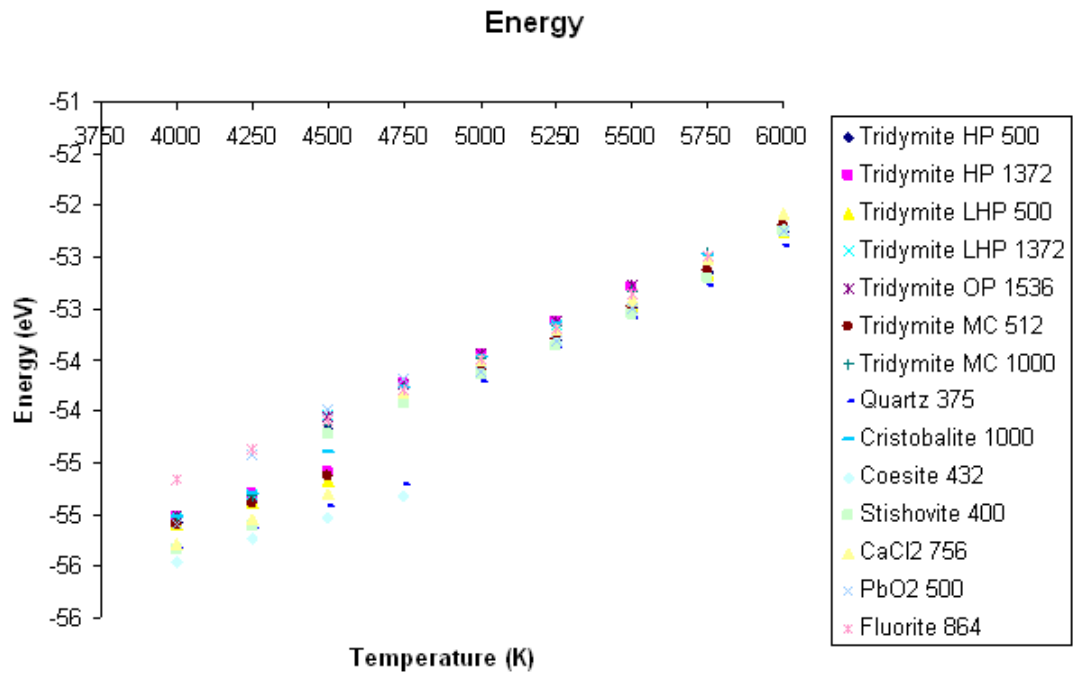


Figure 4.11: Final energy for simulations of a number of silica crystal structures at a range of temperatures

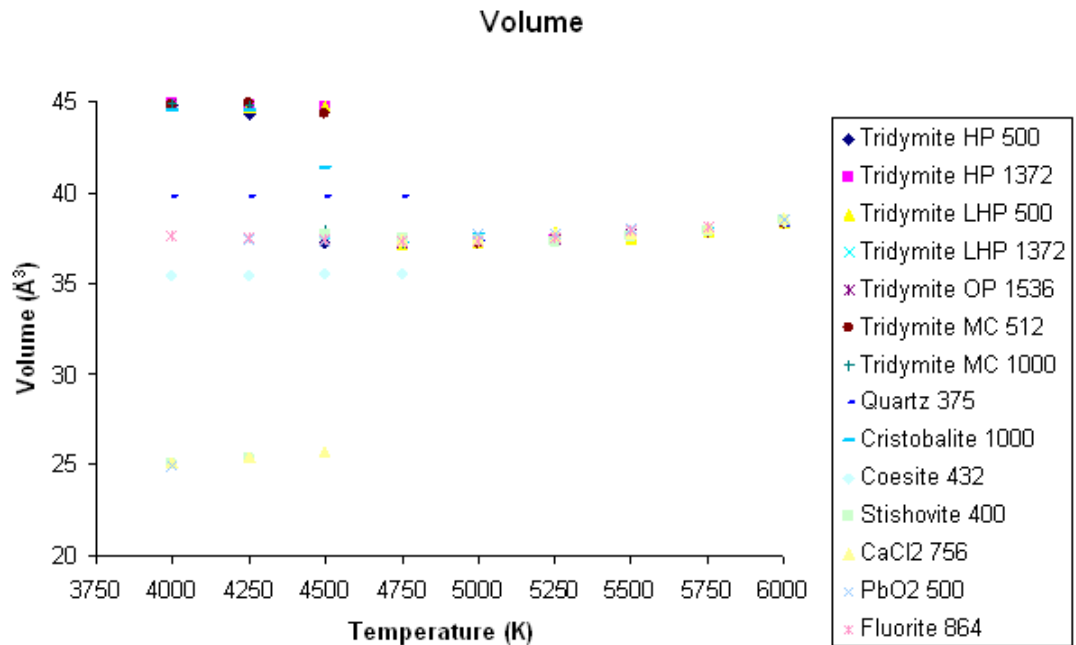


Figure 4.12: Final volume for simulations of a number of silica crystal structures at a range of temperatures

Table 4.5 shows energies and volumes for the six vitreous structures described in section 4.2. All results are at 1 K. The first column contains the original crystal structure from which the melt was produced. The third column contains the temperature from which the structure was quenched.

Original structure	Number of silicon atoms	Temperature of melt (K)	Energy (eV)	Volume (\AA^3)
LHP tridymite	500	6000	-55.618	37.594
MC tridymite	512	6000	-55.645	37.725
Cristobalite	1000	5000	-56.096	38.051
Stishovite	400	6000	-55.5025	37.723
PbO ₂	500	6000	-55.614	37.864
Fluorite	864	5000	-56.110	37.817

Table 4.5: Energy and volume for vitreous structures

Although the volumes for vitreous structures quenched from 5000 K and 6000 K are comparable, the energies for vitreous structures from 6000 K are higher than those from 5000 K, illustrating the discussion in section 4.2 on quench rates in computational studies being several orders of magnitude faster than those in experiments. The reason for this is that although melts at 5000 K and 6000 K are at an equilibrium, the quench rate is too fast for the structures to relax and find a configuration with a sufficiently low energy state. The quenching for the 6000 K structures between 6000 K and 5000 K is an additional period with a quench rate that is too fast which does

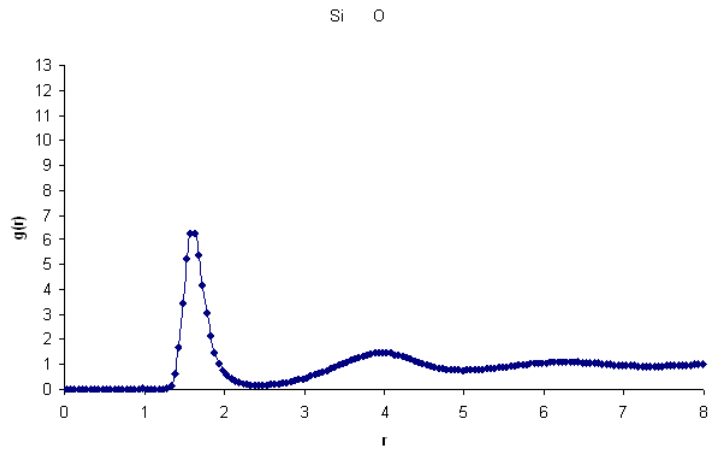
not take place for structures cooled from 5000 K.

No experimental data were found on the density of a silica melt. The experimental density of silica glass has been found to be 2.2 g/cm^3 [84]. The density of a melt produced from simulations in this thesis is approximately 2.60 g/cm^3 and that of a vitreous structure approximately 2.65 g/cm^3 . These numbers are significantly larger than the experimental value for glass and might be explained by deviations from experiment in coordination number, discussed in section 4.7. The densities presented here are, however, consistent with other similar computer simulations described in [85] and [86], and the divergence is almost certainly a consequence of the fast quench rates in computer simulations.

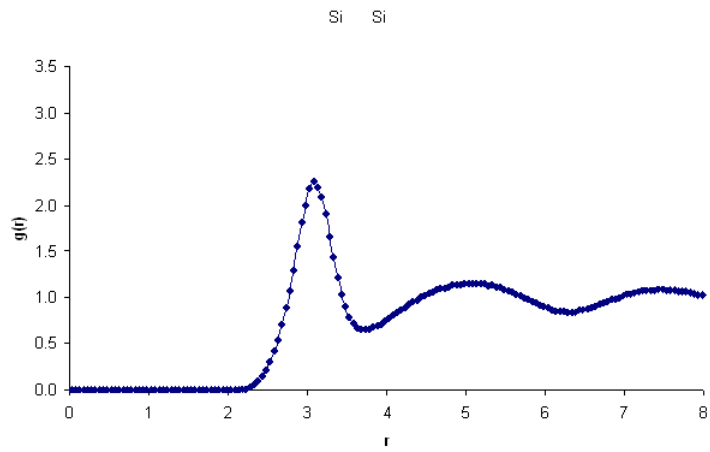
4.6 Bond lengths, angles and Pair Distribution Functions

Figures 4.13 and 4.14 show typical examples of Pair Distribution Functions (PDFs) for a melt and a vitreous structure respectively.

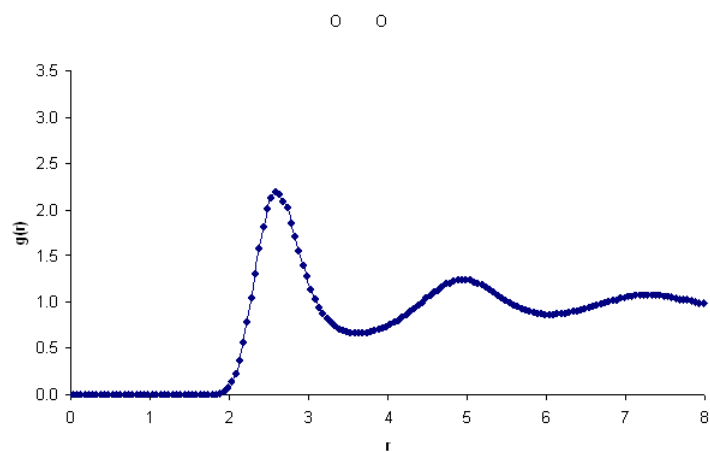
All plots have the appearance that would be expected from an amorphous structure, having no long range order. However, both struc-



(a) PDF Si-O

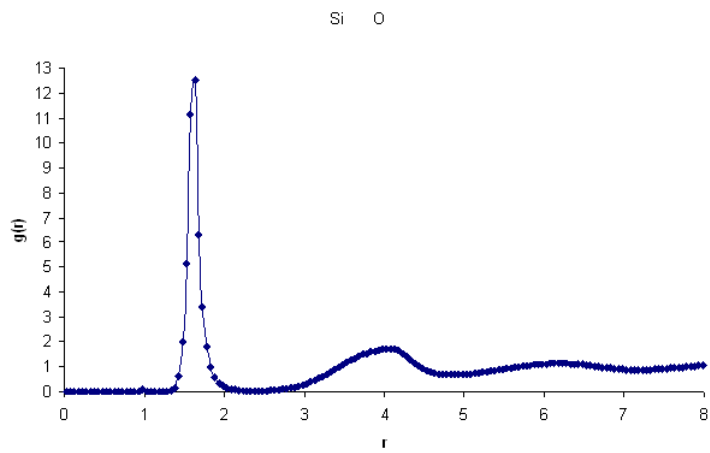


(b) PDF Si-Si

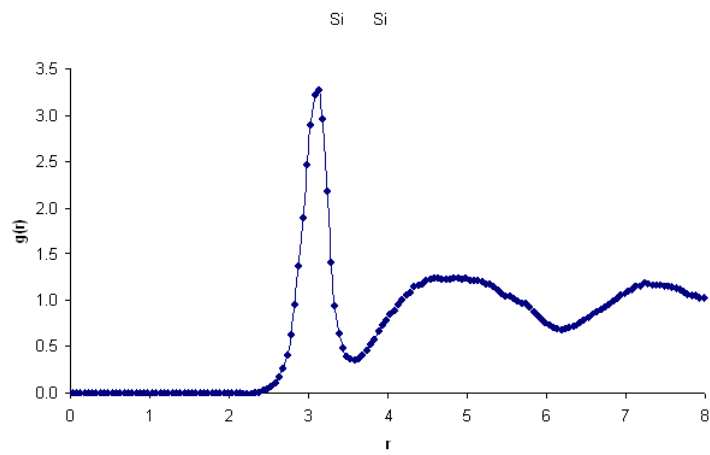


(c) PDF O-O

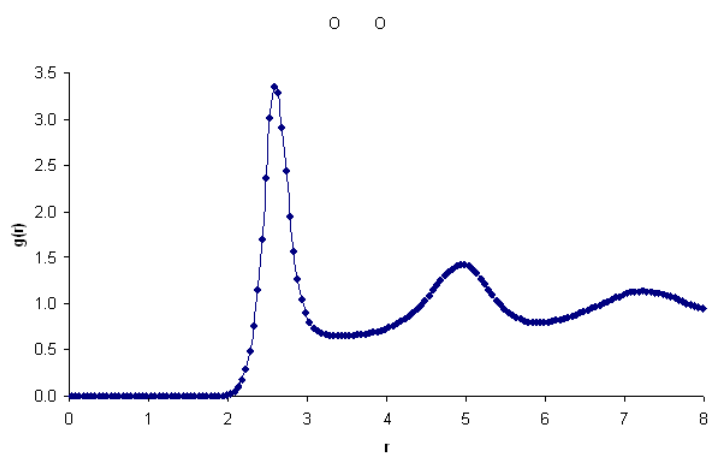
Figure 4.13: Example of a PDF of a melt (at 6000 K)



(a) PDF Si-O



(b) PDF Si-Si



(c) PDF O-O

Figure 4.14: Example of a PDF of a vitreous structure

tures display significant short and medium range order (up to approximately 8 Å) as found in X-ray diffraction experiments [87]. Vitreous structures have a larger amount of short-range order than liquids, which can be seen by the first peak for all three PDFs being higher and narrower in the vitreous structure. The short and medium range order in both types of structure is explored further in the following discussion on bond lengths and angles and in section 4.7 which investigates coordination.

Unlike crystalline structures, experimental data on bond lengths and angles for amorphous structures can generally only give average values. Computational techniques can provide more detailed information and are useful for investigating the distributions of these properties.

In order to calculate bond lengths and angles a cut-off must be specified beyond which atoms are not considered to be bonded. In a crystalline structure this is straightforward. However, in an amorphous structure where there is a continuous range of bond lengths and angles the choice of cut-off is salient. This issue is illustrated in Figures 4.15 and 4.16 which show Si-O distance against cumulative mean coordination number for a melt and a vitreous structure respectively (from a melt of LHP tridymite at 6000 K). The y-axis

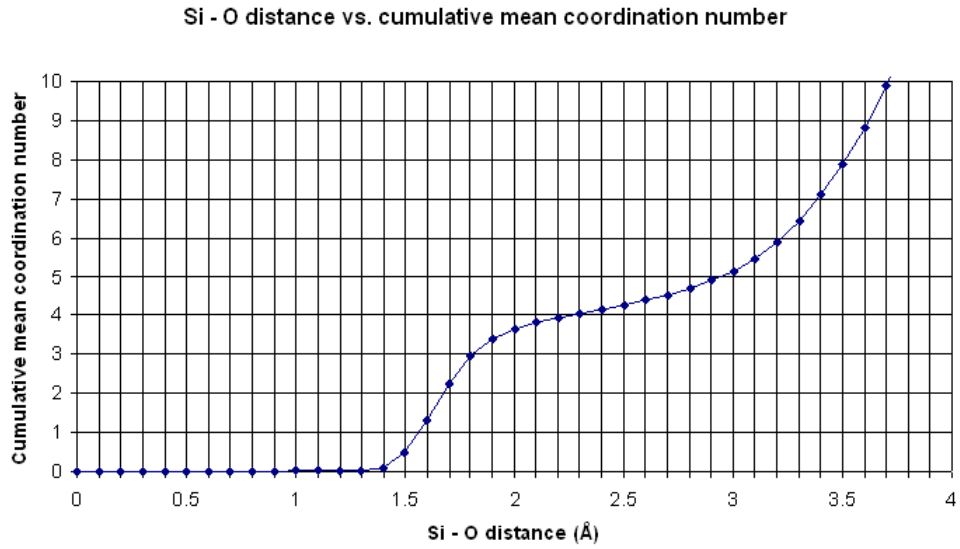


Figure 4.15: Si-O distance against cumulative mean coordination for a melt (at 6000 K)

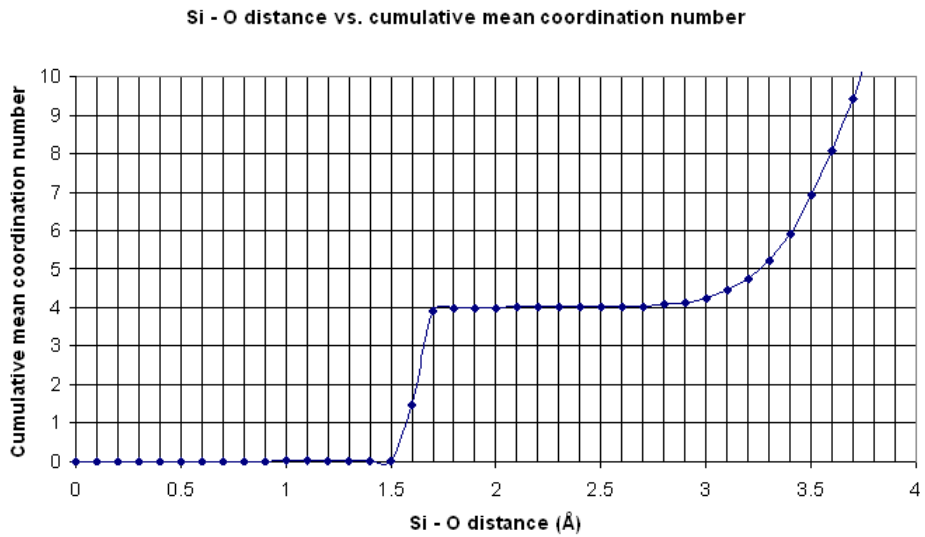


Figure 4.16: Si-O distance against cumulative mean coordination for a vitreous structure

shows the number of oxygen atoms near a silicon atom within the distance on the x-axis, averaged over all silicon atoms. Figure 4.16 shows that in a vitreous structure there is a clear cut first coordination shell and a cut-off anywhere in the range 1.8 Å and 2.6 Å would be appropriate. However, Figure 4.15 shows that there is no clear-cut first coordination shell in a melt. For a melt a cut-off of 2.5 Å was chosen as this was the point on the graph with the smallest gradient (also the minimum point after the first peak in the PDF). The same value was also chosen as the cut-off for a vitreous structure as it is in the range on the graph where the line is flat. However, calculations for bond lengths and angles were additionally carried out using cut-offs of 2.0 Å and 3.0 Å in order to test the sensitivity of the results.

Figures 4.17 to 4.19 show bond length distributions, O-Si-O angle distributions and Si-O-Si angle distributions of a melt at 6000 K (with LHP tridymite as the starting structure) with a cut-off of 2.5 Å. Figures 4.20 to 4.22 show the same distributions but for a vitreous structure for the same starting structure. Similar distributions were obtained for the remaining starting structures.

Table 4.6 shows mean bond lengths and their standard deviations for melts and vitreous structures for different starting structures

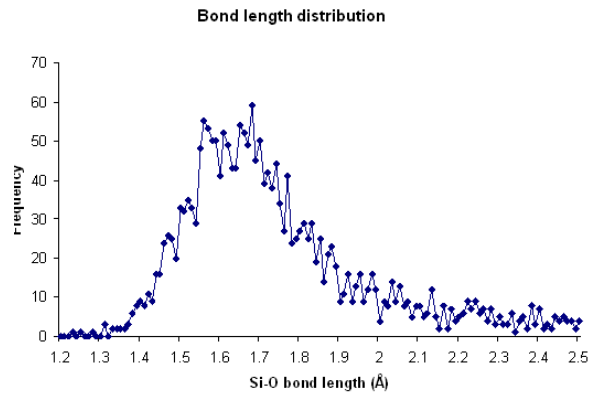


Figure 4.17: Typical Si-O bond length distribution for a melt (at 6000 K)

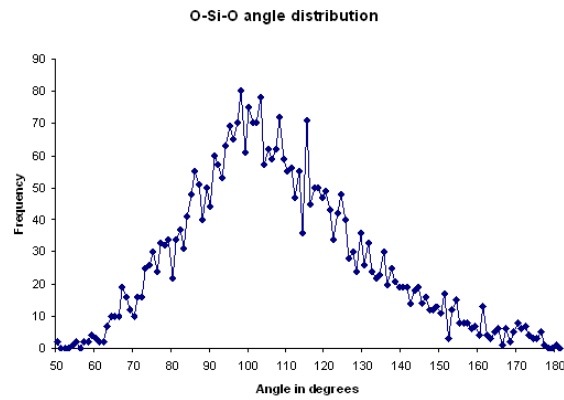


Figure 4.18: Typical O-Si-O angle distribution for a melt (at 6000 K)

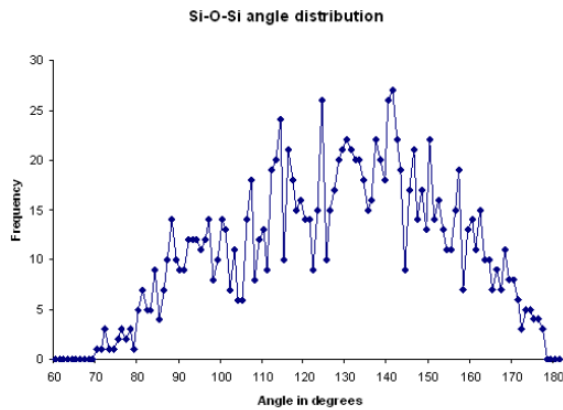


Figure 4.19: Typical Si-O-Si angle distribution for a melt (at 6000 K)

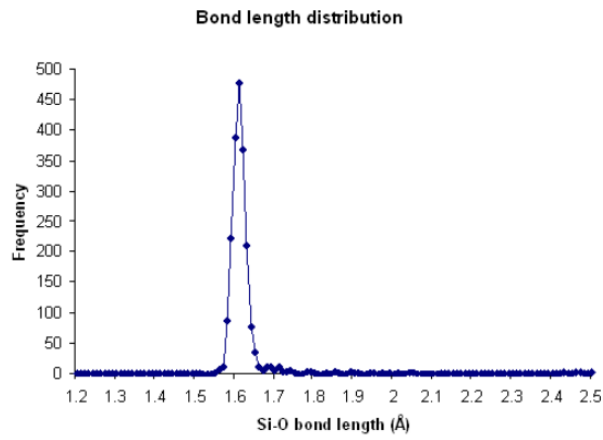


Figure 4.20: Typical bond length distribution for a vitreous structure

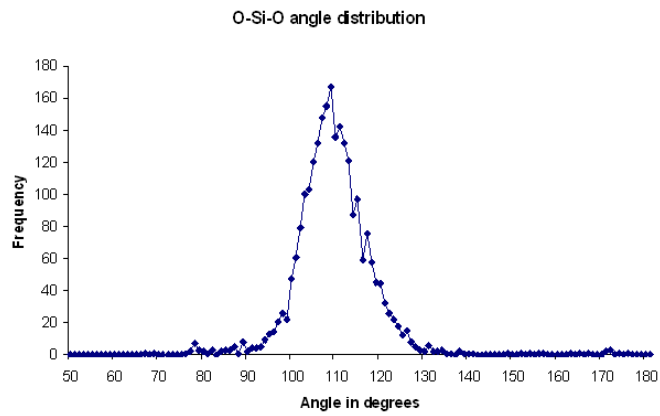


Figure 4.21: Typical O-Si-O angle distribution for a vitreous structure (the ideal O-Si-O angle is 109°)

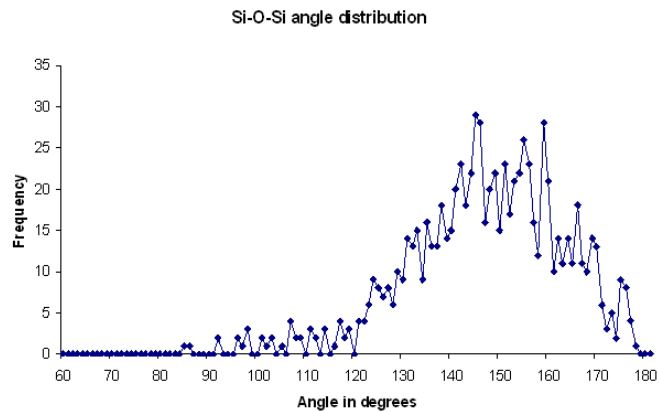


Figure 4.22: Typical Si-O-Si angle distribution for a vitreous structure

(i.e. means and standard deviations for the graphs shown above for different starting structures). Table 4.7 shows mean O-Si-O angle distributions and table 4.8 shows mean Si-O-Si angle distributions. Calculations using a cut-off of 2.0 Å are also shown.

Starting structure	Cut-off = 2.5 Å				Cut-off = 2.0 Å	
	Mean Si-O distance (Å) for a melt	Standard deviation	Mean Si-O distance Å for a vitreous structure	Standard deviation	Mean Si-O distance (Å) for a melt	Mean Si-O distance (Å) for a vitreous structure
Tridymite LHP	1.732	0.239	1.607	0.101	1.658	1.605
Tridymite MC	1.741	0.252	1.607	0.078	1.658	1.605
Cristobalite	1.723	0.221	1.609	0.040	1.664	1.608
Stishovite	1.742	0.249	1.608	0.100	1.661	1.604
PbO ₂	1.746	0.249	1.610	0.074	1.663	1.608
Fluorite	1.725	0.222	1.610	0.040	1.664	1.607

Table 4.6: Bond lengths for melts and vitreous structures for a number of starting structures

Starting structure	Cut-off = 2.5 Å				Cut-off = 2.0 Å	
	Mean O-Si-O angle for a melt	Standard deviation	Mean O-Si-O angle for a vitreous structure	Standard deviation	Mean O-Si-O angle for a melt	Mean O-Si-O angle for a vitreous structure
Tridymite LHP	107.73	22.37	109.18	8.92	109.47	109.33
Tridymite MC	106.76	23.50	109.26	8.23	109.49	109.31
Cristobalite	107.10	21.60	109.24	8.14	109.04	109.28
Stishovite	106.94	24.29	109.18	8.92	109.33	109.28
PbO ₂	106.87	23.18	109.16	9.09	109.50	109.23
Fluorite	106.96	22.17	109.31	7.63	108.88	109.33

Table 4.7: O-Si-O angles for melts and vitreous structures for a number of starting structures

Starting structure	Cut-off = 2.5 Å				Cut-off = 2.0 Å	
	Mean Si-O-Si angle for a melt	Standard deviation	Mean Si-O-Si angle for a vitreous structure	Standard deviation	Mean Si-O-Si angle for a melt	Mean Si-O-Si angle for a vitreous structure
Tridymite LHP	127.60	22.76	146.54	15.96	133.62	148.34
Tridymite MC	127.10	24.80	147.13	15.02	133.97	147.52
Cristobalite	130.91	23.44	147.61	14.69	137.25	147.95
Stishovite	126.53	23.34	146.54	15.96	132.79	147.16
PbO ₂	127.19	24.25	146.79	15.80	133.91	147.25
Fluorite	129.95	23.64	148.07	14.20	135.81	148.27

Table 4.8: Si-O-Si angles for melts and vitreous structures for a number of starting structures

The values for all three properties do not significantly differ between the different starting structures for vitreous structures. This is also the case for bond lengths and O-Si-O angles for melts. However, the mean Si-O-Si angles in melts with cristobalite and fluorite as starting structures are slightly higher than for the remaining structures. This difference may be due to the simulations for those two structures being at 5000 K (the highest possible temperature that resulted in a successfully completed simulation) rather than 6000 K which was used for the remaining structures.

As would be expected from the earlier discussion, the properties of a vitreous structure do not significantly differ when a cut-off of 2.0 Å is used rather than 2.5 Å, as they are both in the appropriate range of 2.0 Å to 2.6 Å. However, this is not the case for a melt, showing that the results are quite sensitive to the choice of cut-off.

Figures 4.17 to 4.22 show that the distributions in a melt are wider than those in a vitreous structure. This is confirmed by tables 4.6 to 4.8 where the standard deviations are larger in a melt than in a vitreous structure. These differences support the discussion relating to PDFs, above, that there is more short and medium range order in a vitreous structure than in a melt.

We now compare results obtained here with the experimental and computational literature on silica liquid and glasses.

There are no experimental data available for bond lengths and angles of a silica melt. A simulation of a melt using a two-body potential derived from Car-Parrinello molecular dynamics simulations is described in [88]. At a temperature of 3600 K a mean Si-O-Si angle of 150° was found. This value is higher than the mean Si-O-Si angles of simulations of melts in this thesis. However, the parameters for the potential used are derived using a very different method to those of the BKS potential.

Considering now the vitreous structure, one of the first important papers on the Si-O bond length in vitreous materials (published in 1969) is that of R. L. Mozzi and B. E. Warren [87]. In X-ray diffraction experiments they found that the mean bond length of vitreous silica is 1.62 \AA , which is a little higher than the calculations in the present study. More recently (1994) A. C. Wright [39] carried out two X-ray diffraction and two neutron scattering experiments. The two X-ray diffraction experiments give mean Si-O bond lengths of 1.626 ± 0.004 and $1.619 \pm 0.002 \text{ \AA}$. The two neutron scattering experiments give mean Si-O bond lengths of 1.608 ± 0.004 and $1.605 \pm 0.003 \text{ \AA}$. The result of calculations for a vitreous struc-

ture are consistent with both the neutron scattering experiments but less so with the X-ray diffraction experiments. According to G. H. Beall [89] the Si-O bond length of vitreous silica is between 1.59 and 1.62 Å. This is based on X-ray, neutron and electron diffraction experiments. The results for all the calculated quenched structures are in the middle of this range.

In the earliest X-ray, neutron and electron diffraction experiments described in [89], the mean O-Si-O angle was found to be 109.5° , which is a little higher than for calculations in this study. In high energy X-ray diffraction experiments described in [90] it was found to be 109.3° which is consistent with calculations.

As can be seen from the standard deviation column for a vitreous structure in table 4.8 there is a wide distribution of Si-O-Si angles in a silica glass. In Mozzi and Warren's X-ray diffraction experiments [87] the distribution of Si-O-Si angles was found to be between 120° and 180° with a maximum at 144° , which is confirmed by studies described in [91] and [92]. In high energy X-ray diffraction experiments carried out by H. F. Poulsen, J. Neuefeind, H.-B. Neuman, J. R. Schneider and M. D. Zeidler [90] the maximum was determined to be at 147° . NMR experiments by T. M. Clark, P. J. Grandinetti, P. Florian and J. F. Stebbins [93] also found the max-

imum angle to be 147° . In NMR experiments by E. Dupree and R. F. Pettifer in [40], it was found that the Si-O-Si angle distribution is wide with roughly constant probability in the range 140° - 155° . These findings are all consistent with results from this thesis. Simulations of a vitreous structure using the BKS potential by X. Yuan and A. N. Cormack [59] found a most probable Si-O-Si angle of 152° . This value is higher than calculations in this thesis. However, simulations described in the paper differ from those described here in that they were carried out at constant volume.

Another piece of evidence that the simulated vitreous structures produced are similar to experimental structures is shown in the similarity between Figure 4.23, which shows the experimental vibrational density of states taken from experiments by S. N. Taraskin and S. R. Elliott [95] (the line labelled “true” is the one to be compared), and Figure 4.24, which shows a typical spectrum calculated from vitreous structures in this thesis. For further density of states calculations see [96] which uses MD to simulate a glass, calculates the density of states and then characterises the vibrations (e.g. bond stretching, angle bending, etc.).

There is no experimental data available on torsion (Si-O-Si-O) angles. Figure 4.25 shows a typical distribution of torsion angles in a

S.N. Taraskin, S.R. Elliott / Physica B 234-236 (1997) 452-454

453

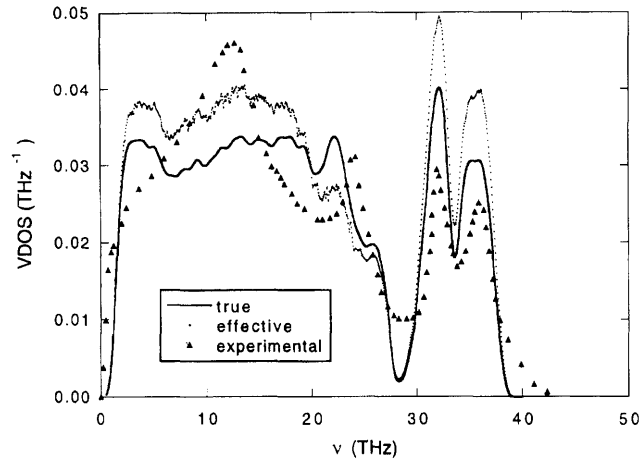


Fig. 1. True (solid line), effective (dotted line) and experimental (triangles) [7] vibrational density of states for vitreous silica, the former two obtained from computer simulations.

Figure 4.23: Experimental density of states for vitreous silica taken from [94]

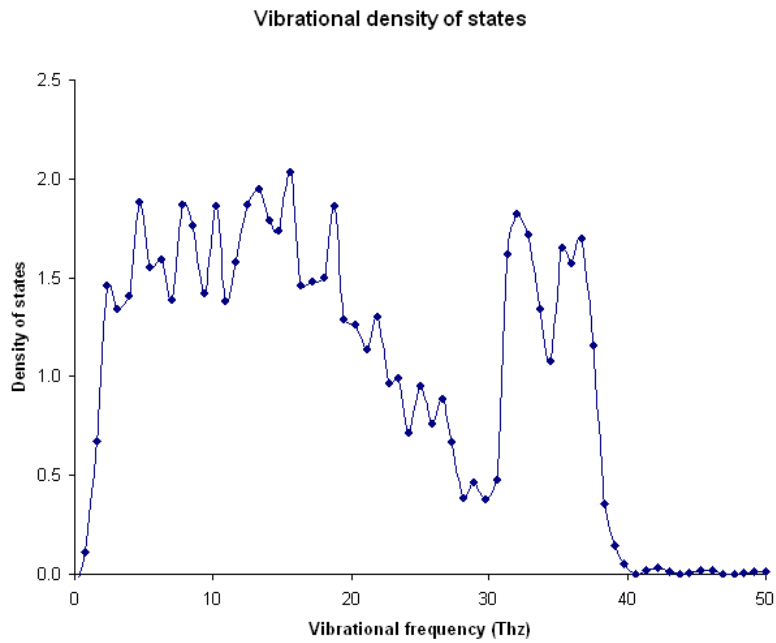


Figure 4.24: A typical density of states spectrum for a vitreous structure in this thesis

vitreous structure from this thesis (this particular graph is from a vitreous structure produced from a melt of LHP tridymite at 6000 K). The distribution is quite uniform. The mean angle for this distribution is 90.3° (with a standard deviation of 52) which confirms this uniformity (as the angles can only take values between 0° and 180°).

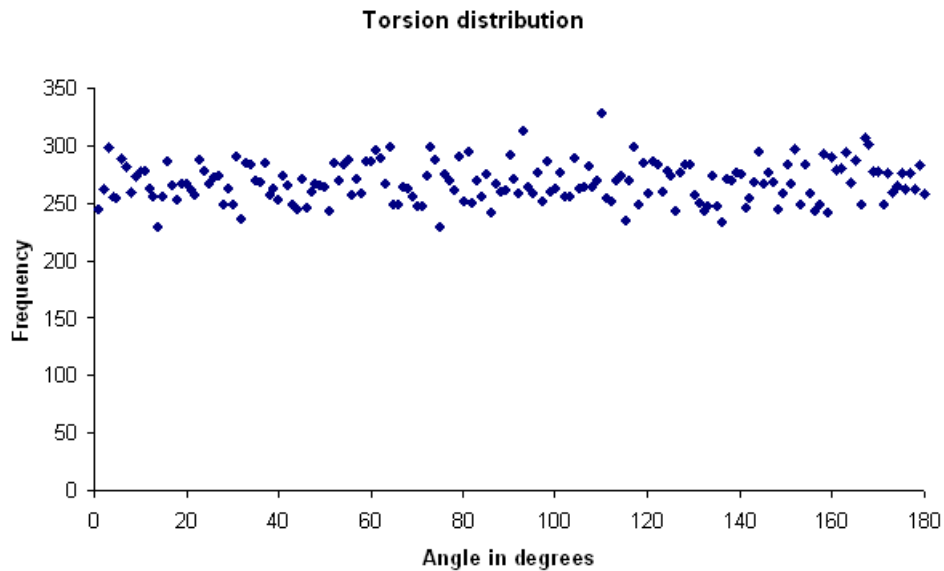


Figure 4.25: Distribution of torsion angles for a vitreous structure

4.7 Coordination of silica melts and glasses

It has generally been thought that a vitreous structure is “almost always tetrahedrally coordinated” [31] (the number of oxygen atoms surrounding each silicon atom is four).

Table 4.9 taken from [39] shows the mean coordination number for a vitreous structure for four different experiments: two X-ray diffraction experiments and two neutron diffraction experiments. No data could be found on the coordination of a silica melt.

Experiment	Coordination number
X-ray	3.77 ± 0.12
X-ray	3.58 ± 0.09
Neutron	3.85 ± 0.16
Neutron	3.79 ± 0.14

Table 4.9: Mean coordination number from X-ray and neutron diffraction experiments taken from [39]

As with bond lengths and angles, a cut-off must be chosen beyond which atoms are not considered to be bonded when performing calculations. The same cut-off (2.5 Å) as described in the previous section was chosen.

Tables 4.10 and 4.11 show mean coordination numbers for calculated melts and vitreous structures respectively for a number of simulations. All vitreous structures are at 1 K.

Figure 4.26 shows the distribution of coordination number for a number of simulations of a melt. The x-axis shows the original crystal structure which was melted and the temperature of the melt.

Figure 4.27 shows the distribution of coordination number for dif-

ferent simulations of a vitreous structure. The x-axis shows the original crystal structure which was melted and the temperature from which it was quenched.

Starting structure	Temperature (K)	Mean coordination number
Cristobalite	5000	4.071
Fluorite	5000	4.132
PbO ₂	6000	4.026
Stishovite	6000	4.147
LHP Tridymite	6000	4.180
MC Tridymite	6000	4.234

Table 4.10: Mean coordination number of a melt for a number of starting structures

Starting structure	Temperature from which glass was quenched (K)	Mean coordination number
Cristobalite	5000	4.025
Fluorite	5000	3.932
PbO ₂	6000	4.108
Stishovite	6000	3.884
LHP Tridymite	6000	4.008
MC Tridymite	6000	4.018

Table 4.11: Mean coordination number of a vitreous structure for a number of starting structures

In the melts (Figure 4.26) there are a significant number of 3 and 5 coordinated atoms, with only approximately 60% of atoms being four coordinated. There does not appear to be a significant difference in the distribution of coordination between the different starting structures.

It is not clear why the distribution for the vitreous structures (Figure 4.27) varies between the different starting structures. It does not

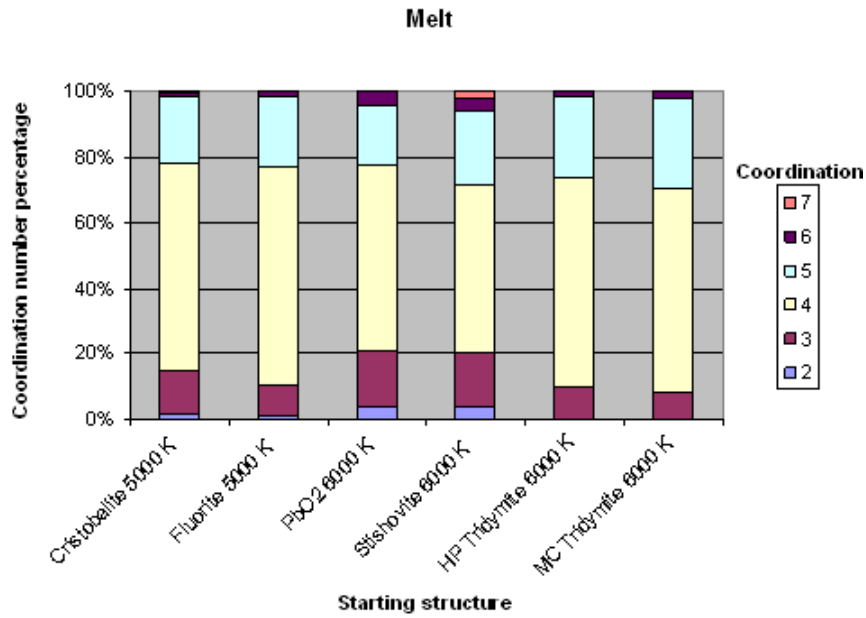


Figure 4.26: Distribution of coordination number for a number of melts

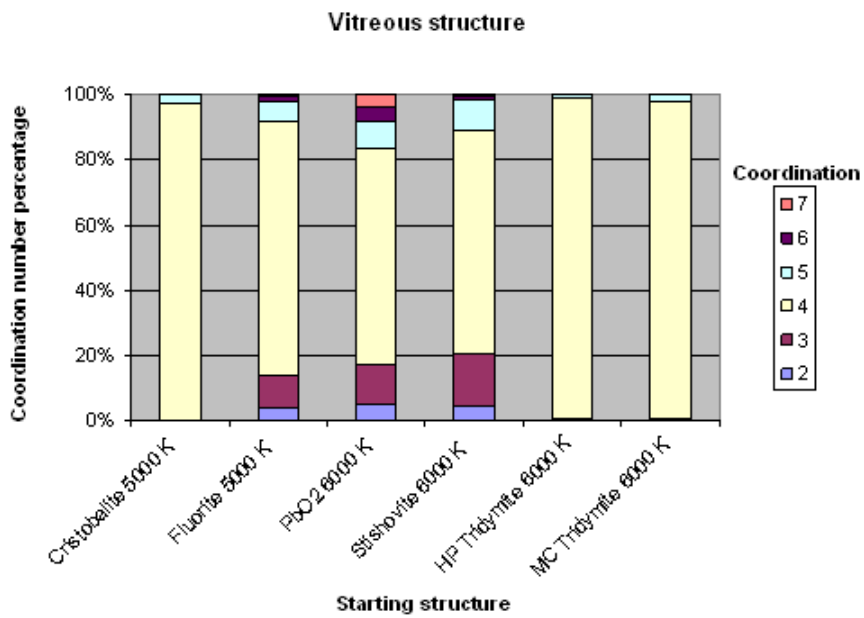


Figure 4.27: Distribution of coordination number for a number of vitreous structures

appear to be related to either the temperature or the diffusion coefficient of the melt. The starting structures with fewer 4 coordinated atoms are the high pressure polymorphs, although it is not clear why this is the case because the coordination of the melts from which the vitreous structures were made all have a similar distribution (Figure 4.26).

The mean calculated coordination numbers for a melt (table 4.10) are a little higher than those calculated for a vitreous structure (table 4.11). The mean calculated coordination numbers for a vitreous structure are significantly higher than the experimental values (table 4.9) for most of the starting structures. This may be due to the fast quench rate, which is several orders of magnitude faster in computational simulations than for experiment. The true melted structure probably has a significantly higher coordination than the vitreous structure. The structure being quenched computationally does not have sufficient time to relax from the melted structure to a lower mean coordination. This would also explain the higher density (discussed in section 4.5) found in simulated vitreous structures compared to experiment. The findings of the simulations described here do not appear to contradict the hypothesis that the vast majority of silicon atoms in vitreous silica are tetrahedrally coordinated.

4.8 The effect of defects in a crystal on its melting behaviour

In this section we explore the effect of defects on the melting behaviour of a silica crystal, for which little experimental data was found. A number of simulations at a range of temperatures with differing numbers of defects were carried out. The defects were made by removal of two oxygen atoms for every one silicon atom to ensure charge neutrality. One defect represents the removal of one SiO_2 cluster, two defects represent the removal of two SiO_2 clusters, etc. The crystal structure used as the initial configuration was Hexagonal Packed (HP) tridymite with 500 silicon atoms. Figures 4.28, 4.29, 4.30 and 4.31 show a comparison of the energies, volumes and diffusion coefficients of the structures with defects with those of the perfect crystal structure. 3 out of a total of 49 simulations did not successfully complete and are not shown in the figures.

The energies, volumes and diffusion coefficients are similar for all structures at temperatures up to 3000 K. However, at intermediate temperatures (3500 K to 4500 K) there is a spread of values for these properties, which provides some evidence that defects significantly lower the melting point of silica. A small number of defects appears

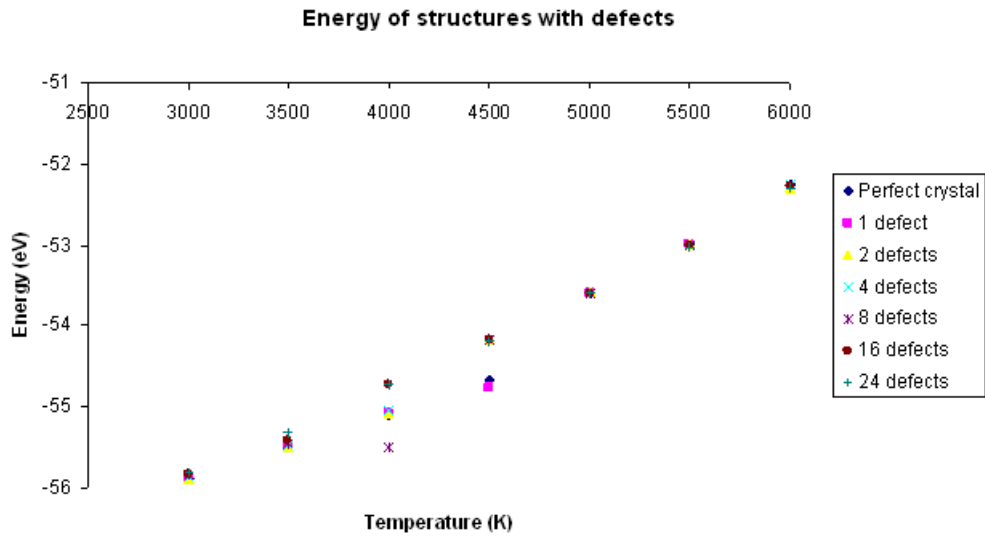


Figure 4.28: Final energy for simulations with the LHP tridymite structure with 500 silicon atoms with differing numbers of defects at a range of temperatures

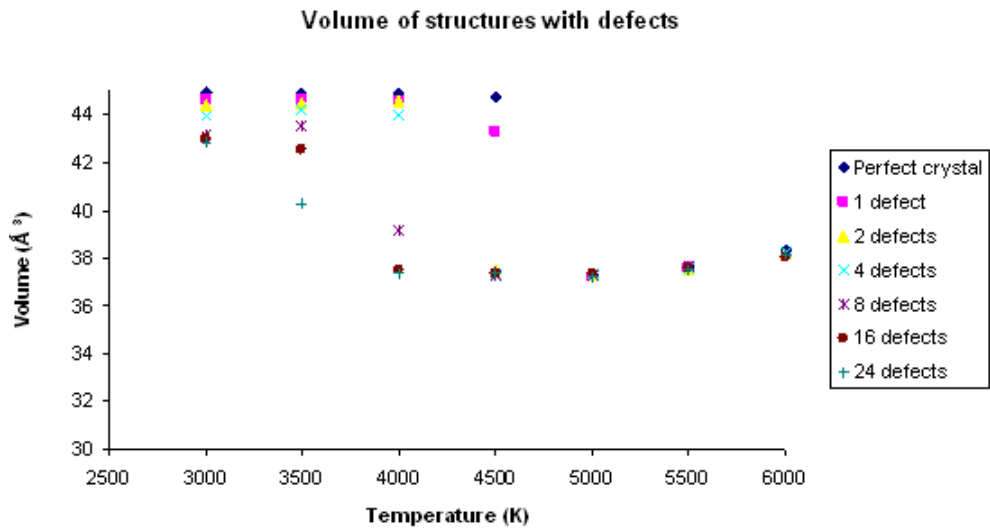


Figure 4.29: Final volume for simulations with the structure LHP tridymite with 500 silicon atoms with differing numbers of defects at a range of temperatures

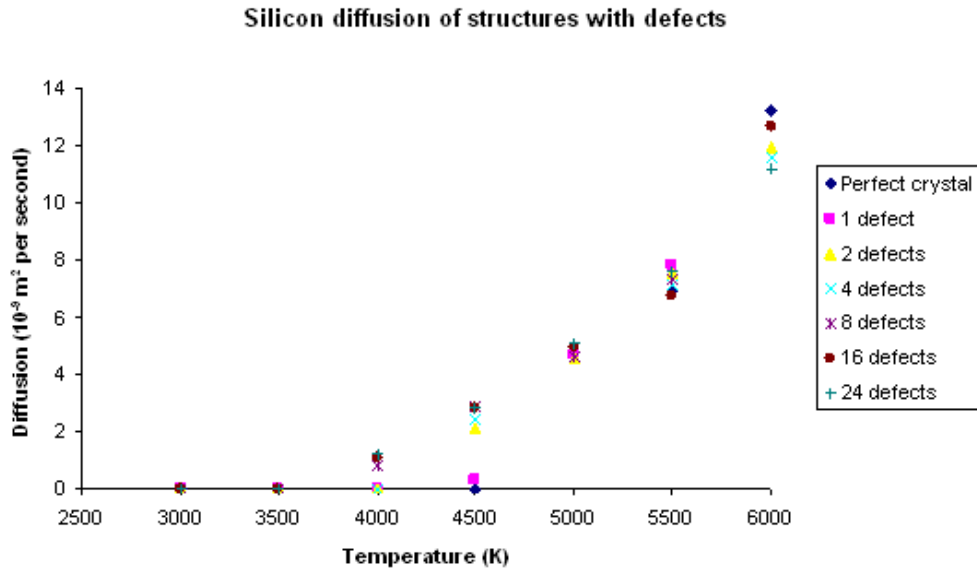


Figure 4.30: Diffusion coefficients for silicon with the LHP tridymite structure with 500 silicon atoms with differing numbers of defects at a range of temperatures

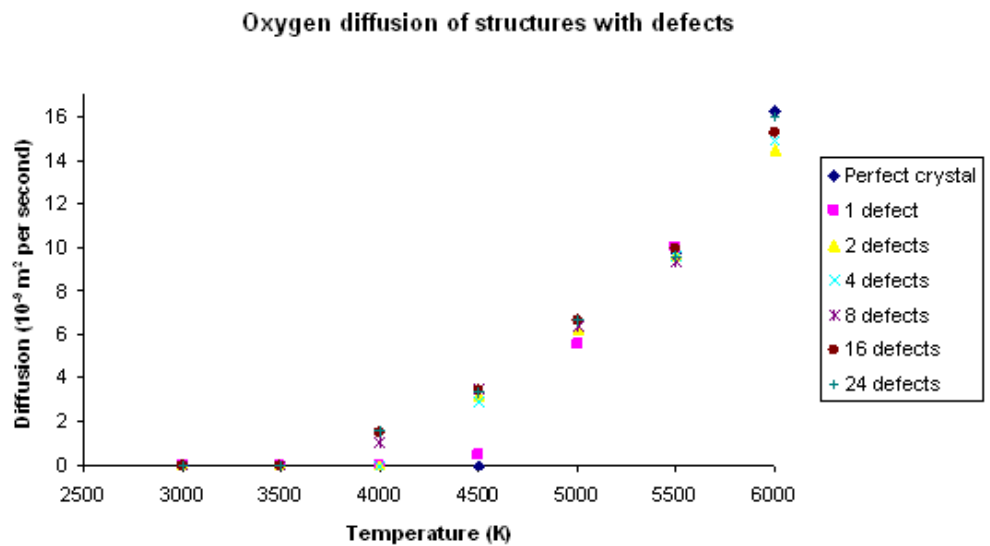


Figure 4.31: Diffusion coefficients for oxygen with the LHP tridymite structure with 500 silicon atoms with differing numbers of defects at a range of temperatures

to be sufficient to make a significant difference. For example, for simulations at 4500 K, the diffusion coefficient of a perfect crystal is $0.005 \cdot 10^{-9} m^2/s$, whereas with only two defects it is $2.136 \cdot 10^{-9} m^2/s$. At higher temperatures (5000 K and above) defects do not appear to make a significant difference to the energies, volumes and diffusion coefficients. These results indicate that the presence of defects significantly lowers the melting temperature.

4.9 The nature of the Si-O bond in a melt

This section explores the duration of the Si-O bond and the extent to which silicon and oxygen atoms move together in a silica melt. Two methods were used. In the first, silicon and oxygen atoms bonded together at a particular point in the simulation were tagged (atoms were deemed to be bonded if they were within a certain cut-off, as discussed in section 4.6). The duration that two atoms remained within the cut-off for the remainder of the simulation was recorded and averaged over all atoms in the structure. The calculations were carried out for the last 10 ps of a 100 ps simulation to ensure that the structure was a typical melt. Table 4.12 shows the mean duration in ps that atoms remained within the specified cut-off for a

melt of LHP tridymite with 500 silicon atoms at four different temperatures. Similar results were obtained for the other melted crystal structures used in this thesis.

Temperature (K)	Cut-off (\AA)		
	2.0	2.5	3.0
4500	1.007	10	10
5000	0.400	2.005	2.354
5500	0.337	1.354	1.574
6000	0.309	0.891	1.038

Table 4.12: Bond length duration (in picoseconds) at different temperatures

At temperatures of 4500 K and below bonds are not broken. This can be seen by the mean duration of a bond for cut-offs of 2.5 and 3.0 \AA at 4500 K being equal to the total simulation time. The value of 1.007 ps for a cut-off of 2.0 \AA at this temperature shows that this value is too small to give meaningful results, as the atoms are vibrating with a large amplitude and vibrate beyond this cut-off. The table shows that at temperatures of 5000 K and above the duration of the Si-O bond is very short, approximately 2 ps at 5000 K and approximately 1 ps at 6000 K. Figure 4.32 shows the distribution of bond length duration for the calculation at 6000 K with a cut-off of 2.5 \AA .

In the second method atoms bonded together at a point in the simulation were tagged, as above. At the end of the simulation, mean

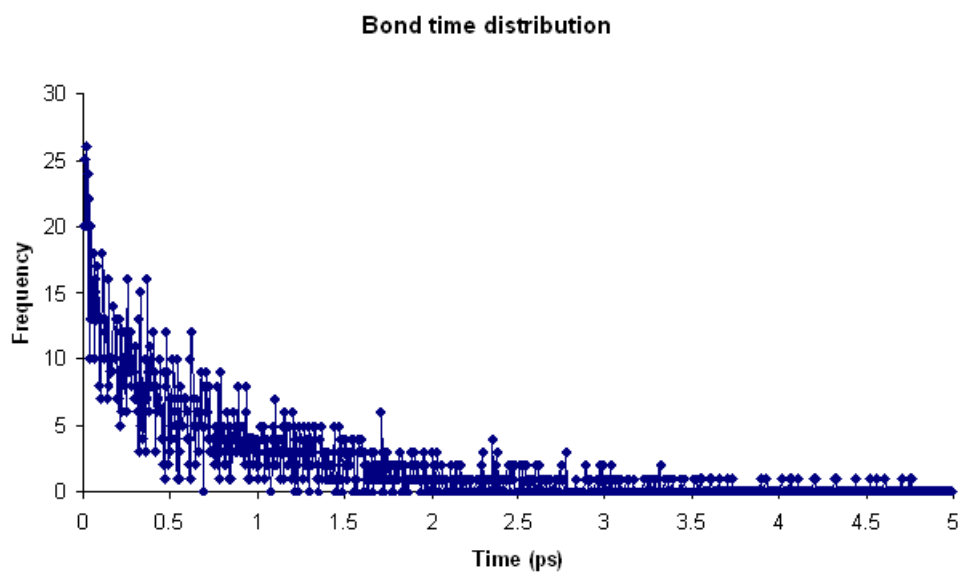


Figure 4.32: Bond time distribution for a silica melt

Si-O distances of all atoms which were bonded together at the beginning were compared with the mean Si-O distances of all atoms whether bonded or not (i.e. distances between each silicon atom and every other oxygen atom in the structure and vice versa). Figure 4.33 shows this calculation starting at the 50 ps point in a 100 ps calculation (so the starting structure is amorphous) with LHP tridymite as the starting structure and run at 6000 K.

Figure 4.34 shows the same calculation for an entire simulation (so the starting structure is a crystal) with the PbO_2 polymorph as the starting structure and run at 6000 K. Similar behaviour is seen for melts for all crystalline starting structures.

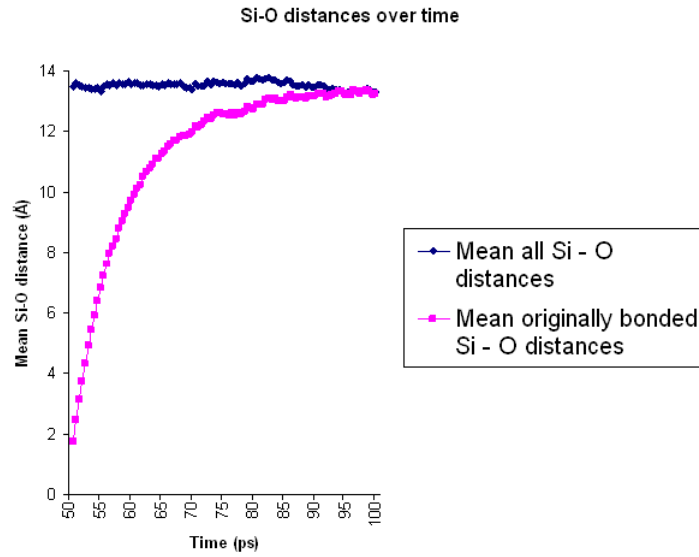


Figure 4.33: Si-O distances for atoms originally bonded against Si-O distances for all atoms in a silica melt with a melt as the starting structure for the last 50 ps of a 100 ps simulation (at 6000 K)

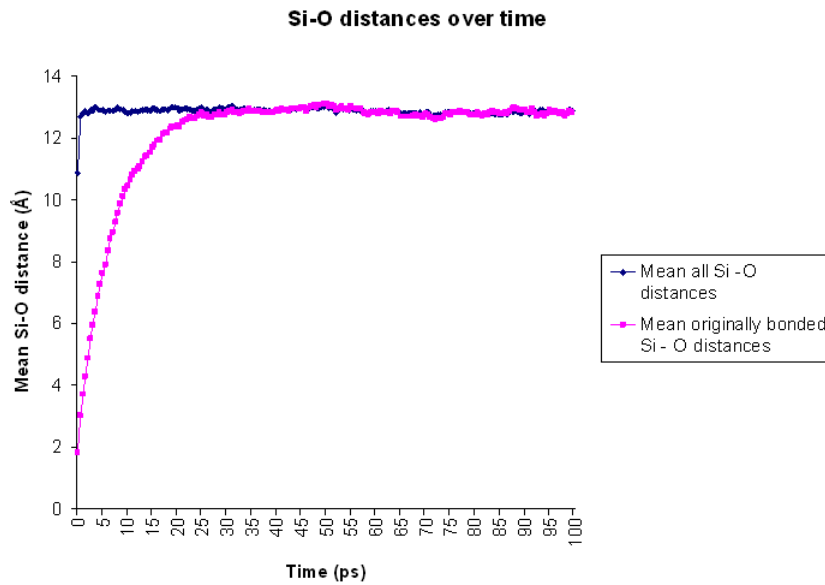


Figure 4.34: Si-O distances for atoms originally bonded against Si-O distances for all atoms in a silica melt with a crystal as the starting structure for a 100 ps simulation (at 6000 K)

It can be seen that in both instances bonded silicon and oxygen atoms become separated very quickly. There does not appear to be a significant cage effect (where an atom is trapped by its surrounding atoms and can only move within them). By the end of the simulation the mean distance between the originally bonded atoms and between all atoms in the structure is the same, showing that no memory of the original Si-O bond remains.

A qualitative illustration of the relative movements of silicon and oxygen atoms in a melt might prove informative. Figure 4.35 shows a typical trajectory of a silicon atom and an oxygen atom for the final 10 ps of a 100 ps simulation. Each point represents the location in space of either the silicon or oxygen atom at a particular point in time. A frame is taken every 100 time steps (every 50 fs, with the time step being 0.5 fs) and a point is shown on the graph every frame. The lighter colours represent the trajectory of the silicon atom and the darker colours represent the trajectory of the oxygen atom. The same colour represents the same time period for the two atoms, with the atoms being differentiated by light and dark so that they can be compared, e.g. light pink represents frames 81-120 for silicon and dark pink represents frames 81-120 for oxygen.

As with the previous figures it can be seen that the atoms become

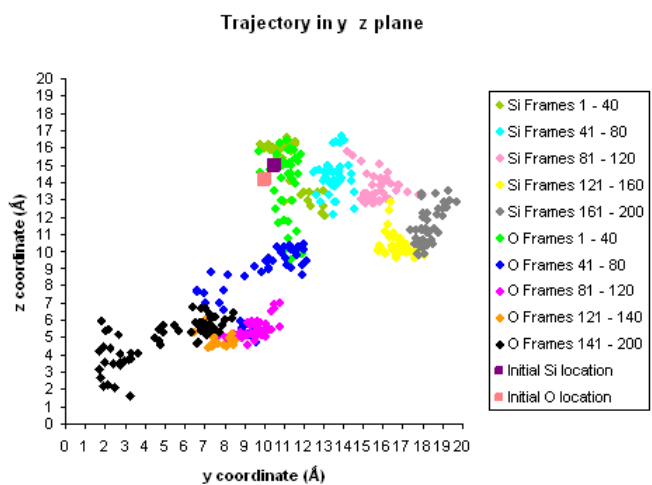
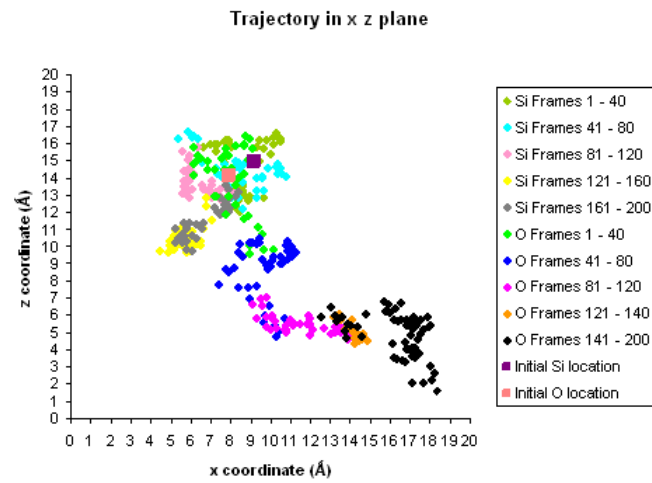
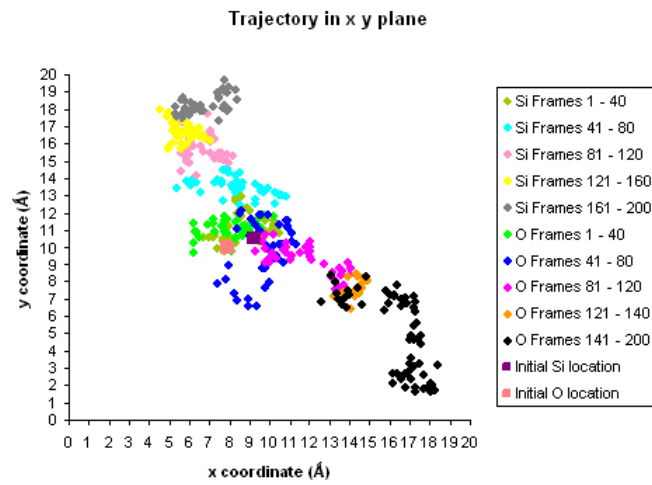


Figure 4.35: Typical trajectories of a silicon and oxygen atom in a melt (at 6000 K)

separated and begin moving independently after a relatively short time.

4.10 Melting a structure using the Sanders potential

A literature search revealed no published papers using a shell model to simulate a silica melt. We therefore investigated the use of the Sanders potential for simulating a silica melt.

The potential was amended to simulate a melt using the same method as for the BKS potential (see [72] and section 4.1 of this chapter). The three body term was removed to allow silicon atoms to have a coordination number different from four.

As with the BKS potential, runs were carried out using a number of different crystal starting structures. The only simulation which ran for a sufficient amount of time without terminating prematurely and at a sufficiently high temperature to produce a melt (judged according to PDFs, the proportion of bonds broken and diffusion coefficients; see below) was one with a starting structure of HP tridymite, with 500 silicon atoms, at a temperature of 4500 K and

with a time step of 0.02 fs. The largest number of time steps possible before the calculation terminated was just over 200,000. The total simulation time was therefore 4 ps (compared to 100 ps using the BKS potential).

Table 4.13 is a frequency table (described in section 4.3 for the BKS potential) which shows the displacement from its starting position at the end of the simulation of every silicon atom individually. We note that only one atom is displaced by less than 10 \AA^2 from its original site, providing some evidence that the structure has melted.

Distance in \AA^2	Number of atoms at that distance
0-10	1
10-20	0
20-30	4
30-40	3
40-50	0
50-100	16
100-300	74
300-500	53
500-700	40
700-900	42
900-1100	45
1100-1300	48
1300-1500	51
1500-1700	42
1700-1900	32
>1900	49
Total	500

Table 4.13: Mean square displacement of each silicon atom for a melt of HP tridymite at 4500 K using the Sanders potential

Table 4.14 contains data on a number of properties of the simulated

structure which are compared with the same starting structure using the BKS potential at 4500 K and 6000 K.

Property	Sanders at 4500 K	BKS at 4500 K	BKS at 6000 K
Diffusion ($10^{-9}m^2$ per second)	9.71	2.76	12.88
Volume per Si atom (\AA^3)	31.83	37.23	38.24
Mean Si-O bond length (\AA)	1.783	1.700	1.741
Mean O-Si-O angle	104.21°	107.54°	107.14°
Mean Si-O-Si angle	120.64°	133.70°	128.52°
Mean coordination	4.81	4.19	4.25

Table 4.14: Properties for a simulation using the Sanders potential with a starting structure of HP tridymite with 500 silicon atoms, compared to the same starting structure using the BKS potential

The magnitude of the diffusion coefficient of the simulation using the Sanders potential at 4500 K (9.71) shows that the system is a liquid. The value is lower than for the BKS simulation at 6000 K (12.88), but much higher than for the BKS simulation at 4500 K (2.76), indicating that the melting temperature of the Sanders potential is lower than that of the BKS potential.

The mean Si-O-Si angle is significantly smaller in the Sanders simulation than in both BKS simulations, which is contrary to what might have been expected: The Sanders potential is a full charge model, with the more highly charged atoms repelling each other to a greater degree than in the BKS potential, which is a partial charge model. It would therefore have been expected that these angles were

straighter in simulations using the Sanders potential.

For the simulation using the Sanders potential the mean bond length is longer and the mean O-Si-O angle is smaller than for either of the structures simulated using the BKS potential. This indicates that there are a larger number of more highly coordinated silicon atoms in the Sanders melt, which is confirmed by the mean coordination being significantly higher than for the BKS structures. A higher coordination would produce a more dense structure. This is confirmed by the volume for the simulation with the Sanders potential being significantly lower than for either of the BKS structures.

The structural properties of simulations of a silica melt using the Sanders potential differ significantly from those using the BKS potential. Little experimental data is available for these properties, so it is not possible to determine at this stage which of the potentials is the most accurate. However, the BKS potential is the more robust of the two, as the majority of simulations at high temperatures using this potential terminated successfully, whereas only one simulation using the Sanders potential ran for a sufficient amount of time to determine properties.

Attempts were made to quench the Sanders melt but these were

unsuccessful.

4.11 Conclusions

1) Structural and dynamic properties of a silica melt and glass that are not available from experimental data have been investigated: Diffusion coefficients at high temperatures (section 4.3), activation energies at high temperatures (section 4.4), the mean and the distribution of bond lengths and angles of a silica melt (section 4.6), the distribution of bond lengths and angles of a vitreous structure (also section 4.6), the mean and distribution of the coordination number in a melt (section 4.7), the distribution of the coordination number in a vitreous structure (also section 4.7), the duration of the Si-O bond in a melt (section 4.9) and the relative movements of silicon and oxygen atoms in a melt (also section 4.9).

2) Given a sufficiently high temperature, the structural and dynamic properties of both a silica melt and glass are independent of the crystal structure from which the melt was produced. This finding has been tested by calculating a number of properties for melts and vitreous structures produced from a number of crystal structures,

including diffusion coefficients (section 4.3), activation energies (section 4.4), energies and volumes, (section 4.5), bond lengths and angles (section 4.6) and coordination numbers (section 4.7). The initial structures included higher pressure polymorphs with higher coordination numbers.

3) Section 4.8 discusses the effect of defects in a crystal on its melting behaviour. It concludes that at high temperatures defects do not significantly affect the crystal's melting behaviour. However, at intermediate temperatures (3500 K to 4500 K for simulated structures) the energy, volume and diffusion coefficients significantly depend on the presence and number of defects.

4) The performance of the BKS potential was assessed for a melt and glass by comparing its output to available experimental data. There was good agreement between the experimental and calculated vibrational density of states (section 4.2). Calculated bond lengths and angles for a vitreous structure are also consistent with experimental data (section 4.6). The calculated mean coordination for a vitreous structure is significantly larger than that of the experimental data (section 4.7). This difference is probably not caused by the potential but is due to the faster quench rate in simulations compared to experiment. The melted structure probably has a higher

coordination than the glass and the structure being quenched does not have sufficient time to relax from the melted structure. The density of a vitreous structure simulated in this thesis was significantly larger than experimental values, although it was consistent with other published simulations (section 4.5). This feature can be attributed to the larger coordination.

5) The performance of the Sanders potential for simulating a melt and glass was assessed. Only one structure ran at a high temperature for a significant enough length of time to produced statistically meaningful results. The melting temperature was lower than for the BKS potential. The volume, mean bond lengths, mean angles and mean coordination for the melt were significantly different from the BKS potential (section 4.10). A quench run using the Sanders potential was not successful.

Chapter 5

The behaviour of amorphous silica under pressure

5.1 Introduction

The preceding chapters have focused on simulations at a range of temperatures but at ambient pressure. This chapter extends the scope of the research to include non-ambient pressures.

Amorphous silica has a wide range of applications (discussed in section 1.1) and is used under a variety of conditions. It is therefore

important to understand its behaviour and durability when exposed to a range of temperatures and pressures. The abundant silicate materials in the interior of the earth and a number of other planets are subjected to very high pressures. A greater understanding of the properties of silica at high pressures and temperatures would provide insight into the factors affecting the geology of these planets.

Neutron diffraction has been used to investigate the structure of amorphous silica at ambient pressure [39] [89], but unfortunately, samples produced at high pressure are often too small for investigation using this method. X-ray diffraction has not been wholly successful in determining the detailed structure of amorphous silica at high pressure [97]. Computational techniques therefore have much to contribute to the understanding of the properties of materials at high pressures.

There are two aims to this chapter. The first is to assess the performance of the BKS potential ([24] and described in section 2.3.2) at elevated pressures and compare its output with available experimental and computational data. The second aim is to use the potential to investigate properties of amorphous silica at high pressure for which experimental and computational data are not available.

5.2 Literature review

This section discusses the experimental and computational literature relating to the application and removal of pressure in amorphous silica. The studies cover a range of temperatures, although the majority have been carried out at ambient temperatures. The experimental studies are generally consistent with each other. However, the computational studies in the literature do not always agree with each other and often disagree both quantitatively and qualitatively with experimental data.

5.2.1 Compression at ambient temperatures

5.2.1.1 Experimental studies

When pressures up to approximately 9 GPa are applied to amorphous silica densification occurs. This behaviour is due to a reversible reduction in Si-O-Si angles, which has been observed in Raman scattering experiments [98] [99].

Between approximately 9 GPa and 20 GPa the densification is not completely reversed when the pressure is released. This behaviour

is due to irreversible changes in the Si-O-Si angles. Neutron diffraction experiments [97] carried out on samples compressed to 16 GPa show a 20% permanent increase in density and a significant decrease in Si-O-Si angles. Brillouin scattering experiments [100] showed a $20\pm 10\%$ permanent increase in density after the application of a pressure of 17.5 GPa. Experiments using Raman scattering [101] find that below approximately 10 GPa the Raman spectra before and after compression are indistinguishable, whereas above this pressure they are different. Experiments by C. H. Polsky, K. H. Smith and G. H. Wolf [102] also use Raman scattering and estimate that the pressure at which densification begins to be irreversible is in the range 8.5 GPa to 10.6 GPa.

At pressures above 20 GPa there is an additional mechanism of densification [103] in addition to the changes in the Si-O-Si angles, which involves the deformation of the tetrahedra, with an increase in coordination number and therefore changes in bond lengths and O-Si-O angles. This additional change is completely reversible and when the pressure is released the coordination, bond lengths and O-Si-O angles return to their original values as before compression, although Si-O-Si angles do not. X-ray diffraction experiments discussed in [104] were carried out at four different pressures: ambient

pressure, 8 GPa, 28 GPa and 42 GPa. There is no significant difference in the modal Si-O distance of 1.57 Å between ambient pressure and 8 GPa. At 28 GPa this distance rises from 1.57 Å to 1.64 Å. At 42 GPa it rises to 1.66 Å. At 42 GPa the modal O-Si-O angle is 96° (for 4 and 6 coordinated silica the ideal O-Si-O angles are 109.5° and 90° respectively) indicating that at this pressure the majority of silica atoms are 6 coordinated.

It is interesting to compare the experimental results indicating that the increase in coordination is completely reversible for amorphous silica with the finding that the 6-coordinated silica crystal structure stishovite (section 1.3.4) can exist at ambient pressure. The stishovite structure has been found in nature at ambient pressure [105] and when synthesised in a laboratory and the pressure removed, the 6-coordinated structure was retained [106].

5.2.1.2 Computational studies

Molecular dynamics (MD) simulations [107] [108] [109] were carried out using a two body potential (the TTAM potential, described in [110]) which, similarly to the BKS potential, was parameterised using ab initio electronic structure calculations but, unlike the BKS

potential, did not include experimental data in its parameterisation. The study does not discuss decompression but finds that from 3 GPa the average coordination number begins to increase (as opposed to 20 GPa according to experiments).

MD simulations [111] using the BKS potential show the average coordination remaining at 4 until 14 GPa, increasing to 5 at 15 GPa and reaching 6 by 20 GPa. This finding is not necessarily inconsistent with experimental results, however, the same paper suggests that the change in density is reversible up to 14 GPa (as opposed to 9 GPa according to experiment).

L. Huang and J. Kieffer [112] carried out MD calculations using a three body potential where both the Si-O-Si and O-Si-O angles were constrained. Si-O-Si angles approaching 180° were made to be energetically unfavourable. O-Si-O angles in a tetrahedral coordination were made to be the most energetically favourable, meaning the probability of any change in coordination number is greatly reduced. Compressions were carried out at pressures between 0 and 20 GPa. It was found that in this pressure range the mean Si-O bond length and mean O-Si-O angle did not change and that the mean Si-O-Si angle decreased with increasing pressure. Although these results are consistent with experiment, they are as would be

expected given the many constraints of the potential. However, although the mean O-Si-O angle did not change, it was found that its distribution became wider with increasing pressure. This is an interesting finding considering that these angles were constrained.

5.2.2 Compression at high temperatures

5.2.2.1 Experimental studies

A number of experimental studies have been carried out on the effect of both high temperatures and pressures on amorphous silica, although the range of temperatures is limited. Experimental studies suggest that the higher the temperature, the greater the amount of permanent densification. They also suggest that the higher the temperature, the lower the pressure at which densification becomes irreversible. Experiments [113] at two different temperatures (475 K and 545 K) provide evidence for the first point. A study by G. D. Mukherjee, S. N. Vaidya and V. Sugandhi [114] finds that at 953 K the pressure at which densification becomes irreversible is 3.6 GPa (compared to approximately 9 GPa at ambient temperature). Raman spectra [115] for glassy silica compressed at 3.95 GPa and 530°C show a significant permanent decrease in volume due to a decrease

in the mean Si-O-Si angle. Experiments [116] also using Raman spectroscopy carried out at 700°C and at pressures up to 8 GPa find permanent densification at pressures as low as 2 GPa. The most significant features are a decrease in Si-O-Si angle, although a lengthening of Si-O bonds is also observed. Raman spectroscopy studies [117] at 5 GPa and 600°C found a decrease in the mean Si-O-Si angle from approximately 144° to approximately 120°.

5.2.2.2 Computational studies

Only one computational study at high temperatures and pressures has been reported: MD simulations carried out by L. Huang and J. Kieffer [118] at 1000 K and 1500 K found that the amount of permanent densification increases with increasing temperature. The potential used for the simulations is not discussed in the paper. If it is the same potential as in the authors' previous work [112] discussed above it will have the O-Si-O and Si-O-Si angle constraint and so may not be appropriate for simulating changes in coordination number.

5.3 Results

This section discusses the results of simulations at a range of temperatures and pressures carried out in two stages: In the first stage a vitreous structure is pressurised at a given pressure and temperature. In the second stage the pressure is released (i.e. the pressure is changed to 0 GPa). For the majority of simulations the temperature is not changed for the second stage. A few of simulations were carried out where the temperature is reduced to ambient temperature in the second stage. These are described in section 5.3.4. It should be noted that in work described in the previous chapter it was found that the vitreous structures produced exhibited a higher density than has been found in experiment, probably due to the faster quench rate (see section 4.5 for details). Therefore, the structures being compressed as discussed in this chapter have an initial density which is higher than in experiment.

The majority of simulations at ambient pressure described in the previous chapter were run for 100 ps. It is possible that with the application and release of pressure the structures require a longer run to reach equilibrium. Longer simulation runs, up to 300 ps for each stage of the application or release process, were carried out in

order to examine the amount of time required for equilibrium to be reached. However, the results showed that 100 ps was a sufficient amount of time to settle fluctuations.

Simulations were run for five different amorphous structures of different supercell sizes and shapes, in order to investigate variability. These structures were generated by melting and quenching five different silica crystal structures with different unit cell shapes and sizes. The results for all the starting structures were similar.

5.3.1 Volume

Figures 5.1 to 5.5 show the resulting volumes per silicon atom of typical simulations at a range of temperatures and pressures. The pink points represent the volume of a single simulation at 0 GPa. The green points represent the volume of a single simulation at the pressure specified in the legend. The blue points represent the resulting volume of a second simulation at 0 GPa using the structure resulting from the simulation represented by the green points as input, i.e. the resulting volume after the pressure specified in the legend has been released.

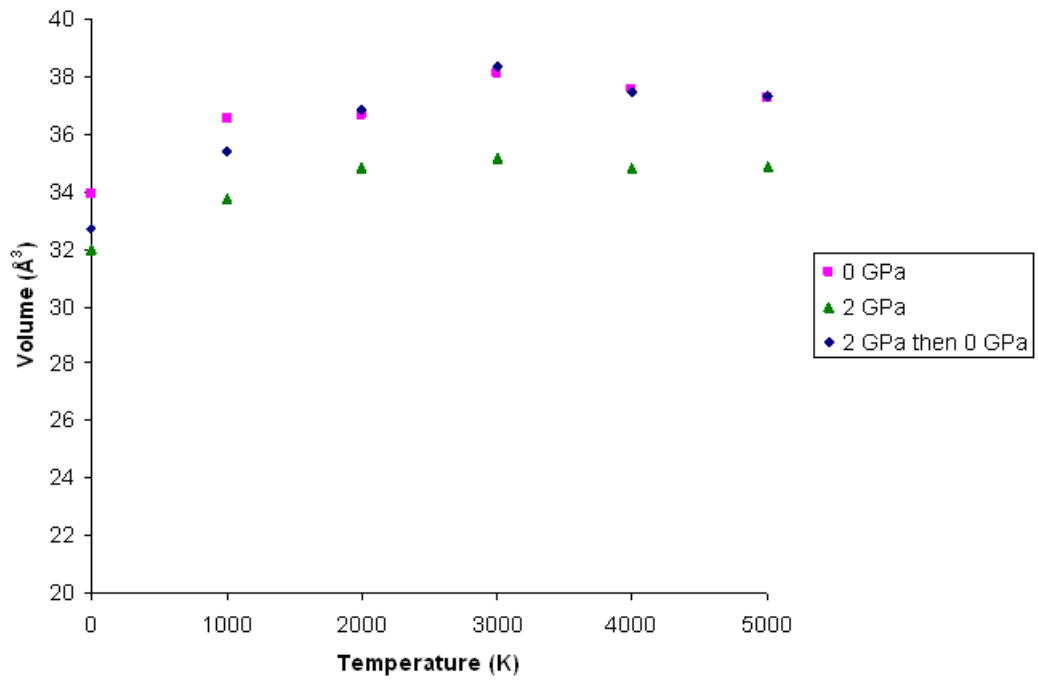


Figure 5.1: Volume resulting from compression of amorphous silica at 2 GPa at a range of temperatures

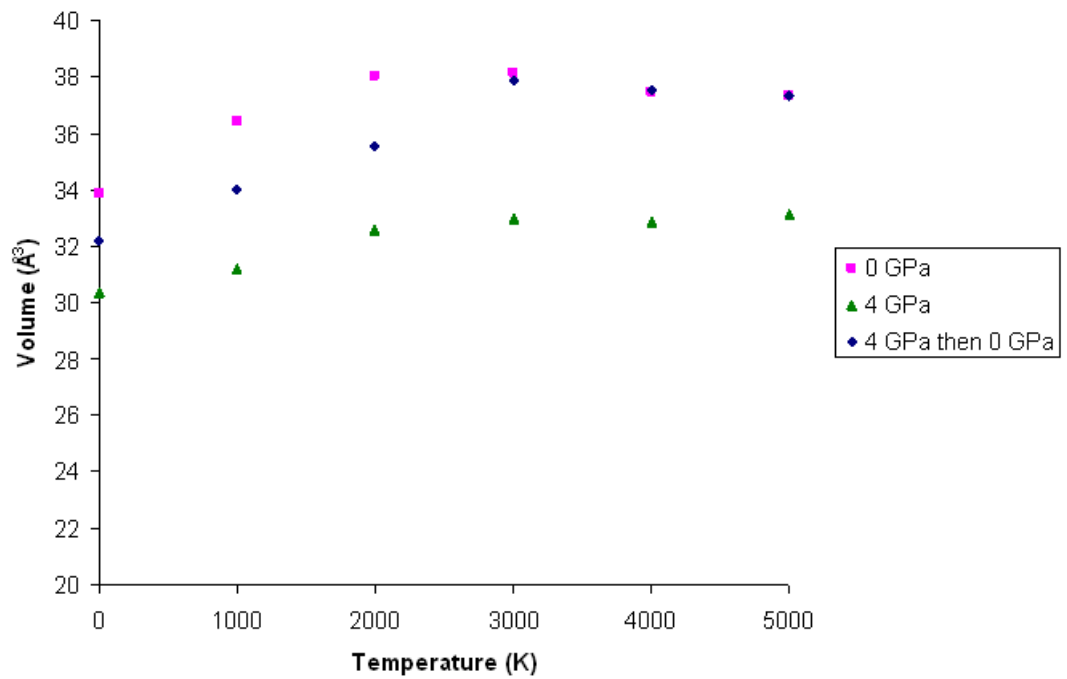


Figure 5.2: Volume resulting from compression of amorphous silica at 4 GPa at a range of temperatures

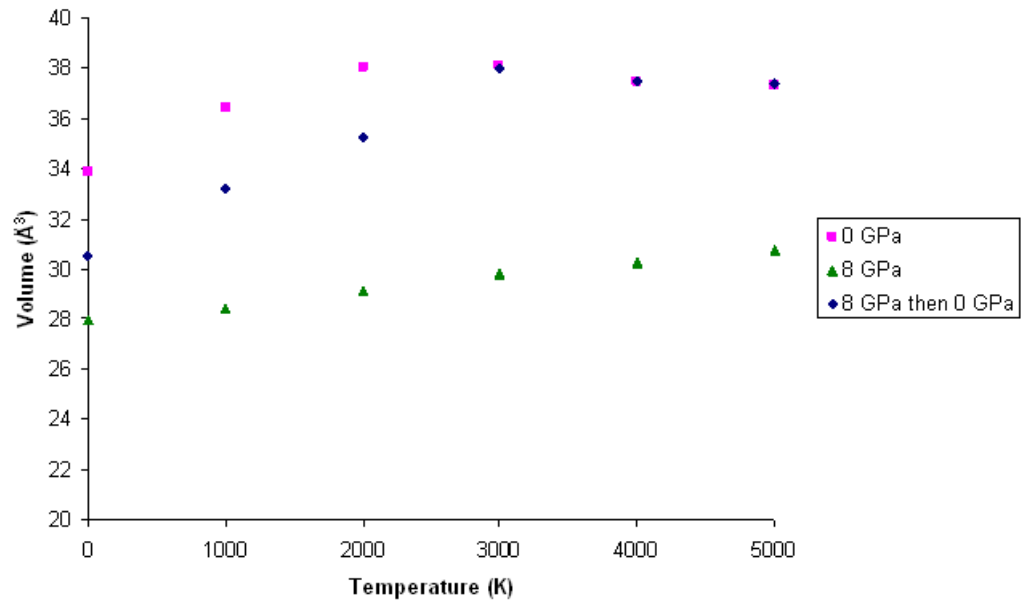


Figure 5.3: Volume resulting from compression of amorphous silica at 8 GPa at a range of temperatures

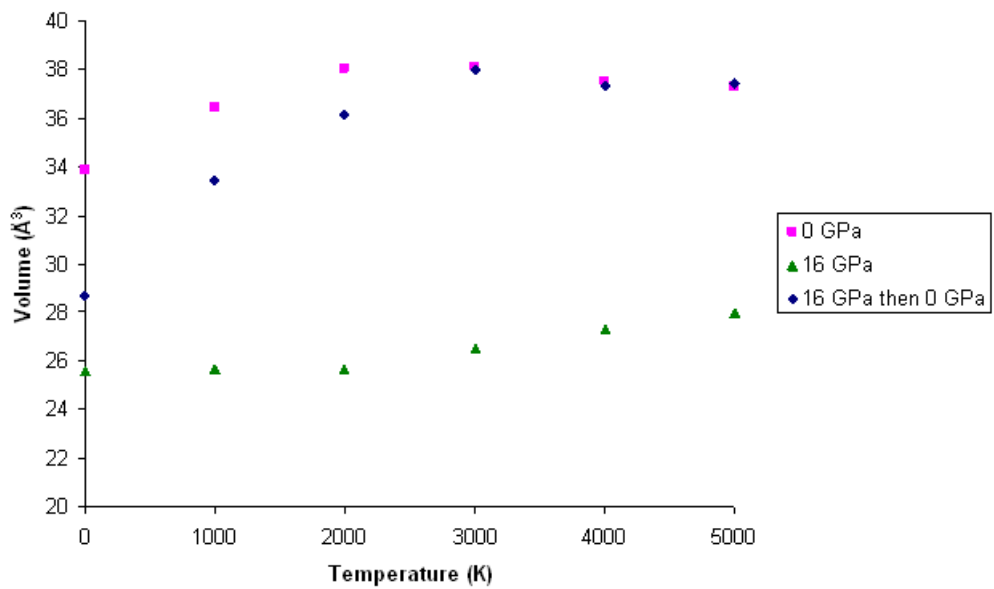


Figure 5.4: Volume resulting from compression of amorphous silica at 16 GPa at a range of temperatures

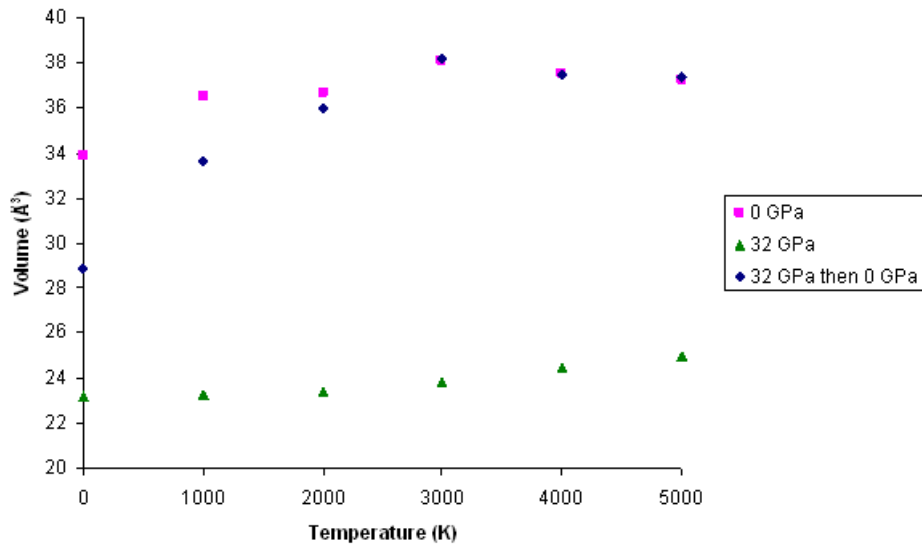


Figure 5.5: Volume resulting from compression of amorphous silica at 32 GPa at a range of temperatures

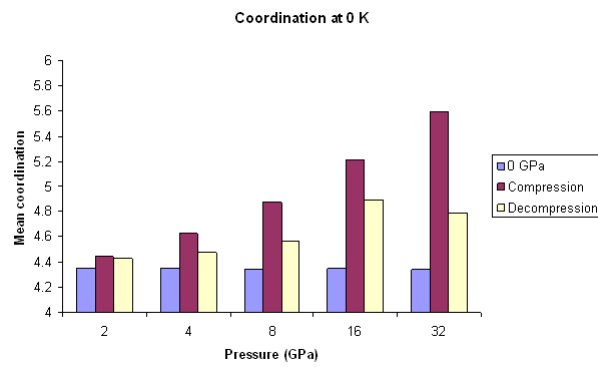
We note that for simulations at high temperatures the original volume is recovered after decompression, regardless of pressure. These results contradict the experiments discussed in section 5.2.2 which find that the higher the temperature, the greater the amount of permanent densification.

The figures show that at low temperatures, for all pressures, the volume before compression is not recovered after decompression. These results again do not agree with experimental findings, which are that the volume change is reversible up to 9 GPa. It is interesting to note that the melting temperature in a simulation is much higher than in experiment: approximately 6000 K with the BKS potential, compared to 1986 K [37, p. 9] for experiment. The differences

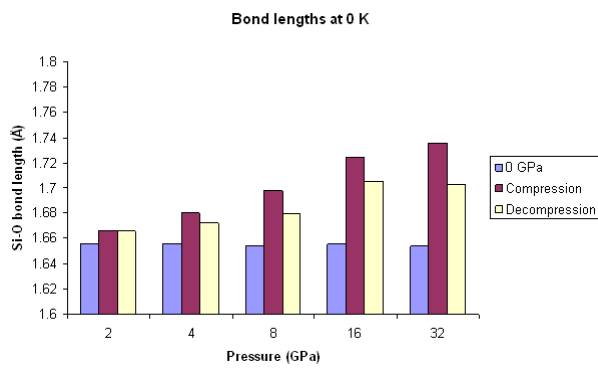
between calculations and experiment for both the behaviour under pressure and the melting point might be due to a similar mechanism. An explanation could be that the energy barriers in the potential might be higher than those in experiment, so at low temperatures the atoms cannot overcome these barriers and therefore get caught in meta-stable energy minima. Additionally, experimental materials will have defects, which were not included in simulations in this chapter. However, work described in section 4.8 indicates that the presence of defects significantly lowers the melting point of a silica crystal. It is possible that the presence of defects might affect the behaviour of silica under pressure, which could be an interesting area for further work.

5.3.2 Coordination, bond lengths and angles

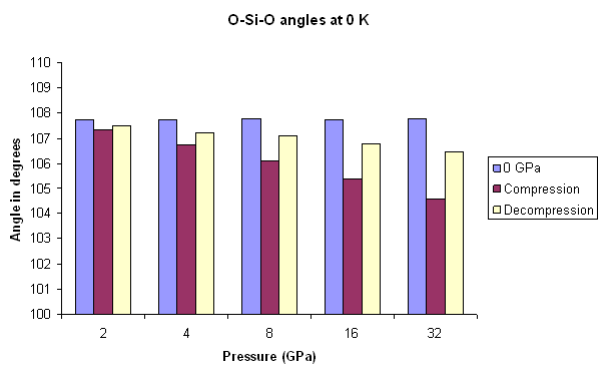
Figures 5.6 and 5.7 contain results for mean coordination, bond lengths and angles for simulations at 0 K and 4000 K respectively. The mauve bars show values for simulations at 0 GPa. The pink bars show values for simulations at pressures displayed on the x-axis. The cream bars show values for simulations at 0 GPa following a simulation at the pressure displayed on the x-axis.



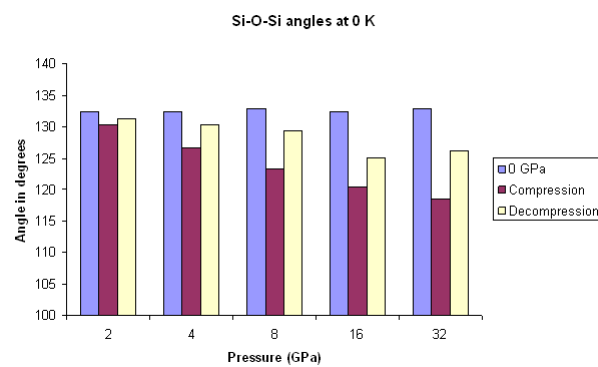
(a) Coordination



(b) Si-O bond lengths

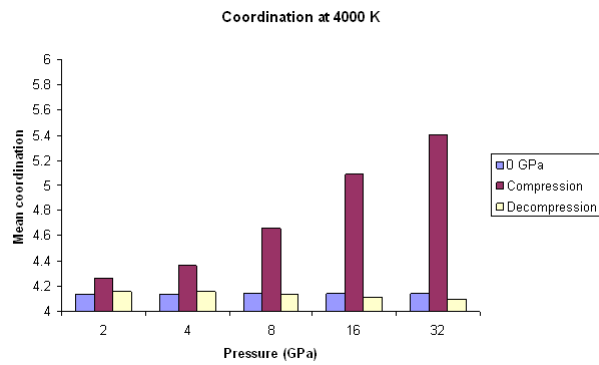


(c) O-Si-O angles

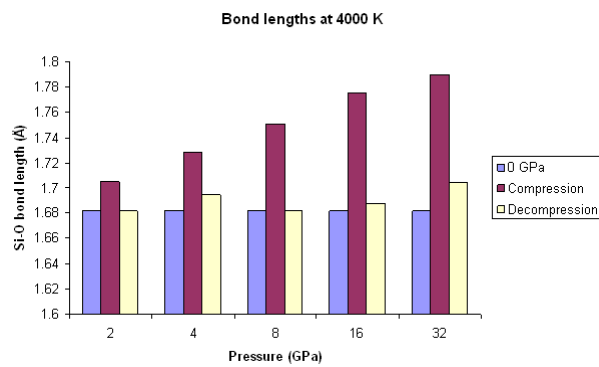


(d) Si-O-Si angles

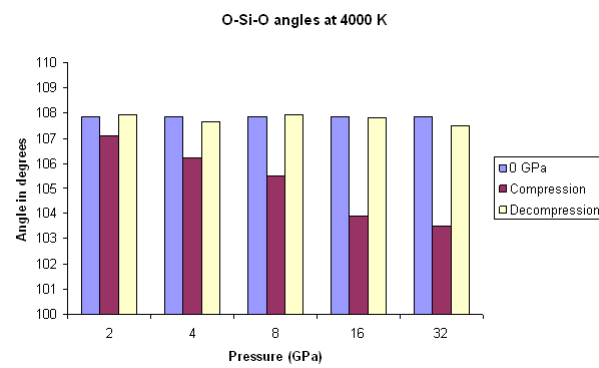
Figure 5.6: Mean coordination, bond lengths, O-Si-O angles and Si-O-Si angles at 0 K



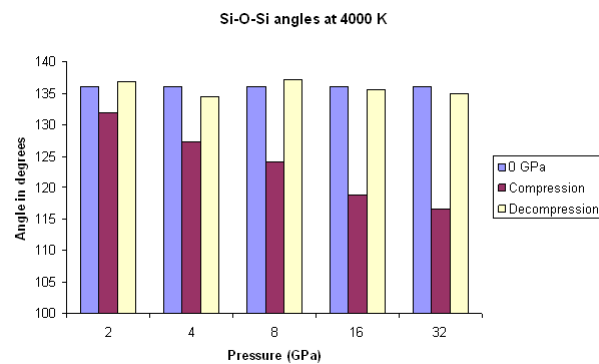
(a) Coordination



(b) Si-O bond lengths



(c) O-Si-O angles



(d) Si-O-Si angles

Figure 5.7: Mean coordination, bond lengths, O-Si-O angles and Si-O-Si angles at 4000 K

We first discuss simulations at 0 K. During compression, as would be expected, Si-O-Si angles decrease with increasing pressure at all pressures. However, there are no pressures at which Si-O-Si angles recover completely upon decompression. This result contradicts experimental data (section 5.2.1.1) which find permanent changes in these values only at pressures of 9 GPa and above. Coordination, bond lengths and O-Si-O angles also change upon compression at all pressures. These results do not agree with experimental data which find that these values are only affected by compression at pressures above 20 GPa. Additionally, experiments show that, regardless of pressure, these values completely recover after decompression, contradicting the results shown in the figure.

The figures show that at all pressures at 4000 K there are significant changes in coordination, bond lengths, O-Si-O angles and Si-O-Si angles upon compression. No previous experimental or computational studies were found relating to changes in tetrahedra at high temperatures. The figures also show that there is no significant difference between values for these properties at 0 GPa and after decompression. This result does not agree with experiments discussed in section 5.2.2.1, which cites two studies at high temperatures that found a permanent decrease in Si-O-Si angle, even at low pressures.

5.3.3 Gradual application and release of pressure

The results described so far relate to simulations where a change in pressure has been immediate. Pressure changes which were gradual rather than immediate would be more representative of experimental conditions. Simulations were carried out where both application and release of pressure were gradual. The simulations with gradual compression were carried out by running for 200,000 steps with a time step of 0.5 fs (totalling 100 ps) at 0 GPa then increasing the pressure by a small amount and running for a further 200,000 steps. This process was repeated until the required pressure was reached. The simulations of gradual decompression were carried out similarly but in reverse. Two different compression/decompression rates were used: the change in pressure between each stage was either 0.5 GPa or 1.0 GPa.

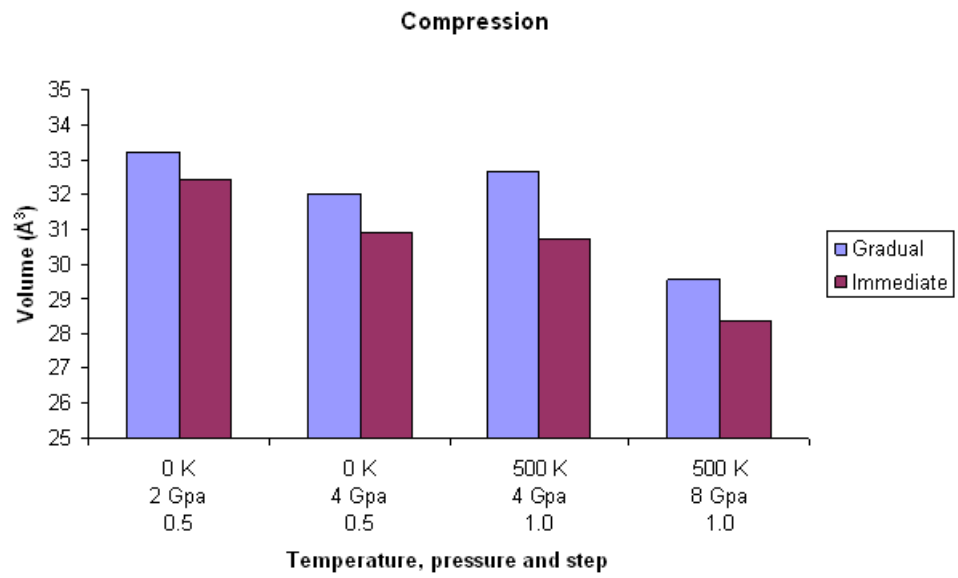
Figure 5.8 compares volumes for gradual and immediate compression/decompression. The first line of the x-axis labels gives the temperature of the simulation. The second line for the compression graph shows the pressure to which the structure was compressed and for the decompression graph shows the pressure from which the structure was decompressed. The third line gives the difference

in pressure or step (in GPa) between each stage of the compression/decompression. As described in previous sections, simulations with five different starting structures were carried out in order to investigate variability. The results for all the starting structures were similar and the values in the figure represent the mean values of the different starting structures.

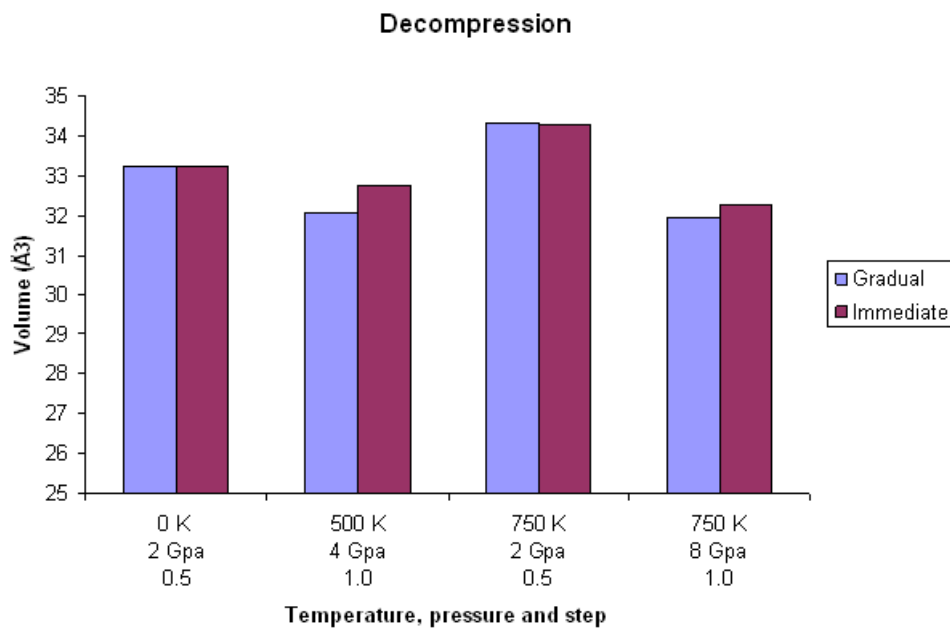
The graphs for decompression show no discernible difference in volume between immediate and gradual decompression where the step is 0.5 GPa. There is a small difference between immediate decompression and gradual decompression where the step is 1.0 GPa.

In the case of compression, however, in all cases the volume for gradual compression is significantly higher than for immediate compression. In order to investigate the reasons for this difference, the coordination, bond lengths and angles of the two types of simulation were compared and are shown in Figure 5.9.

The figure shows that there is a higher coordination for immediate compression when compared to gradual compression, which is confirmed by the larger O-Si-O angles. The bond lengths are longer in order to accommodate the higher coordination. The Si-O-Si angles are smaller for immediate application of pressure than for gradual

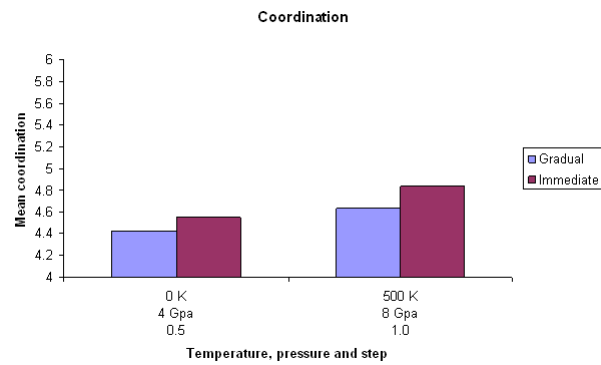


(a) Compression

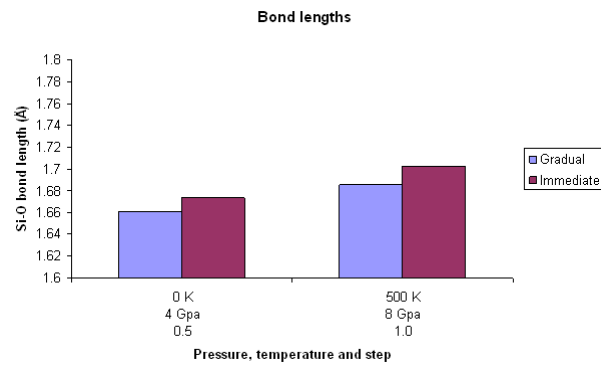


(b) Decompression

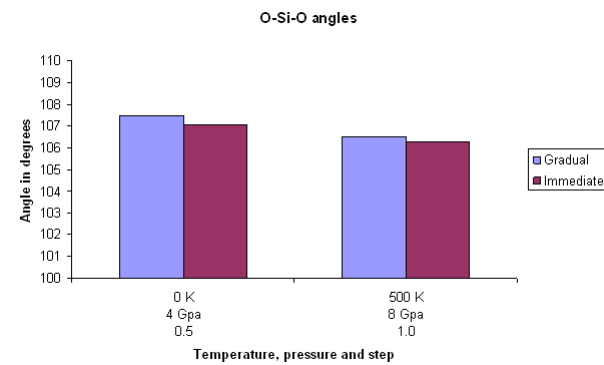
Figure 5.8: A comparison of the mean resulting volumes of simulations with gradual and immediate changes in pressure



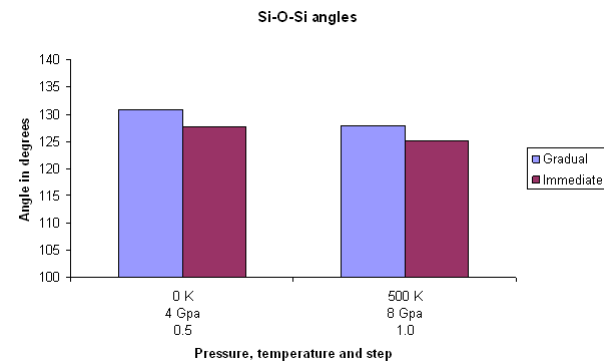
(a) Coordination



(b) Si-O bond lengths



(c) O-Si-O angles



(d) Si-O-Si angles

Figure 5.9: Comparing mean coordination, bond lengths, O-Si-O angles and Si-O-Si angles for simulations with gradual and immediate compression

application. The smaller volume observed with immediate application of pressure (Figure 5.8) is therefore due to both the higher coordination and smaller Si-O-Si angles.

The differences between immediate and gradual compression were further analysed by constructing a frequency table showing the displacement of every silicon atom, comparing its location at the beginning and end of the simulation. Table 5.1 shows such a table for all silicon atoms comparing immediate and gradual compression to 8 GPa at 500 K. Immediate decompression from 8 GPa at 500 K is also shown for comparison.

The table shows that there is a marked difference in the displacement of the atoms between immediate and gradual compression. There is more displacement with gradual compression, indicating that a large number of bonds might be broken. An explanation for this difference might be that on immediate compression the height of the energy barriers increases by a large amount quite suddenly, meaning that the new atomic configuration must have energy minima which are very close to those of the initial structure, due to the atoms finding it difficult to overcome a large number of high energy barriers. When the structure is compressed gradually it has a longer time to explore a phase space which has lower energy barriers and

Distance in \AA^2	Number of atoms at that distance		
	Immediate compression	Gradual compression	Immediate decompression
0.0-0.2	16	0	176
0.2-0.4	25	6	102
0.4-0.6	34	16	67
0.6-0.8	29	35	40
0.8-1.0	26	44	24
1.0-1.2	30	64	18
1.2-1.4	20	38	18
1.4-1.6	32	49	13
1.6-1.8	28	32	11
1.8-2.0	16	33	10
2.0-2.2	12	21	6
2.2-2.4	18	22	3
2.4-2.6	20	21	2
2.6-2.8	13	17	2
2.8-3.0	13	27	2
>3.0	168	75	6
Total	500	500	500

Table 5.1: Displacement of each silicon atom for decompression from/compression to 8 GPa at 500 K

Number of Si atoms	Temperature (K)	Pressure (GPa)	Energy (eV) per Si atom for gradual compression	Energy (eV) per Si atom for immediate compression
500	0	4	-57.780	-57.710
512	0	4	-57.777	-57.730
500	500	8	-57.512	-57.462
512	500	8	-57.469	-57.445

Table 5.2: A comparison of final energies in eV for gradual and immediate compression

can therefore find a more energetically favourable configuration. Table 5.2 shows that it is indeed the case that structures pressurised by gradual compression have a lower energy than those that have been compressed immediately.

This finding might explain the data in Figure 5.9, with the lower coordination and larger Si-O-Si angles indicating that a more energetically favourable structure has been found on gradual application of pressure.

5.3.4 The release of both high pressures and temperatures

A number of simulations were carried out where the pressure was removed and the temperature lowered to ambient levels simultaneously. No literature on these type of experiments or simulations was found. Figure 5.10 shows an example of the resulting volumes of such a simulation. The pressure of each first run was 8 GPa, at the temperature specified on the x-axis. The pressure was then released to 0 GPa with the temperature also being lowered to 300 K.

For all simulations there is a large difference between the volumes of structures at 0 GPa and the decompressed structures. This behaviour possibly illustrates the point discussed in section 5.3.1:

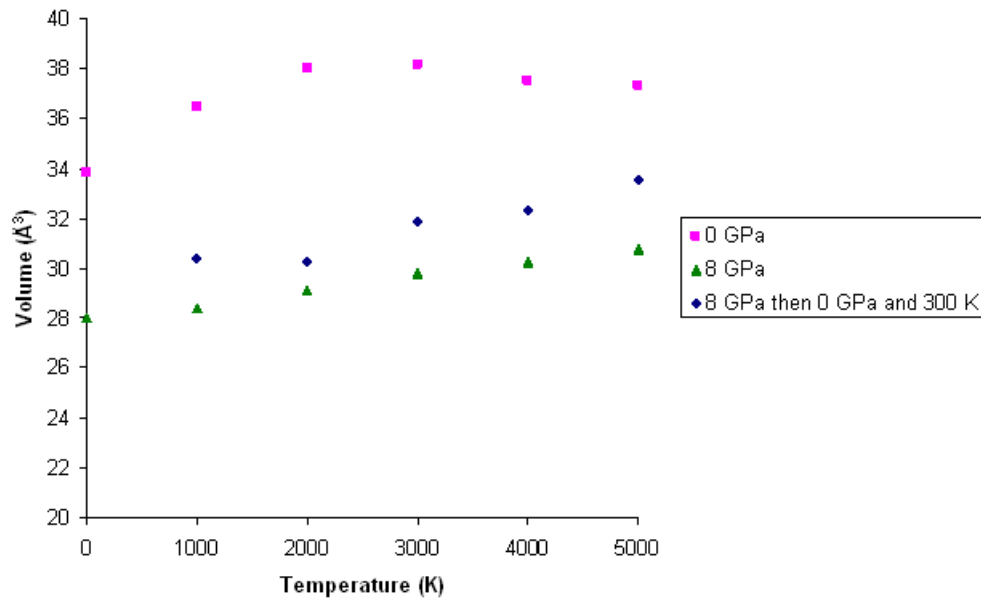


Figure 5.10: Volume for simulations where both temperature and pressure are lowered

When the temperature is low the particles cannot move with a sufficiently high force to overcome the energy barriers and therefore remain in meta-stable energy minima. These results are probably due to the parameters of the potential and the fast cooling rate and may not be representative of experimental results.

5.4 Summary and conclusions

5.4.1 Summary

This chapter describes simulations of the compression and decompression of amorphous silica at a range of temperatures and pres-

tures.

At low temperatures, upon compression at any pressure the simulations result in structures where there are significant changes in volume, coordination, bond lengths, O-Si-O angles and Si-O-Si angles. These results do not agree with experimental results which find that tetrahedra only begin to become deformed above 20 GPa (section 5.2.1.1). The results are similar to a number of computational studies discussed in section 5.2.1.2 in finding changes in all values at low pressures, but differ from two of the studies which are more consistent with experiment.

Upon decompression at low temperatures, results of simulations presented here find that the original volume, coordination, bond lengths, O-Si-O angles and Si-O-Si angles are not recovered at any pressure. These findings also disagree with experimental data which find that deformations of tetrahedra due to any pressure are always recovered upon decompression and that the original volume and Si-O-Si angles are recovered at pressures up to 9 GPa.

Simulations of compression at high temperatures resulted in significant changes in volume, coordination, bond lengths, O-Si-O angles and Si-O-Si angles at all pressures. No experimental data were found

investigating deformation of tetrahedra, but experiments show that volume and Si-O-Si angles are reduced upon compression.

On decompression at high temperatures simulations result in complete recovery of volume, coordination, bond lengths, O-Si-O angles and Si-O-Si angles at all pressures. In contrast to the findings described here, experimental data show that the higher the temperature, the lower the pressure at which changes in the above values are not recovered upon decompression. The single computational study at high temperatures that was found agrees with the experimental results, although the tetrahedra were constrained by the potential used.

It was found that the volume of a system compressed gradually differed significantly from the volume of a system undergoing immediate compression, which was due to differences in coordination, bond lengths, O-Si-O angles and Si-O-Si angles. This difference in volume was not observed between gradual and immediate decompression.

5.4.2 Conclusions

There are significant quantitative and qualitative differences between results of simulations discussed in this thesis and the experi-

mental literature.

The deformation of tetrahedra upon compression at pressures much lower than in experiment might be due to the nature and parameterisation of the potential. The O-Si-O angles of amorphous silica from simulations using the BKS potential may not be sufficiently rigid under pressure.

For all pressures, at low temperatures, none of the structural parameters (volume, coordination, bond lengths, O-Si-O angles and Si-O-Si angles) are recovered after decompression, whereas at high temperatures they are recovered completely. Neither of these findings agree with experimental data which find that different characteristics are recoverable at different pressures. The most likely explanation for this behaviour is that the potential is constructed such that at low temperatures the atoms get caught in meta-stable energy minima, with possibly higher energy barriers than in experiment, and do not have sufficient energy to explore the phase space and find a more energetically favourable structure. In contrast, at high temperatures the atoms are possibly able to explore a larger area of phase space and can therefore find a more optimal structure than in experiment.

Chapter 6

Summary and future work

6.1 Summary

The techniques of free energy minimisation, molecular dynamics (MD) and Density Functional Theory were used to simulate a number of different tridymite starting structures at a range of temperatures. It was found that the interatomic potential and simulation technique used were the main factors affecting the resulting structure. The temperature of the simulation and the initial structure did not generally affect the final atomic configuration or volume and the initial structure did not affect the final energy. Of the two interatomic potentials used, the Sanders potential (section 2.3.3

and [25]) reproduced experimental volumes more accurately than the BKS potential (sections 2.3.2 and [24]). Additionally, the final atomic configurations from MD simulations using the Sanders potential were similar to a tridymite structure that has been found in nature, in contrast to the those from the BKS potential, which were not similar to any of the known structures. These results may be due to a number of possible reasons: Firstly, the transitions between the various tridymite structures require only changes in Si-O-Si angles (displacive transitions) with no breaking or forming of bonds (reconstructive transitions). The energy landscape of tridymite is therefore very flat and the techniques and potentials used may not be sensitive enough to deal with this. Another possible reason is that the potentials have been parameterised to distinguish between structures which have reconstructive transitions and these parameters may not be able to simulate displacive transitions as is the case with tridymite. Finally, if the structures which have been found in nature are meta-stable and/or poorly characterised, it might be difficult for the simulation techniques to find their atomic configurations.

Properties of silica melts and glasses that are not available from experiment were investigated using MD simulations with the BKS po-

tential. This method was also used for calculating properties which are available from experiment in order to assess the performance of the potential. The properties investigated were the mean square displacement, autocorrelation functions, pair distribution functions, energy, volume, the extent to which silicon and oxygen atoms move together, Arrhenius plots, coordination number, bond lengths and angles. It was found that the density and coordination are significantly higher than in experiment. This result is not, however, attributed to the potential, but to the higher quench rate in computational studies than an experiment. Additionally, a range of different silica crystals (including both high temperature and high pressure forms) were melted and a number of properties of these melts were investigated. It was found that at sufficiently high temperatures the melts are all similar and that the starting structure does not affect the properties of the melt. Investigations were also carried out to see whether it is possible to use the Sanders potential to simulate a silica melt. Various properties of such a melt were calculated, which were found to be significantly different to those calculated using the BKS potential.

There is little experimental data available on the behaviour of amorphous silica at both high temperatures and pressures. MD with the

BKS potential was used to explore the properties of amorphous silica at elevated pressures and a range of temperatures. Calculations at low temperatures show that when compressed to any pressure, all properties (volume, coordination, bond lengths, O-Si-O angles and Si-O-Si angles) of the structure are affected, in contrast to experimental results which show that tetrahedra do not become deformed until pressures above 20 GPa. Upon decompression the original values of the calculated properties are not recovered, whereas experimental results find complete recovery of the distortion of the tetrahedra on decompression from any pressure. Calculations at high temperatures result in all properties of the initial structure before compression being recovered, which contrasts with experimental findings which show that the higher the temperature, the lower the pressure at which the original properties are not recovered.

Computer simulation techniques are a powerful tool for investigating a range of structural and dynamic properties. In this work we have gained insight into the capabilities and limitations of a number of techniques and potentials and have also learned much about the properties of liquid, glassy and crystalline silica.

6.2 Future work

The research on the tridymite polymorph, discussed in chapter 3, could be extended by carrying out further electronic structure calculations. The chapter describes the results of Density Functional Theory calculations on silica clusters terminated by hydrogen atoms. Calculations using periodic boundary conditions are often more accurate than those using clusters and therefore calculations using this method may be a worthwhile route to pursue.

Chapter 4 describes molecular dynamics simulations to calculate various static and dynamic properties of pure silica. An interesting area for further work might be to explore the extent to which these properties differ when impurities are added.

It was found that the density of vitreous silica produced computationally differs significantly from that of experiment. This difference is most probably due to the computational quench rate being several orders of magnitude faster than in experiment. In order to confirm whether this is the correct explanation, computational simulations with much slower quench rates than is standard could be carried out.

In chapter 5 it was found that the results of simulations at high pressures using the BKS potential did not generally agree with experimental results. This potential was parameterised for modelling silica structures at ambient pressure. A further area of work could be to reparameterise the potential so that it more accurately reproduces experimental results at high pressures.

Bibliography

- [1] M. H. Battey and A. Pring. *Mineralogy for students*. Addison Wesley Longman Ltd., 3rd edition, 1997.
- [2] H. R. Wenk and A. Bulakh. *Minerals*. Minerals Cambridge University Press, 2003.
- [3] C. Klein and C. S. Hurlbut Jr. *Manual of mineralogy*. John Wiley and Sons, 21st edition, 1999.
- [4] Chemical Database Service. Chemical database service website. <https://cds.dl.ac.uk/>.
- [5] D. Cellai, M. A. Carpenter, R. J. Kirkpatrick, E. K. H. Salje, and M. Zhang. Thermally induced phase transitions in tridymite: an infrared spectroscopy study. *Phys. Chem. Min.*, 22:50–60, 1994.

- [6] N. R. Keskar and J. R. Chelikowsky. Structural properties of nine silica polymorphs. *Phys. Rev. B*, 46:1, 1992.
- [7] P. J. Heaney. Structure and chemistry of the low pressure silica polymorphs. *Rev. Min.*, 29:20, 1994.
- [8] A. K. A. Pryde and M. T. Dove. On the sequence of phase transitions in tridymite. *Phys. Chem. Min.*, 26:171, 1998.
- [9] K. Kihara. Disorder and successive structure transitions in the tridymite forms of silica. *Phys. Chem. Min.*, 22:223–232, 1995.
- [10] A. Nukui, A. Yamamoto, and H. Nakazawa. Non-integral phase in tridymite. In J. M. Cowley, J. B. Cohen, M. B. Salamon, and B. J. Wuensch, editors, *Am. Inst. Phys. AIP*, volume 53, pages 327–329, 1979.
- [11] H. Graetsch. X-ray powder diffraction study on the modulated high-temperature forms of SiO₂ tridymite between 110°C and 220°C. *Phys. Chem. Min.*, 28:313–321, 2001.
- [12] W. A. Dollase. The crystal structure at 220°C of orthorhombic high tridymite from the steinbach meteorite. *Acta. Cryst.*, 23:617, 1967.

- [13] T. Hirose, K. Kihara, M. Okuno, S. Fujinami, and K. Shinoda. X-ray, DTA and raman studies of monoclinic tridymite and its higher temperature orthorhombic modification with varying temperature. *J. Min. and Pet. Sci.*, 100:55, 2005.
- [14] S. J. Kitchin, S. C. Kohn, R. Dupree, C. M. B. Henderson, and K. Kihara. In situ ^{29}Si MAS NMR studies of structural phase transitions of tridymite. *Amer. Min.*, 81:550–560, 1996.
- [15] W. H. Baur. Silicon-oxygen bond lengths, bridging angles Si-O-Si and synthetic low tridymite. *Acta. Cryst.*, B33:2615–2619, 1977.
- [16] W. A. Dollase and W. H. Baur. The superstructure of meteoritic low tridymite solved by computer simulation. *Amer. Min.*, 61:971–978, 1976.
- [17] K. Kato and A. Nukui. Die kristallstruktur des monoklinen Tief-Tridymits. *Acta. Cryst.*, B 32:2486–2491, 1976.
- [18] E. A. Smelik and R. R. Reeber. A study of the thermal behaviour of terrestrial tridymite by continuous x-ray diffraction. *Phys. Chem. Min.*, 17:196–206, 1990.
- [19] H. Graetsch. Characterization of the high-temperature modifications of incommensurate tridymite L3-T0 (MX-1) from 25°C

- to 250°C. *Amer. Min.*, 83:872–880, 1998.
- [20] R. I. Withers, J. G. Thompson, Y. Xiao, and R. J. Kirkpatrick. An electron diffraction study of the polymorphs of silica-tridymite. *Phys. Chem Min.*, 21:421–433, 1994.
- [21] M. A. Carpenter and M. Wennemer. Characterisation of synthetic tridymites by transmission electron microscopy. *Amer. Min.*, 70:517–528, 1985.
- [22] S. P. Gardner and D. E. Appleman. X-ray crystallography and polytypism of naturally-occurring tridymite, SiO₂. *Am. Cryst. Ass. Prog. and Abst.*, 2, 1974.
- [23] J. H. Kohnert and Appleman. The crystal structures of low tridymite. *Acta. Cryst.*, B34:391–403, 1978.
- [24] B. W. H. van Beest, G. J. Kramer, and R. A. van Santen. Force fields for silicas and aluminophosphates based on ab initio calculations. *Phys. Rev. Lett.*, 64:1955, 1990.
- [25] M. J. Sanders, M. Leslie, and C. R. A. Catlow. Interatomic potentials for SiO₂. *J. Chem. Soc.*, 1271, 1984.
- [26] J. Brady. Silica phase diagram.
<http://serc.carleton.edu/images/research-education/equilibria/silica-minerals-stability.jpg>.

- [27] J. L. Holm, O. J. Kleppa, and E. F. Westrum Jr. Thermodynamics of polymorphic transformation in silica. Thermal properties from 5 to 1070 K and pressure-temperature stability fields for coesite and stishovite. *Geochimica et Cosmochimica Acta*, 31:2289–2307, 1967.
- [28] V. B. Prokopenko, L. S. Dubrovinsky, V. Dmitriev, and H.-P. Weber. In situ characterization of phase transitions in cristobalite under high pressure by raman spectroscopy and x-ray diffraction. *J. Alloys and Compounds*, 327:87–95, 2001.
- [29] K. J. Kingma, R. E. Cohen, R. J. Hemley, and H-K Mao. Transformation of stishovite to a denser phase at lower-mantle pressures. *Letters to Nature*, 374:243–245, 1995.
- [30] R. J. Hemley, J. Badro, and D. M. Teter. Polymorphism in crystalline and amorphous silica at high pressures. In *Physics meets mineralogy*. Cambridge University press, 2000.
- [31] J. E. Shelby. *Introduction to glass science and technology*. The Royal Society of Chemistry, 2nd edition, 2005.
- [32] F. L. Galeener. Current models for amorphous SiO₂. In *The Physics and Technology of Amorphous SiO₂*. Plenum Press, 1988.

- [33] W. H. Zachariasen. The atomic arrangement in glass. *J. Amer. Cer. Soc.*, 54(3841), 1932.
- [34] G. N. Greaves and S. Sen. Inorganic glasses, glass-forming liquids and amorphizing solids. *Advances in Physics*, 56:1–166, 2007.
- [35] P. H. Gaskell. Structure and properties of glasses - how far do we need to go? *J. Non. Crys. Sol.*, 222:1–12, 1997.
- [36] R. H. Doremus. *Glass Science*. John Wiley and Sons, 2nd edition, 1994.
- [37] G. O. Jones. *Glass*. Chapman and Hall Ltd, 1971.
- [38] N. N. Greenwood and A. Earnshaw. *Chemistry of the elements*. Butterworth - Heinemann, 2nd edition, 2001.
- [39] A. C. Wright. Neutron scattering from vitreous silica. V. the structure of vitreous silica: What have we learned from 60 years of diffraction studies? *J. Non. Crys. Sol.*, 179:84, 1994.
- [40] E. Dupree and R. F Pettifer. Determination of the Si-O-Si bond angle distribution in vitreous silica by magic angle spinning NMR. 308:523, 1984.
- [41] G. N. Greaves. EXAFS and the structure of glass. *J. Non. Crys. Sol.*, 71:203–217, 1985.

- [42] J. D. Gale and A. L. Rohl. The general utility lattice program (GULP). *Molecular Simulation*, 29:291–341, 2003.
- [43] A. Putnis. *Introduction to mineral sciences*. Cambridge University press, 1992.
- [44] M. T. Dove. *Introduction to Lattice Dynamics*. Cambridge University press, 1993.
- [45] M. Born and K. Huang. *Dynamical Theory of Crystal Lattices*. Oxford University Press, 1954.
- [46] C. Kittel. *Introduction to solid state physics*, volume 5. John Wiley and Sons, 1976.
- [47] A. R. Leach. *Molecular modelling: principles and applications*. Pearson Education Ltd, 2nd edition, 2001.
- [48] M. B Taylor, G. D. Barrera, N. L. Allan, and T. H. K. Barron. Free energy derivatives and structure optimisation within quasiharmonic lattice dynamics. *Phys. Rev. B*, 56(22):380–390, 1997.
- [49] W. Smith, T. R. Forester, and I. T. Todorov. The DL_POLY_2.0 user manual, 2008.
- [50] D. Frenkel and B. Smit. *Understanding Molecular Simulation*. Academic Press, 2002.

- [51] I Saika-Voivod, F. Sciortino, and P. H. Poole. Free energy and configurational entropy of liquid silica: Fragile-to-strong crossover and polyamorphism. *Phys. Rev. E*, 69(4):041503.
- [52] J. Horbach, W. Kob, and K. Binder. Molecular dynamics computer simulation of the dynamics of supercooled silica. *J. Phys. Condens. Matter*, 1, 1997.
- [53] J. S. Tse and D. D. Klug. Mechanical instability of alpha-quartz: a molecular dynamics study. *Phys. Rev. Lett.*, 67(25), 1991.
- [54] A. Tilocca, N. de Leeuw, and A. N. Cormack. Shell model molecular dynamics calculations of modified silicate glasses. *Phys. Rev. B*, 73:10429, 2006.
- [55] A. Kerrache, V. Teboul, and A. Monteil. Screening dependence of the dynamical and structural properties of BKS silica. *J. Chem. Phys.*, 321:69, 2005.
- [56] K. Binder, J. Horbach, H. Knoth, and P. Pfliderer. Computer simulation of molten silica and related glass forming fluids: recent progress. *J. Phys. Condens. Matter*, 19:205102, 2009.
- [57] K. Muralidharan, J. H. Simmons, P. A. Deymier, and K. Runge. Molecular dynamics studies of brittle fracture in

- amorphous silica: Review and recent progress. *J. Non. Cryst. Sol.*, 351:1532–1542, 2005.
- [58] P. Jund and R. Jullien. The glass transition in a model silica glass: evolution of the local structure. *Philosophical Magazine A.*, 79(1):223–236, 1999.
- [59] X. Yuan and A. N. Cormack. Si-O-Si bond angle and torsion angle distribution in vitreous silica and sodium silicate glasses. *J. Non. Cryst. Solids*, 319:31, 2003.
- [60] L. Pauling. The nature of silicon-oxygen bonds. *Amer. Min.*, 65:321–323, 1980.
- [61] I. Saka-Voivod, F. Sciortino, T. Grande, and P. H. Poole. Simulated silica. *Phil. Trans .R. Soc. A*, 363:525, 2004.
- [62] H. Kimizuka, H. Kaburaki, and Y. Kogure. Molecular dynamics study of the high-temperature elasticity of quartz above the alpha-beta phase transition. *Phys. Rev. B.*, 67(024105), 2003.
- [63] N. J. Henson, A. K. Cheetham, and J. D. Gale. Theoretical calculations on frameworks and their correlation with experiment. *Chem. Mater.*, 6:1647–1650, 1994.

- [64] P. Hohenberg and W. Kohn. Inhomogeneous electron gas. *Phys. Rev. B*, 136:864–871, 1964.
- [65] J. P. Perdew and Y. Wang. Accurate and simple analytic representation of the electron-gas correlation energy. *Phys. Rev. B.*, 45(23):13244–13249, 1992.
- [66] DMol3. DMol3 website. <http://accelrys.com/products/materials-studio/quantum-and-catalysis-software.html>.
- [67] J. M. Haile. *Molecular Dynamics Simulation*. Wiley Professional Paperback Series, 1997.
- [68] E. Rossler and A. P. Sokolov. The dynamics of strong and fragile glass formers. *Chemical geology*, 128:143–153, 1996.
- [69] P. W. Atkins. *Physical chemistry*. Oxford University Press, 4th edition, 1990.
- [70] J. Haines, C. Levelut, A. Isambert, P. Hebert, S. Kohara, D. A. Keen, T. Hammouda, and D. Andrault. Topologically ordered amorphous silica obtained from the collapsed siliceous zeolite, silicalite-1-F: a step toward “perfect” glasses. *J. Amer. Chem. Soc.*, 131:12333–12338, 2009.
- [71] A. A. Hassanali and S. J. Singer. Static and dynamic properties of the water/amorphous silica interface: a model for the

- undissociated surface. *J. Computer Aided Material Design*, 2007.
- [72] I. Saka-Voivod, F. Sciortino, and P. H. Poole. Free energy and configuration entropy of liquid silica: Fragile - to - strong crossover and polyamorphism. *Phys. Rev. E*, 69:041503, 2004.
- [73] M. S. Shell, P. G. Panagiotopoulos, and A. Z. Debenetti. Molecular structural order and anomalies in liquid silica. *Phys. Rev. E*, 66:011202, 2002.
- [74] Y. Zhang, G. Guo, K. Refson, and Y. Zhao. Finite size effect at both high and low temperatures in molecular dynamics calculations of the self diffusion coefficient and viscosity of silica. *J. Phys. Condens. Matter*, 16:9127–9135, 2004.
- [75] K. Vollmayr, W. Kob, and K. Binder. Cooling rate affects in amorphous silica: A computer simulation study. *Phys. Rev. B.*, 54(22):808, 1996.
- [76] F. Bejina and O. Jaoul. Silicon diffusion in silicate minerals. *Earth and Planetary Sci. Lett.*, 153:229, 1997.
- [77] O. Jaoul, F. Bejina, and F. Elie. Silicon self diffusion in quartz. *Phys. Rev. Lett.*, 74:2038, 1995.

- [78] E. L. Williams. Diffusion of oxygen in fused silica. *J. Amer. Cer. Soc.*, 48:190–194, 1965.
- [79] J. Daintith. *Oxford Dictionary of Chemistry*. Oxford University Press, 5th edition, 2004.
- [80] J. C. Mikkelsen Jr. Self-diffusivity of network oxygen in vitreous SiO₂. *Appl. Phys. Lett.*, 45:1187–1189, 1984.
- [81] E. W. Sucov. Diffusion of oxygen in vitreous silica. *J. Amer. Cer. Soc.*, 46(1):14, 1963.
- [82] K. Muehlenbachs and H. A. Schaeffer. Oxygen diffusion in vitreous silica - utilisation of natural isotopic abundances. *Canadian mineralogist*, 15:179–184, 1977.
- [83] H. A. Schaeffer. Oxygen and silicon diffusion - controlled processes in vitreous silica. *J. Non. Cryst. Sol.*, 38:545–550, 1980.
- [84] J. Horbach and W. Kob. Static and dynamic properties of a viscous silica melt. *Phys. Rev. B*, 60:3169, 1999.
- [85] P. K. Hung, N. V. Hong, and L. T. Vinh. Diffusion and structure in silica liquid: a molecular dynamics simulation. *J. Phys. Condens. Matter*, 19:466103, 2007.
- [86] M. Micoulaut. A comparative numerical analysis of liquid silica and germania. *Chemical geology*, 213:197–205, 2004.

- [87] R. L. Mozzi and B. E. Warren. The structure of vitreous silica. *J. Appl. Cryst.*, 2:164, 1969.
- [88] A. Carre, J. Horbach, S. Ispas, and W. Kob. New fitting scheme to obtain effective potential from Car-Parrinello molecular dynamics simulations: Application to silica. *EPL*, 82(17001), 2008.
- [89] G. H. Beall. Industrial applications of silica. In *Silica*, volume 29 of *Reviews in Mineralogy*, page 493. Mineralogical Society of America, 1994.
- [90] H. F. Poulsen, J. Neufeind, H.-B. Neuman, J. R. Schneider, and M. D. Zeidler. Amorphous silica studied by high-energy x-ray diffraction. *J. Non. Cryst. Sol.*, 188:63–74, 1995.
- [91] P. G. Coombs, J. F. De Natale, P. J. Hood, D. K. McElfresha, R. S. Wortman, and J. F. Shackelford. The nature of the Si-O-Si bond angle distribution in vitreous silica. *Philosophical Magazine B.*, 51(4):L39 –L42, 1985.
- [92] F. L. Galeener. A model for the distribution of bond angles in vitreous SiO₂. *Philosophical Magazine B.*, 51(1):L1–L6, 1985.
- [93] T. M. Clark, P. J. Grandinetti, P. Florian, and J. F. Stebbins. Correlated structural distributions in silica glass. *Phys. Rev.*

- B*, 70:64202, 2004.
- [94] S. N. Taraskin and S. R. Elliott. Nature of vibrational excitations in vitreous silica. *Phys. Rev. B*, 65:8605, 1997.
- [95] S. N. Taraskin and S. R. Elliott. How to calculate the true vibrational density of states from inelastic neutron scattering. *Physica B*, 234-236:452–454, 1997.
- [96] C. Oligschleger. Dynamics of silica glasses. *Phys. Rev. B*, 60(5):3182–3193, 1999.
- [97] S. Susman, K. J. Volin, D. L. Price, M. Grimsditch, J. P. Rino, R. K. Kalia, P. Vashishta, G. Gwanmesia, Y. Wang, and R. C. Lieberman. Intermediate range order in permanently densified vitreous silica: A neutron diffraction and molecular dynamics study. *Phys. Rev. B*, 43(1):1194–1197, 1991.
- [98] R. J. Hemley, H. K. Mao, P. M. Bell, and B. O. Mysen. Raman spectroscopy of SiO₂ glass at high-pressure. *Phys. Rev. Lett*, 57(6):747, 1986.
- [99] B. Champagnon, C. Martinet, M. Boudeulle, D. Vouagner, C. Coussa, T. Deschamps, and L. Grosvalet. High-pressure elastic and plastic deformations of silica: In situ diamond

- anvill cell raman experiments. *J. Non. Crys. Sol.*, 354:569–573, 2008.
- [100] M. Grimsditch. Polymorphism in amorphous silica. *Phys. Rev. Lett.*, 52(26):2379–2381, 1984.
- [101] H. Sugiura and T. Yamadaya. Raman scattering in silica glass in the permanent densification region. *J. Non. Crys. Sol.*, 144:151–158, 1992.
- [102] C. H. Polsky, K. H. Smith, and G. H. Wolf. Effect of pressure on the absolute raman scattering cross-section of silica and germania glasses. *J. Non. Crys. Sol.*, 248:159–168, 1999.
- [103] R. J. Hemley, C. T. Prewitt, and K. J. Kingma. High-pressure behaviour of silica. In *Silica*, volume 29 of *Reviews in mineralogy*. Mineralogical Society of America, 1994.
- [104] C. Meade, R. J. Hemley, and H. K. Mao. High-pressure x-ray diffraction of silica glass. *Phys. Rev. Lett.*, 69(9):1387–1391, 1992.
- [105] E. C. T. Chao, J. J. Fahey, and J. Littler. Stishovite, silica, a very high pressure new mineral from meteor crater, arizona. *J. Geophysical Research*, 67(1):419–421, 1962.

- [106] W. Sinclair and A. E. Ringwood. Single crystal analysis of the structure of stishovite. *Nature*, 272:714–715, 1978.
- [107] K. O. Trachenko and M. T. Dove. Intermediate state in pressurised silica glass: reversibility window analogue. *Phys. Rev. B*, 67(212203), 2003.
- [108] K. O. Trachenko and M. T. Dove. Floppy modes in silica glass under pressure. *J. Phys. Condens. Matter*, 14:1143–1152, 2002.
- [109] K. O. Trachenko and M. T. Dove. Compressibility, kinetics and phase transition in pressurised amorphous silica. *Phys. Rev. B*, 67(064107), 2003.
- [110] S. Tsuneyuki, M. Tsukada, and H. Matsui Y. Aoki. First principles interatomic potential of silica applied to molecular dynamics. *Phys. Rev. Lett*, 61:869, 1998.
- [111] J. S. Tse, D. D. Klug, and Y. le Page. High-pressure densification of amorphous silica. *Phys. Rev. B*, 46(10):5933–5938, 1992.
- [112] L. Huang and J. Kieffer. Amorphous-amorphous transitions in silica glass. I. reversible transitions and thermomechanical anomalies. *Phys. Rev. B*, 69(224203), 2004.

- [113] F. K. El'kin, V. V. Brazhkin, L. G. Khvostantsev, O. B. Tsiok, and A. G. Lyapin. In situ study of the mechanism of formation pressure densified silica glasses. *JETP letters*, 75(7):314–347, 2002.
- [114] G. D. Mukherjee, S. N. Vaidya, and V. Sugandhi. Direct observation of amorphous to amorphous apparently first-order phase transition in fused quartz. *Phys. Rev. Lett.*, 87(19):195501–1 – 195501–4, 2001.
- [115] P. McMillan, B. Piriou, and R. Couty. A raman study of pressure densified vitreous silica. *J. Chem. Phys.*, 81(10):4234–4236, 1984.
- [116] B. T. Poe, C. Romano, and G. Henderson. Raman and XANES spectroscopy of permanently densified vitreous silica. *J. Non. Cryst. Sol.*, 341(1-3):162–169, 2004.
- [117] G. E. Walrafen, Y. C. Chu, and M. S. Hokmabadi. Raman spectroscopic investigation of irreversibly compacted vitreous silica. *J. Chem. Phys.*, 92(12):6987–7002, 1990.
- [118] L. Huang and J. Kieffer. Amorphous-amorphous transitions in silica glass. II irreversible transitions and densification limit. *Phys. Rev. B*, 69(224204), 2004.